New type of photoelectric converter based on an *n*-CdO/*a*-C/*p*-Si heterostructure

A. M. Baranov, Yu. A. Malov, and S. A. Tereshin

S. A. Vekshinskiĭ State Scientific Research Institute of Vacuum Technology, Moscow
(Submitted April 17, 1997)
Pis'ma Zh. Tekh. Fiz. **23**, 1–6 (November 12, 1997)

A new system for a photoelectric converter is proposed, and its photoelectric properties are studied, using an *n*-CdO/*a*-C/*p*-Si heterostructure as an example. The distinguishing feature of the structure is that the broad-band insulating layer of SiO_2 on the surface of the silicon is replaced by a narrow-band layer of amorphous carbon, while a layer of CdO is used as the upper electrode. It is shown that an increase of the short-circuit current because of impact ionization can be expected in such a heterostructure. The results of the paper show that it is worthwhile to use CdO films in practice as transparent electrodes. © *1997 American Institute of Physics.* [S1063-7850(97)00111-0]

The problem of obtaining ecologically clean electrical energy by the conversion of solar radiation has recently become more and more important. The creation and study of new materials and methods for directly converting light into electrical energy is therefore extremely crucial, taking into account that the most widely used material in solar energy—silicon—has already almost reached its limiting efficiency.[1–3]

This paper proposes a new system for a photoelectric converter that makes it possible to increase the short-circuit current both by creating conditions for impact ionization and by increasing the internal quantum yield of the converter in the short-wavelength region.

The energy-band diagram of the converter is shown in Fig. 1. The essence of the proposed system for a photoelectric converter is as follows: When a cell is formed between a *p*-type layer (P1) and an *n*-type layer (P3) that have different band gaps, an intermediate semiconductor layer (P2) is produced in which there is a strong electric field. The purpose of the layer is to heat the charge carriers and to transport them between the *n* and *p* layers without scattering. When this occurs, the photogenerated carriers can acquire sufficient energy for impact ionization, and this generates additional charge carriers.

To make sure that these conditions are fulfilled, the parameters of the layers of the heterostructure must be chosen starting from the following considerations:

The band gap E_{g3} of layer P3, on which sunlight is incident, must be greater than E_{g1} in order to provide the ''window'' effect. Layer P3 in the converter is based on a semiconductor with $E_{g3} \approx 2.5$ eV. There are photons in the solar spectrum with energies $E > E_{g3}$, which will be absorbed in layer P3. Photons with $E < E_{g3}$ are transmitted through layer P3, and, if their energy is greater E_{g1}, they are absorbed in layer P1. The band gap E_{g3} is chosen so that minority carriers travelling from P3 to P1 acquire enough energy at the P3–P2 interface to produce impact ionization in layer P1.

The conditions for the appearance of impact ionization obtain when the relationship $(3/2)E_{g1} < E_{g3} - \eta_1 - U_1$ is sat-

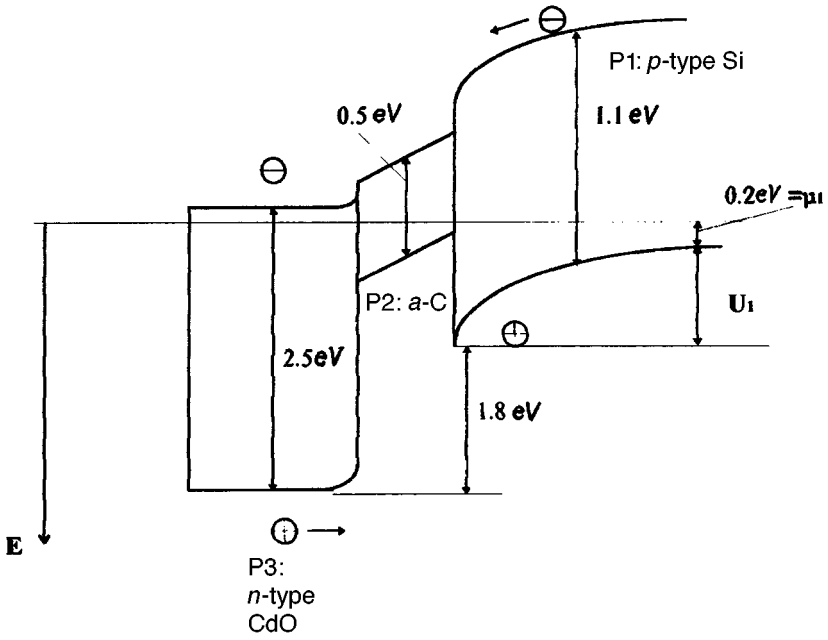

FIG. 1. Energy-band diagram.

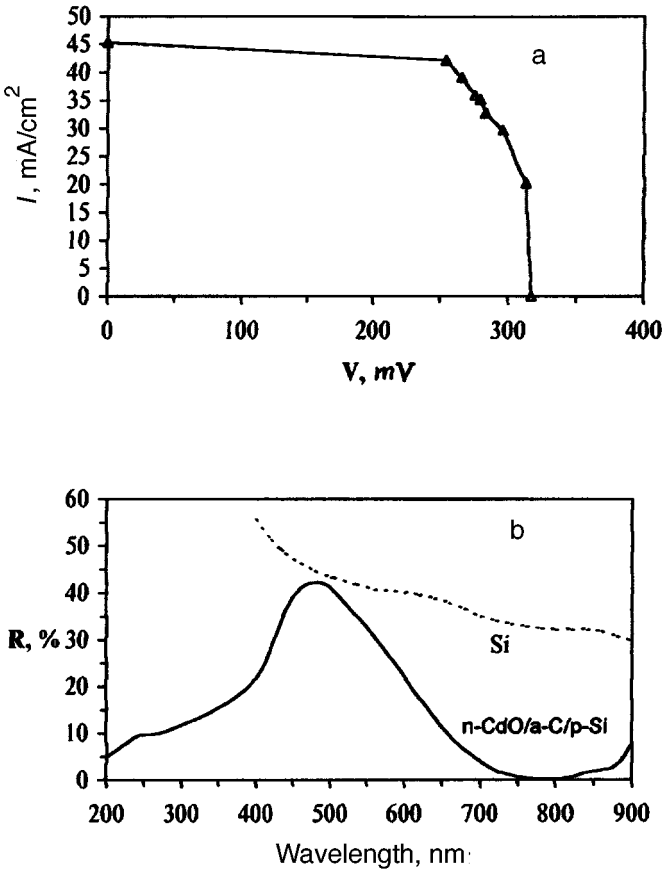

FIG. 2. Current–voltage characteristic of an n-CdO/a-C/p-Si structure illuminated by sunlight with an intensity of 0.1 W/cm^2 (a), and reflectance R vs wavelength for the photoelectric converter described here and for pure silicon (b).

isfied, in which U_1 is the voltage corresponding to the band bending in P1, and η_1 is the difference between the Fermi energy and the energy of the top of the valence band in P1.

In order to reduce the series resistance of the converter (and consequently to increase the fill factor) and to increase the carrier collection, layer P3 can be based on a strongly doped semiconductor. Moreover, the thickness of layer P3 is chosen so that it is an antireflection coating with respect to layer P1. Consequently, semiconductor layer P3

- is an antireflection coating with respect to layer P1,
- collects charge-carriers from the surface of the converter, and
- generates electron–hole pairs because of the absorption of light in the blue region of the visible solar spectrum.

This structure is similar to an MIS structure in that a thin intermediate layer P2 is present in it between layers P1 and P3. The presence of a thin insulating layer in a metal–insulator–semiconductor structure makes it possible to increase the open-circuit voltage V_{oc} in comparison with a Schottky barrier by means of a built-in positive charge.[4] At the same time, this layer (in any case) impedes the movement of the charge carriers because of the presence of a potential barrier at the layer boundary. Therefore, in the structure under consideration, a broad-band insulating layer is replaced with a narrow-band semiconductor layer. The parameters of layer P2 must be such that they ensure the transport of charge carriers through it in the ballistic regime (i.e., the mean free path of the carriers in layer P2 must be greater than the layer thickness, while $E_{g2}<E_{g1}$). Thus, the relationship between the band gaps of the layers is $E_{g3}>E_{g1}>E_{g2}$.

The physical processes underlying the functioning of the proposed converter have the following feature: Discontinuities of the potentials at the interfaces between P1 and P2 and between P2 and P3 produce heating of the electrons and holes. If, as they pass through layer P2, the hot ballistic electrons and holes experience no recombination or scattering, the holes entering layer P1 will have enough energy to generate electron–hole pairs. This causes an increase of the short-circuit current.

In creating a photoelectric converter, we started from the materials and technologies available to us. Therefore, silicon with p-type conductivity (KDB-10) was chosen as the material for layer P1. The plate had thickness 330 μm and $E_{g1}=1.1$ eV. The intermediate layer P2 is made from amorphous carbon (a-C) of thickness 30 Å, with $E_{g2}=0.5$ eV. The thickness of the a-C was monitored during deposition.[5,6] The broad-band semiconductor CdO, with a band gap of 2.5 eV (Refs. 7 and 8) and a thickness of about 800 Å, was used as the second, n-type, outer layer P1. Amorphous carbon layers were obtained by magnetron sputtering of graphite in argon, and the CdO was obtained in an atmosphere of nitrogen with oxygen. The active area of the photoelectric converter was $S=0.64$ cm^2. The CdO layer consisted of two regions with different resistivities. The first region (next to the P3–P2 interface) was 100 Å wide and had a resistivity of $\approx 1\ \Omega\cdot$cm, while the second had $\rho=5\times10^{-4}\Omega\cdot$cm. The change in resistivity was produced by varying the oxygen concentration in the CdO.[8] Two regions were created because it was necessary to introduce an electric field inside the CdO layer that aided the motion of the carriers generated in the CdO in order to increase their collection.

Figure 2a shows the current–voltage characteristic of the n-CdO/a-C/p-Si structure when it is illuminated by sunlight with an intensity of 0.1 W/cm^2. It can be seen that, despite the small value of $V_{oc}=0.32$ V, the short-circuit current reaches the values obtained in the best silicon-based solar cells.[1,2] The efficiency of the structure is about 11.5%. In the absence of the a-C layer, the short-circuit current was several times less, which was possibly associated with the high density of boundary states. Figure 2b shows how the reflectance R depends on wavelength for the given structure (curve *1*) and for pure silicon (curve *2*). It can be seen that R is virtually equal to zero at a wavelength of 800 nm.

Even though the conditions of the experimental heterostructure described here were not optimal, it follows from the above that the proposed photoelectric converter system is promising for further studies.

[1] M. Grauvogl, A.G. Aberle *et al.*, Appl. Phys. Lett. **69**, 1462 (1996).
[2] J. Zhao, A. Wang *et al.*, Appl. Phys. Lett. **66**, 3636 (1996).
[3] ''Solar cells and their industrial application. Advances in materials technology,'' Monitor, UNIDO No. 31, 2 (1993).
[4] S. M. Sze, *Physics of Semiconductor Devices* (Wiley, New York, 1969).

[5] A. Baranov, S. Tereshin, I. Mikhailov *et al.*, Proc. SPIE **2863**, 359 (1996).
[6] A. Baranov, S. Tereshin, I. Mikhailov, *et al.*, Proc. SPIE **2519**, 108 (1995).
[7] T.L. Chu and S. Shirley, J. Electr. Mater. **19**, No. 9 (1990).
[8] C. Scavani and K. T. R. Reddy, Semicond. Sci. Technol. No. 6, 1036 (1991).

Translated by W. J. Manthey
Edited by David L. Book

Nonradiative energy transfer from titanium (III) ions to erbium (III) ions in aluminosilicophosphate glass

I. M. Batyaev and E. B. Kleshchinov

A. I. Gertsen Russian State Pedagogical University, St. Petersburg
(Submitted March 17, 1997)
Pis'ma Zh. Tekh. Fiz. **23**, 7–11 (November 12, 1997)

A luminophor based on aluminosilicophosphate glass doped with erbium (III) and titanium (III) has been synthesized. It is shown that the erbium luminescence in this glass is efficiently sensitized by the titanium ions via the $^4I_{13/2}\rightarrow{}^4I_{15/2}$ channel ($\lambda=1.538$ μm). It is determined that the transport is by a dipole–dipole mechanism. The critical transport concentration is 0.032 M, and the critical transport distance is 1.95 nm. © *1997 American Institute of Physics.* [S1063-7850(97)00211-5]

One way to enhance the energy efficiency and economy of solid-state erbium lasers is to introduce impurity ions into the matrix that can absorb energy in the visible region and can then transfer it to the erbium ions. Despite the significant advances that have been achieved in this scientific direction,[1] the search for new sensitizers of the 1.5-μm luminescence of erbium remains pressing.[2]

In this paper we study of the possibility of nonradiative excitation-energy transport from titanium (III) ions to erbium in aluminosilicophosphate glass. The spectroluminescence properties of titanium (III) in various glassy matrices were studied in Refs. 3–6. We showed in Refs. 7–10 that titanium ions in phosphate glasses are efficient sensitizers of the luminescence of neodymium and ytterbium.

A glassy matrix was synthesized by the method of coprecipitation from the solutions, producing a high degree of homogeneity in the resulting glass. The concentration of activator ions was 0.5 wt% for erbium and 1 wt% for titanium.

We carried out a series of experiments that allowed us to conclude that erbium luminescence is efficiently sensitized by titanium.

Superposition of the absorption bands of titanium and erbium is observed in the electronic absorption spectrum of the resulting glass (Fig. 1, curve *A*). We detected no visible differences from the spectra of the corresponding noncodoped ions in the same matrix. The absorption maximum of titanium lies in the 560-nm region. The luminescence was recorded with an SDL-1 spectrometer, using an FEU-79 photomultiplier and an original photon counter with a digital-to-analog converter. An ISSh-100 pulse lamp with an MDR-2 monochromator and an LGN-222 He–Ne laser ($\lambda_B=630$ nm, $P=55$ mW) were used as excitation sources. Glasses doped only with titanium ions (with no codopant) exhibit intense luminescence in the 750–980-nm region (Fig. 1, curve *C*). The relative intensity of the luminescence band of titanium decreases by more than a factor of 10 in the luminescence spectrum of glass codoped with Er^{3+} and Ti^{3+} simultaneously. In this case, an increase is noted in the luminescence intensity of erbium at the $^4I_{13/2}\rightarrow{}^4I_{15/2}$ transition ($\lambda=1.538$ μm) after titanium ions are introduced into the matrix (Fig. 2).

A band is present in the 500–700-nm spectral region in the luminescence excitation spectrum of the Er^{3+} ion in Ti^{3+}–Er^{3+}-doped aluminosilicophosphate glass (Fig. 3) that

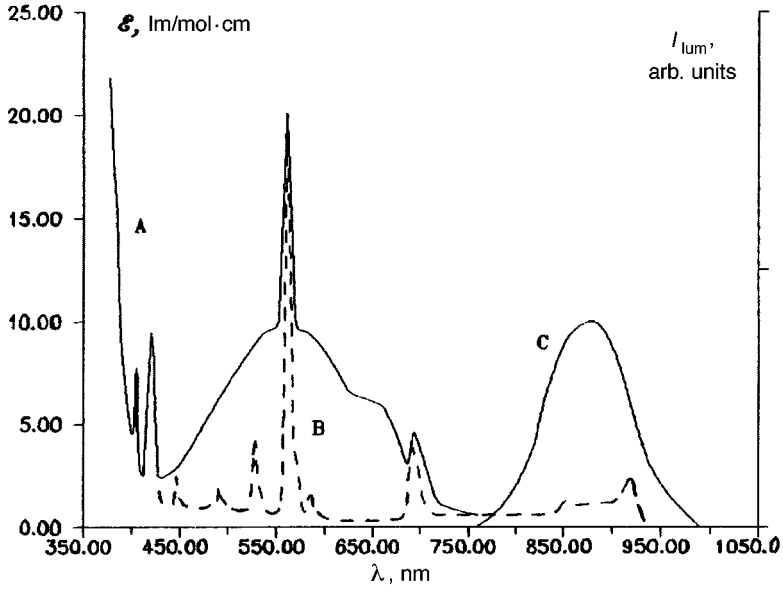

FIG. 1. Absorption (A, B) and luminescence (C) spectra of aluminosilicophosphate glass doped with Ti^{3+}–Er^{3+} (A), Er^{3+} (B) and Ti^{3+} (C).

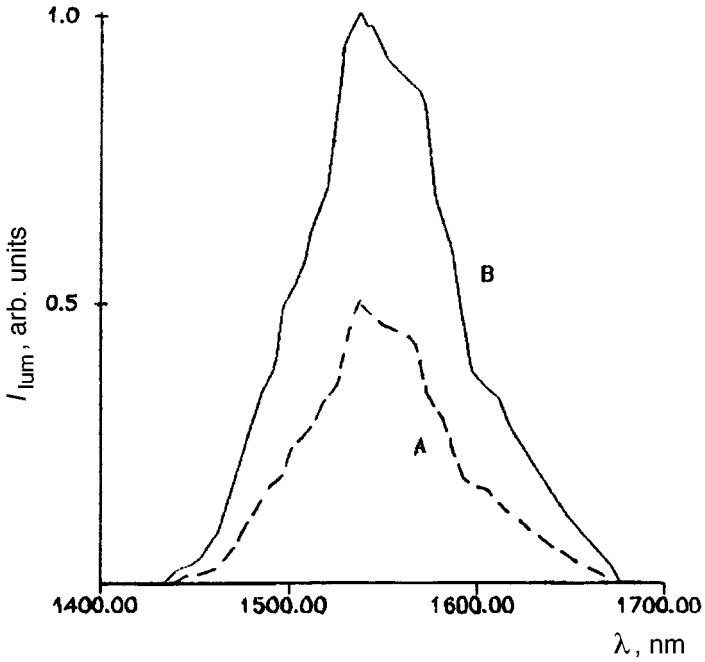

FIG. 2. Luminescence spectrum of erbium in aluminosilicophosphate glass doped with Er^{3+} (A) and Ti^{3+}–Er^{3+} (B).

corresponds to the absorption of the Ti^{3+} ion, and this is evidence of $Ti^{3+} \rightarrow Er^{3+}$ nonradiative energy transport. In studying the luminescence-damping kinetics, we found that the mean lifetime of the excited state of Ti^{3+} ions decreased from 6 to 2.5 μs in the presence of Er^{3+} ions. The kinetic curve in this case had a nonexponential character. The $Ti^{3+} \rightarrow Er^{3+}$ energy transport in all likelihood is by a dipole–dipole mechanism. Such an assertion allowed us to carry out the corresponding calculations from the equation

$$\rho(t) = \exp\left[-\frac{t}{\tau_{OD}} - \frac{C_A}{C_0}\Gamma\left(1-\frac{3}{S}\right)\left(\frac{t}{\tau_{OD}}\right)^{3/S}\right], \qquad (1)$$

where $\rho(t)$ is the luminescence-damping law of a donor; τ_{OD} is the mean luminescence-damping time of a donor in the absence of quenching; C_A is the concentration of energy-acceptor molecules; C_0 is the critical energy-transport concentration; t is the luminescence-damping time of a donor, normalized by intensity; $\Gamma(x)$ is the gamma function; and S is a constant determined by the nonradiative energy-transfer

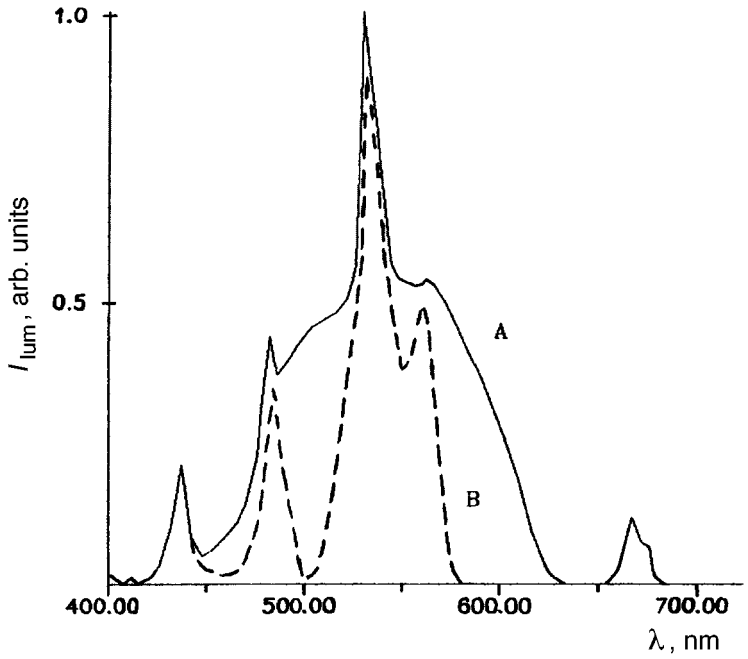

FIG. 3. Luminescence excitation spectrum of erbium in aluminosilicophosphate glass doped with Ti^{3+}–Er^{3+} (A) and Er^{3+} (B).

mechanism. Numerical calculations showed that Eq. (1) gives the most satisfactory description of the experimental curve of the titanium luminescence damping kinetics on the assumption of a dipole–dipole transport mechanism when $S=6$. From this, the critical energy-transport concentration is determined as $C_0=0.032$ M.

The equation

$$R=\left(\frac{3}{4\pi C_0}\right)^{1/3} \tag{2}$$

was used to determine the critical transport distance as $R=1.95$ nm.

It has thus been shown for the first time that the luminescence of erbium can be efficiently sensitized by titanium (III) ions in glasses.

[1] V. P. Gapontsev, A. K. Gromov, A. A. Izyneev, P. I. Sadovskiĭ, A. A. Stavrov, Yu. S. Tipenko, and A. P. Shkadarevich, Kvant. Elektron. (Moscow) **16**, No. 1 (1989) [Quantum Electron. **19**, 447 (1989)].

[2] D. Scrano, IEEE J. Quantum Electron. **32**, 628 (1996).

[3] I. M. Batyaev and S. B. Sukhanov, Opt. Spektrosk. **72**, 1367 (1992) [Opt. Spectrosc. (USSR) **72**, 765 (1992)].

[4] I. M. Batyaev and I. V. Golodova, Opt. Spektrosk. **77**, 54 (1994) [Opt. Spectrosc. **77**, 45 (1994)].

[5] S. B. Sukhanov, ''Spectroluminescent properties of phosphate glass doped with titanium (III) and neodymium (III),'' Author's abstract of dissertation for candidate degree, Russian State Pedagogical University, St. Petersburg, 1994.

[6] I. V. Golodova, ''Spectroluminescent and some physicochemical properties of gallium phosphate glasses doped with Ti^{3+} and Nd^{3+} ions,'' Author's abstract of dissertation for candidate degree, Russian State Pedagogical University, St. Petersburg, 1994.

[7] I. M. Batyaev and E. B. Kleshchinov, Pis'ma Zh. Tekh. Fiz. **22**, No. 12 (1996) [Tech. Phys. Lett. **22**, 494 (1996)].

[8] I. M. Batyaev, S. B. Sukhanov, O. A. Lasor, and E. B. Kletchinov, in Abstracts of the Eleventh Conference on Physical Methods in Coordination Chemistry, Kishinev, 1993, p. 85.

[9] I. M. Batyaev and S. B. Sukhanov, Pis'ma Zh. Tekh. Fiz. **20**, No. 10, 38 (1994) [Tech. Phys. Lett. **20**, 403 (1994)].

[10] I. M. Batyaev and I. V. Golodova, Opt. Spektrosk. **78**, 468 (1995) [Opt. Spectrosc. (USSR) **78**, 421 (1995)].

Translated by W. J. Manthey
Edited by David L. Book

Effect of the width of the spacer layers on the size of the bistability region in the current–voltage characteristics of two-barrier tunnel resonance diodes

M. M. Vrubel', V. M. Borzdov, and F. F. Komarov

Belarus State University, Minsk
(Submitted April 3, 1997)
Pis'ma Zh. Tekh. Fiz. **23**, 12–16 (November 12, 1997)

This paper discusses the question of how the size of the spacer layers affects the position and width of the bistability region in the current–voltage characteristics of tunnel resonance diodes. The current–voltage characteristics were calculated in terms of the self-consistent effective-mass approximation. Increasing the size of the spacer layers shifts the lower boundary of the bistability region upwards so that this region becomes narrower and then completely disappears. [S1063-7850(97)00311-X]

As is well known, under certain conditions the current–voltage characteristics of two-barrier tunnel resonance structures display the bistability effect in regions with negative differential resistance.[1–4] This paper discusses the question of how the size of the spacer layers affects the position of the boundaries of the hysteresis loops in the current–voltage characteristics of two-barrier tunnel resonance structures. Current–voltage characteristics with sections of bistability in regions with negative differential resistance were calculated using the system proposed in Ref. 6, which includes self-consistent solution of the Poisson and Schrödinger equations. Two-barrier AlAs/AlGaAs diodes with parameters similar to those in Ref. 6 were considered: the width of the barriers and of the quantum well was 50 Å, the donor impurity concentration in the contacts was 10^{18} cm^{-3}, the effective mass of the electron was $m=0.067m_0$, the quantum barrier was $V_0=370$ meV, and the relative permittivity was $\varepsilon_R=11.9$. All the current–voltage characteristics are calculated for a temperature of $T=5$ K.

The mechanism by which two stable current states arise in the region of negative differential resistance can be explained as follows:[5–8] As the external voltage is increased (moving from peak currents to valley currents), the resonance level approaches the bottom of the conduction band of the emitter from above. The resonance level, which lies in the energy region $U(0)<E<U(0)+E_F$, accumulates electrons that tunnel from the emitter. The charge of the electrons accumulated on the resonance level of the quantum well alters the potential profile of the structure, in particular by raising the bottom of the well. Because of this, the position of the resonance level is raised, and the voltage at which the resonance level crosses the bottom of the conduction band of the emitter consequently increases. Qualitatively, it is this voltage that forms the boundary between the regions of peak and valley currents. As the voltage falls (moving from a valley to a peak), the resonance level approaches the bottom of the conduction band of the emitter from below. In this case, there are no electrons at all on the resonance level [at low temperatures we neglect scattering and consequently the possibility of accumulating scattered electrons on the resonance level E_R, which is located at the bottom of the conduction band in the energy region $U(L)+E_F<E_R<U(0)$]. The examples considered below make it possible to refine the scheme given here.

As is well known, the presence of spacer layers between the strongly degenerate electrode regions and the quantum barriers introduces significant changes in the potential profile of the structure (Fig. 1). A potential barrier V^* arises that impedes the penetration of charge from the electrodes into the spacer layers. The bottom of the quantum well and consequently the position of the resonance level of the quantum well are raised by comparison with the bottom of the conduction band in the electrodes. The narrower the spacer layer, the smaller the value of V^*.

Figure 2a shows the current–voltage characteristics of two-barrier tunnel resonance diodes that differ only in the size of the spacer layers. It is easy to see that the size of the spacer layers has a strong effect on the position of the lower boundary of the bistability region. The lower boundary of the hysteresis loop (the region with two stable current states) corresponds to the intersection by the resonance level of the bottom of the conduction band of the emitter, provided that there is no accumulated charge in the quantum well. The position of the boundary can be estimated by the quantity $V_L=2(E_R+V^*)/e$. Thus, the narrower the spacer layers, the lower the potential V^* and consequently the smaller the value of V_L.

It should be pointed out that the position V_H of the upper boundary of the hysteresis loop is identical for all the structures that we considered for which the width of the spacer layers was between 35 and 50 Å (Fig. 2a). Figure 2b makes it possible to compare the charge Q accumulated by the quantum well for structures with spacers of different sizes. The quantity Q_m, the maximum charge held by a quantum well, corresponds to the maxima in the dependences of Fig. 2b. It is obvious that the relationship between Q_m and the width $\Delta V=V_H-V_L$ of the bistability region in the structures under consideration cannot be considered linear, unlike tunnel resonance diodes with no spacer layers.[5]

Note that if the spacer layers are so wide that the value of $V_L\approx 2(E_R+V^*)$ exceeds V_H, the region with two stable current states is absent, although charge is accumulated in the quantum well (Fig. 2, $w=60$ Å). The same effect has been detected experimentally.[2]

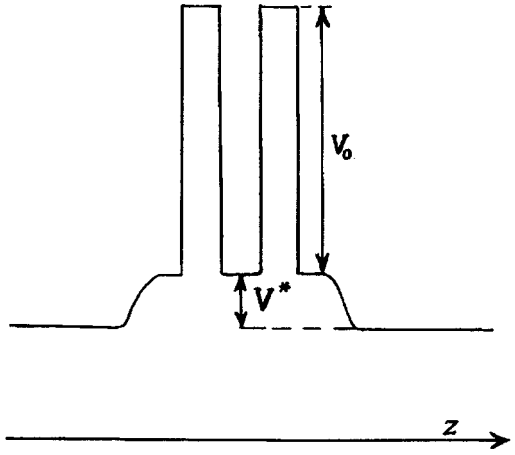

FIG. 1. Schematic representation of the potential profile of a two-barrier tunnel resonance diode with spacer layers.

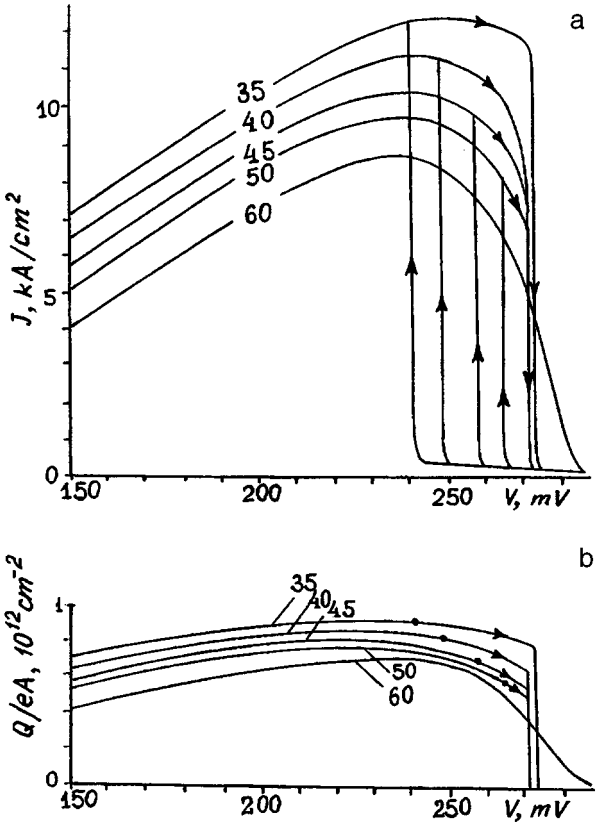

FIG. 2. Current density J (a) and the two-dimensional charge density Q/eA accumulated by the quantum well (b) vs applied external voltage V for two-barrier tunnel resonance diodes that differ in the size of the spacer layers. The numbers on the curves correspond to the width w of the spacer layers, the arrows show the direction in which the voltage varies, and the points show the lower boundary V_L of the bistability regions.

The situation in which the spacer layers are very narrow or absent altogether requires further study. Note that the position of the upper boundary of the hysteresis loop shifts upwards only slightly (Fig. 2, $w=35$ Å). In structures with thin spacer layers, when voltage V_H is reached, a significant falloff is observed in the potential in the emitter and collector regions adjacent to the structure. An enriched layer (at the collector) and a depleted layer (at the emitter) are formed. It becomes necessary to include wide electrode layers in the spatial region for self-consistency, which creates additional difficulties in achieving convergence in the self-consistent solution of the Schrödinger and Poisson equations. Moreover, the solution becomes very sensitive to the choice of initial conditions.

The main results of our work thus reduce to the following: The presence of spacer layers in two-barrier tunnel resonance structures causes the region with two stable current states (the hysteresis loops) to become narrower, because the lower boundary of the loop moves upwards as the width of the spacer layers increases. The position of the upper boundary of the hysteresis loop is identical for structures with spacer layers of different width until the spacer layers are sufficiently wide to impede the formation of depleted or enriched layers in the electrodes. If the spacer layers are so wide that the potential V^* exceeds the size of the bistability region of the analogous structure without spacer layers, the region with two stable current states does not appear.

[1] V. J. Goldman, D. C. Tsui, and J. E. Cunningham, Phys. Rev. Lett. **58**, 1256 (1987).
[2] T. Wei, S. Stapleton, and O. Berolo, J. Appl. Phys. **77**, 4071 (1995).
[3] A. Zaslavsky, V. J. Goldman, D. S. Tsui *et al.*, Appl. Phys. Lett. **53**, 1408 (1988).
[4] A. S. Ignat'ev, V. É. Kaminskiĭ, V. B. Kopylov *et al.*, Fiz. Tekh. Poluprovodn. **26**, 1795 (1992) [Sov. Phys. Semicond. **26**, 1005 (1992)].
[5] F. W. Shead and G. A. Toombs, Appl. Phys. Lett. **52**, 1228 (1988).
[6] J. O. Sofo and C. A. Balseiro, Phys. Rev. B. **42**, 7292 (1990).
[7] K. L. Jensen and F. A. Buot, Phys. Rev. Lett. **66**, 1078 (1991).
[8] R. J. Salvino and F. A. Buot, J. Appl. Phys. **72**, 5975 (1992).

Translated by W. J. Manthey
Edited by David L. Book

Efficiency and reliability of metal–insulator–semiconductor radiative structures based on broad-band semiconductors with unipolar conductivity

V. G. Sidorov, A. G. Drizhuk, and D. V. Sidorov

Vologda Polytechnical Institute
(Submitted June 27, 1997)
Pis'ma Zh. Tekh. Fiz. **23**, 17–23 (November 12, 1997)

This paper discusses the possibility of increasing the efficiency and reliability of radiation sources made from semiconductors with unipolar conductivity and operating in strong electric fields. To this end, the active region of the structure is fabricated in the form of alternating layers of different resistance, so that strong-field regions are spatially separated from luminescence-generation regions. The proposed idea is put into practice on M–*i*–*n* structures made from gallium nitride. The properties of fabricated LED structures are presented. © *1997 American Institute of Physics.* [S1063-7850(97)00411-4]

The problem of creating solid-state radiation sources for the short-wavelength parts of the visible spectrum remains crucial. The difficulties of solving it are associated with the phenomenon of self-compensation of the dopants by intrinsic defects of the crystal in broad-band semiconductors. This phenomenon makes it impossible to freely control the conductivity type of the semiconductor and to create *p*–*n* structures that emit efficiently. The semiconductor remains unipolar, and therefore the search for and the synthesis of new, easily doped broad-band semiconductors continues, along with the improvement of the technology for growing and doping those already known. It is also possible to follow the approach of creating new types of radiative structures based on unipolar semiconductors in which electroluminescence can be efficiently excited. This paper is devoted to the implementation of one such possibility.

Metal–insulator–semiconductor structures are most often used to excite electroluminescence in unipolar semiconductors. In the most efficient metal–insulator–semiconductor structures, the insulator region is made in the form of a semi-insulating layer from the same semiconductor as in the semiconductor layer, but strongly compensated. Moreover, one strives to choose the compensating impurity so that it simultaneously is an efficient radiative center. In this case, luminescence is excited in the *i* layer of the structure. Such structures are called M–*i*–*n* structures. The electroluminescence-excitation mechanism in them is associated with accelerating the majority carriers and also the nonequilibrium charge carriers in the strong electric field of the *i* layer to energies sufficient for the ionization or impact excitation of the luminescence centers. Nonequilibrium charge carriers appear in the *i* layer because of tunnel or impact ionization of impurities or atoms of the crystal. The probability of the given mechanisms is small in principle. The simplest method of increasing the concentration of hot charge carriers is to increase the electric field in the *i* layer. However, this rapidly degrades the structure and eventually causes breakdown. Moreover, the electroluminescence efficiency is reduced for all luminescence mechanisms in which nonequilibrium charge carriers participate, because the electrons and holes generated in the field are separated by the field in opposite directions and can leave the active region before they recombine.[1]

To increase the electroluminescence efficiency, it is necessary to localize the excitation and luminescence at the same centers, i.e., to use defects with an intracenter luminescence mechanism in the active region. Moreover, the given mechanism usually has a higher internal quantum yield than does a recombination mechanism. The reliability of the M–*i*–*n* structures must also increase in this case, since such centers, remaining neutral during excitation and radiation, are less subject to degradation in a strong electric field. An even larger increase of the lifetime of the M–*i*–*n* structures can be expected if the centers in general are not subjected to the action of a strong field. For this it is sufficient to spatially separate the strong-field region from the active region that contains the defects with intracenter luminescence, so that charge carriers are accelerated in the former and luminescence centers are excited in the latter by these accelerated carriers.

To put this proposal into practice, we chose GaN, now no longer unipolar, as the semiconductor with unipolar conductivity. When this experiment was planned, GaN with *p*-type conductivity had not yet been obtained. Neutral isoelectronic defects with intracenter luminescence were to be created by simultaneously isovalently doping GaN with acceptor and donor impurities—specifically, with zinc and oxygen.

Layers of GaN(Zn) and GaN(Zn, O) were grown on (1012) sapphire by vapor-phase epitaxy in a chloride–hydride system in a horizontal flow-through quartz reactor. Zn vapor was supplied to the growth zone by a flow of helium, while oxygen was transported in the form of H_2O vapor by a flow of ammonia. The temperature regimes of the process ensured that Zn and H_2O would interact in the substrate zone in order that Zn and O could be incorporated into the GaN lattice in the form of Zn–O coupled pairs. The resulting layers were oriented in the (1120) plane.

In the presence of O, the solubility of Zn in GaN increases to 8–10%. The Zn and O distributions reproduce one other well across a cleavage face of the layer. The Zn and O concentrations in the layers vary from 5×10^{19} to 2×10^{21} cm^{-3}. The resistivity of GaN(Zn, O) was always about two

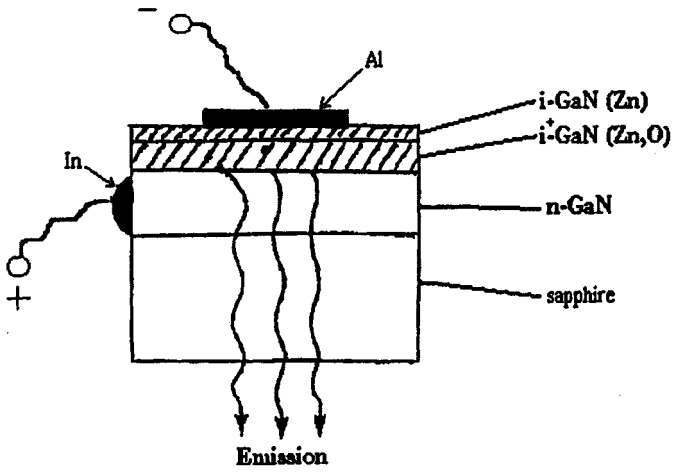

FIG. 1. A radiative M–i–n structure.

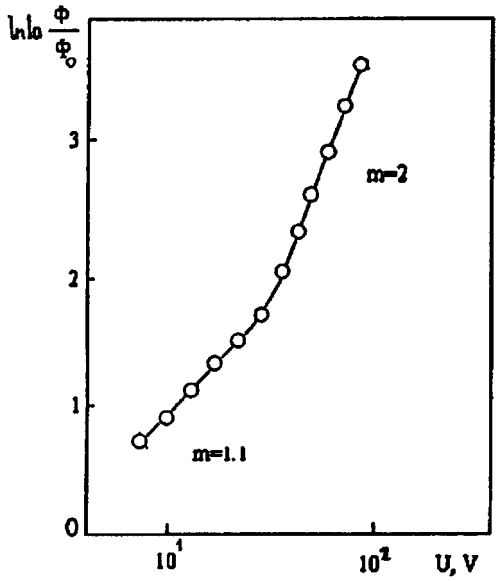

FIG. 2. Electroluminescence intensity vs voltage for an M–i–n structure with an active layer made from GaN(Zn, O).

orders of magnitude less than that of GaN(Zn) for identical concentrations of Zn in these layers. The formation of Zn–O coupled pairs in GaN(Zn, O) is indicated by a band of vestigial rays in the IR reflection spectra,[2] characteristic of ZnO crystals. In the photoluminescence spectra of GaN(Zn, O), along with bands characteristic of GaN(Zn), a new band having plane polarization is detected, with a maximum at 2.55 eV and a half-width of 0.3 eV. We associate the appearance of this band with the presence in the GaN(Zn, O) of defects that include Zn–O pairs. The given band was not observed in the photoluminescence spectra of GaN(O). An intracenter luminescence mechanism in the band detected here is indicated by (a) the character of the polarization patterns of the photoluminescence when it is excited by intrinsic and impurity light, (b) the form of the photoluminescence excitation spectra, and (c) the absence of additional photoconductivity in GaN(Zn, O) for any polarization of the exciting characteristic impurity light.

i-GaN(Zn)–i^+-GaN(Zn,O)–n-GaN/sapphire radiative structures (Fig. 1) were grown in a single process. A layer of undoped low-resistance n-GaN served as a buffer between the substrate and the i layer and simultaneously as an electrical contact to the latter. This layer was grown at 1050 °C at average growth rates of 20 μm/h, which ensured that it and the active i layer had high crystalline perfection. The n layer was 10–20 μm thick. The electron concentration and mobility had values of $(5\times10^{19}$–$10^{20})$ cm^{-3} and about 100 cm^2/V·sec. The active i region was grown as two layers at a temperature of about 950 °C and a growth rate of (6–10) μm/h. The characteristics of this region varied within the following limits: The i–GaN(Zn) layer was (0.05–0.5) μm thick, and its resistivity was $(10^5$–$10^7)\Omega\cdot$cm; the i^+–GaN(Zn,O) layer was (0.3–3) μm thick, and its resistivity was $(10^3$–$10^5)\Omega\cdot$cm. When the layer parameters are related in this way, virtually all the voltage applied to the structure falls across the i– GaN(Zn) layer; when the total voltage on the structure is 4–50 V, the electric field in this layer exceeds 10^5 V/cm, whereas the mean field in the i region does not exceed $(1$–$5)\times10^4$ V/cm. These fields are sufficient to produce impact generation of nonequilibrium charge carriers in the i–GaN(Zn) layer and to accelerate them to the energies necessary to excite the Zn–O centers in the i^+–GaN(Zn, O) layer. Because the structure is asymmetric, this can occur only for one polarity of the voltage on the structure—the minus contact must be to the i–GaN(Zn) layer. Actually, efficient polarized electroluminescence with characteristics corresponding to polarized photoluminescence in GaN(Zn, O) was observed in the structures only for this polarity of the voltage. When the i–GaN(Zn) layer was gradually ground away, polarized photoluminescence excited from the side of the surface of the structure by intrinsic light appeared and gradually increased in intensity. The gradual disappearance of the photoluminescence bands characteristic of GaN(Zn) was simultaneously observed. The total resistance of the i layer and the intensity of the polarized electroluminescence decreased at the same time, and more abruptly than the thickness.

When voltage was applied to the structure in the opposite polarity [plus on the i–GaN(Zn) layer], weak unpolarized electroluminescence of a spectrum close to the photoluminescence spectra of GaN(Zn) was excited. It follows from this that the strong-field condition is not achieved in the i^+-GaN(Zn,O) layer all the way to electric breakdown because of the low resistance of this layer. This is confirmed by such an experiment. After the i–GaN(Zn) layer is removed, polarized electroluminescence cannot be excited at all in the structure for either polarity of the voltage. However, after a new i-GaN(Zn) layer with a thickness of 0.1–0.2 μm was grown on the surface of the i^+-GaN(Zn, O), polarized electroluminescence was again observed in the same structures, but only for a minus voltage on this layer. Moreover, if a second i^+-GaN(Zn, O) layer was grown on the surface of the i-GaN(Zn), polarized electroluminescence could be excited with either polarity of the voltage on the structure.

All the experimental facts enumerated here prove that i–n structures with the planned arrangement and properties of the layers, in which the strong electric-field region is spa-

tially separated from the electroluminescence-excitation region, have been grown, and that the electroluminescence is excited by an impact mechanism, while the luminescence has an intracenter nature. An impact mechanism of the excitation of the luminescence centers is indicated by the fact that ignition of the electroluminescence is always observed on the linear section of the current–voltage characteristic, while the dependence of the electroluminescence intensity on the voltage (Fig. 2) obeys the equation $\Phi = \Phi_0 \exp(-b/U^m)$, where parameter m takes values of 1 and 2 in small and large fields, respectively.[1]

Various types of LEDs were fabricated on the basis of the $i-n$ structures that were grown: with blue polarized radiation,[2] with radiation controllable by light from the blue to the red,[3] with white radiation,[4] and also LEDs with enhanced luminous efficiency.[5] The efficiency of the LEDs was 0.1–0.3%, which is an order of magnitude better than the highest known values for radiative metal–oxide–semiconductor structures created on unipolar semiconductors. The LEDs showed high stability and reliability in operation. Their characteristics varied reversibly by more than 30% in the temperature interval 100–450 K, and they continued to function over the range 4–900 K. Irreversible changes of the parameters of unpackaged LEDs were less than 10% during more than 10 000 h of tests in working regimes. When they were irradiated with electrons and protons having an energy of (1–5) MeV at doses of up to 10^{16} cm^{-2}, the efficiency of the LEDs increased by about 30%.

Thus, the experiment carried out here not only confirmed the idea expressed above but also revealed a new material, GaN(Zn, O), possessing unique properties and polarized luminescence. Now that it is possible to grow p-type GaN stably, GaN(Zn, O) can be successfully used to create injection LEDs with blue polarized radiation, based, for example, on $p-i-n$ structures.

This work was carried out with the partial support of the University of Arizona.

[1] I. K.Vereshchagin, *Electroluminescence of Crystals* (Nauka, Moscow, 1974)
[2] A. G. Drizhuk, M. V. Zaĭtsev, V. G. Sidorov, and D. V. Sidorov, Pis'ma Zh. Tekh. Fiz. **22**, No. 6, 67 (1996) [Tech. Phys. Lett. **22**, 260 (1996)].
[3] A. G. Drizhuk, M. V. Zaĭtsev, V. G. Sidorov, and D. V. Sidorov, Pis'ma Zh. Tekh. Fiz. **22**, No. 7, 50 (1996) [Tech. Phys. Lett. **22**, 289 (1996)].
[4] A. G. Drizhuk, M. V. Zaĭtsev, V. G. Sidorov, and D. V. Sidorov, Pis'ma Zh. Tekh. Fiz. **22**, No. 12, 23 (1996) [Tech. Phys. Lett. **22**, (1996)].
[5] A. G. Drizhuk, M. V. Zaĭtsev, V. G. Sidorov, and D. V. Sidorov, Pis'ma Zh. Tekh. Fiz. **22**, No. 13, 33 (1996) [Tech. Phys. Lett. **22**, 613 (1996)].

Translated by W. J. Manthey
Edited by David L. Book

3.3-μm LEDs for measuring methane

A. A. Popov, M. V. Stepanov, V. V. Sherstnev, and Yu. P. Yakovlev

A. F. Ioffe Physicotechnical Institute, Russian Academy of Sciences, St. Petersburg
(Submitted May 15, 1997)
Pis'ma Zh. Tekh. Fiz. **23**, 24–31 (November 12, 1997)

LEDs have been created that emit in the region of the fundamental absorption band of methane at a wavelength of 3.3 μm for fast-response gas analyzers. A continuous optical power of 0.13 mW (cw) is achieved, and the peak optical power is 2.2 mW (the pulsewidth is 50 μs, and the inverse duty cycle is 1.6×10^2). The current dependence of the optical power on the pump-pulse parameters is studied, and the conditions are found under which the peak power of the radiation of the LEDs in the mid-IR region is maximized. [S1063-7850(97)00511-9]

The 3.3-μm spectral range is extremely attractive for purposes of detecting hydrocarbons in various media, since it contains the fundamental C–H absorption line of hydrocarbons.[1] Devices based on absorption spectral detection methods with radiators in this wavelength region are therefore promising for portable gas analyzers and warning devices for the maximum permissible concentration of methane, ethane, propane, and other gases both under production conditions (shops, gas lines) and in the household.[2] The radiation sources in them can be semiconductor LEDs, whose spectral power density, efficiency, and response rate substantially exceed the analogous ratings of thermal radiation sources. For the 3-μm spectral region, such diodes can be created from heterostructures based on CdHgTe semiconductors,[3] stressed layers of the compounds InGaAs/InP,[4] or solid solutions of InAsSb/InAs.[5–9] The last are the most attractive material, since they are based on III–V semiconductor heterostructures, which are distinguished by their stability against degradation and superior conductivity.

The purpose of this paper is to discuss the creation of LEDs based on the InAs/InAsSbP double heterostructures with the maximum spontaneous radiation at 3.3 μm at room temperature and to present the results of studies of the characteristics that are most essential to put them into practice. It will be shown that optimizing the parameters of the supply pulse of LEDs based on narrow-band semiconductors makes it possible to increase their maximum optical power by more than an order of magnitude.

The LEDs were double symmetrical InAs/InAsSbP heterostructures grown by liquid-phase epitaxy on InAs (100) substrates by the technology discussed earlier.[10] The structure consisted of three epitaxial layers: the active InAs layer (thickness 1.0 μm) was enclosed between two broad-band emitters of n-type and p-type InAsSbP. The active InAs layer was not specially doped. The broad-band InAsSbP bounding layers were grown with a phosphorous ($E_g=550$ μeV) content of 0.35 and were doped with Sn and Zn to a concentration of $(5–7)\times10^{18}$ and $(1–2)\times10^{18}$ cm^{-3} for the n-type and p-type layers, respectively.

The objects of the study were circular mesa diodes obtained by means of photolithography and deep chemical etching into the substrate. The area of the emitting surface ($S=7\times10^{-4}$ cm^2) was determined by the diameter of the mesa (300 μm). The size of the crystal of a single LED was 500×500 μm. The semiconductor crystal was soldered with indium onto a standard TO-18 housing. A parabolic reflector mounted on the housing served to narrow the spatial directionality pattern of the emission of the LED to 10°–12°. The LED with the parabolic reflector was 9 mm in diameter and 5.5 mm in length.

The electrical and spectral characteristics of the diodes were measured by means of a system based on a standard synchronous detector circuit, an MDR-12 monochromator, and a cooled InSb-based photodiode with a passband to 10 MHz. The optical power was recorded by an IMO-2M device. The measurements were made at room temperature ($T=296$ K).

The diodes were supplied in the continuous regime with current up to 150 mA dc and in the pulsed regime with an inverse duty factor of up to 10^3—no greater than 2 A. The current–voltage characteristics of the LEDs had a diode character with a cutoff voltage of about 0.12 V at room temperature (about 0.36 V at liquid-nitrogen temperature). If the current–voltage characteristic is described by the dependence $I=I_0\exp(qU/kT)$, where q is the charge of the electron, U is the voltage, k is Boltzmann's constant, and T is the temperature, the saturation current I_0 was about 4.6 mA. The series resistance with forward bias was about 0.6 Ω.

The emission spectrum of the LED in the continuous supply regime ($I=120$ mA) at room temperature is shown in Fig. 1. The spectrum contains one emission band with a maximum at a wavelength of $\lambda=3.3$ μm. The width of the emission spectrum of the LED at half-maximum (FWHM) was about 0.5 μm. We should point out that the given value is about 2.5–3 times as great as kT and is typical of the electroluminescence of InAs compounds. This probably can be associated not only with the presence of tails on the density of states in the conduction band but also with the possibility of radiative recombination in the region of the heteroboundaries. However, for practical applications, such a width of the spectrum makes it possible to raise the detection sensitivity by collecting the total absorption signal of a number of close-lying absorption lines of hydrocarbons. For comparison, the fundamental absorption bands of methane, based on the HITRAN92 database,[1] are shown in the upper part

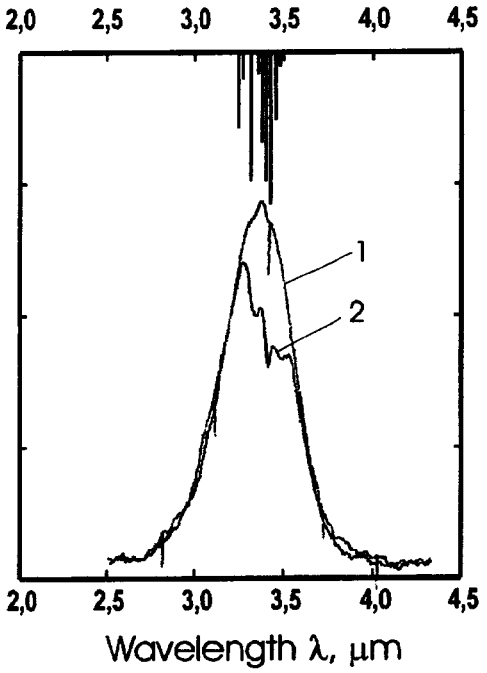

FIG. 1. Emission spectrum of an LED (curve *1*) recorded in the continuous supply regime at room temperature. The FWHM of the emission spectrum is 0.5 μm. The injection current is 120 mA dc. The absorption spectrum of the LED emission by methane at atmospheric pressure, recorded under the same conditions, is represented by curve *2*. The length of the sample cell was 2.5 cm. The position and relative intensity of the absorption lines of methane, based on the HITRAN92 database,[1] are shown for comparison in the upper part of the figure.

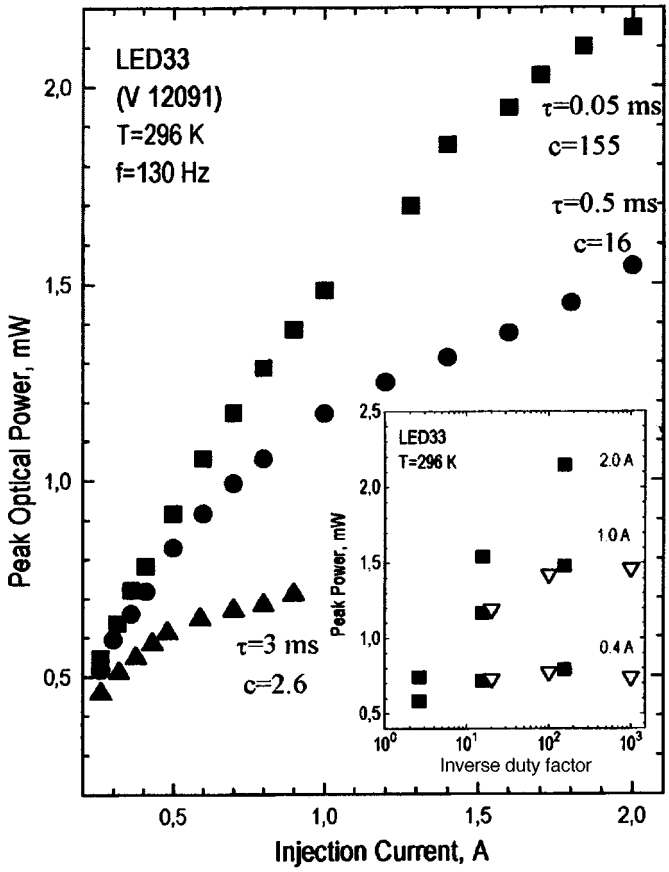

FIG. 2. Peak power of an LED at room temperature vs pulsewidth at a fixed pulse-repetition rate ($f=130$ Hz). The inset shows the effect of the duty factor of the current pulse on the maximum peak power of the LED and plots the dependences for injection currents of 0.4, 1, and 2 A. The highest peak power is reached when the inverse duty factor is about 1.6×10^2. The squares in the inset correspond to a supply regime in which the inverse duty factor was varied by varying the current pulsewidth while the pulse-repetition rate was fixed at 130 Hz. The triangles correspond to a variable repetition rate and a constant pulsewidth of about 1 μs.

of the figure. Figure 1 also shows the emission spectrum of the test LED transmitted through an absorbing cell 2.5 cm long filled with methane at atmospheric pressure. The shape of the spectrum corresponds to the absorption of radiation by hydrocarbons. The position of the maximum of the emission spectrum with the observed width of the LED spectrum is independent of the value of the injected current. When it was cooled to liquid-nitrogen temperature, the maximum shifted by 0.26 μm toward shorter wavelengths with a mean rate of about 1.1 nm/K, which was less than the temperature dependence of the band gap of InAs. As a whole, the spectral and electrical characteristics can be explained by quasi-interband recombination in the volume of the active region, which agrees with the conclusions of previous papers.[4,5]

In the continuous regime, the output optical power of the LED increased essentially linearly in the region of pumping currents up to 120 mA. The maximum continuous power was 130 μW. When the working current was increased further, the output power saturated, and the power decreased sharply (the power characteristic had a cutoff). This was most likely determined by Joule heating of the active region, since nonradiative processes predominate over radiative processes in narrow-band semiconductors as temperature increases[11] and, as the temperature decreased, the output power increased in accordance with the dependence $P\sim\exp(T/T_0)$, with a characteristic temperature T_0 of 56 K. At currents exceeding 150 mA (about 200 A/cm^2), the studies were carried out in the pulsed pump regime. We estimated the maximum modulation frequency from the total rise and fall times of the radiation when the pump current was switched, which was about 50–100 ns at room temperature. Therefore, the modulation frequency in our measurements was limited to the frequency range below 10 MHz. This is sufficient for most applications, since it allows modulation at frequencies exceeding thermal noise.

To study the current regimes at which the maximum pulsed radiation power is attained, measurements were made as a function of inverse duty factor ($c=2-10^3$) and current pulsewidth ($\tau=3$ ms–5 μs). Figure 2 shows the dependence of the peak optical power on the current pulsewidth at a fixed repetition rate. These power characteristics showed that the pump-pulse parameters had a strong influence on the radiative recombination efficiency and the output optical power of LEDs based on narrow-band compounds InAs/InAsSbP. The dependence for a pulsewidth of 3 μs (an inverse duty factor of 2.6) in the region of small currents was close to the dependence obtained for the continuous supply regime, whereas the slope of the current–voltage characteristic varied as a function of the current amplitude for the current region above 100–150 mA. With a pulsed supply, a difference in the efficiency was observed for the region of currents

I above about 0.6 A, evidence that nonradiative losses become much stronger because of heating of the diode at high pump currents ($I>0.6$ A). For shorter pulses, heating of the diode begins to show up at large currents, and the output power of the diode increases virtually linearly with current to (1–2) A. As a whole, the measurements showed that saturation of the watt–ampere characteristics of the LEDs at high pump levels weakens for pulses shorter than 0.5 ms.

The dependence of the output power on the inverse duty factor of the current was studied at various current amplitudes of 0.4, 1, and 2 A (see inset in Fig. 2). In the inset, the squares correspond to the supply regime in which the inverse duty factor was varied by varying the current pulsewidth while the pulse-repetition rate was fixed at 130 Hz. The triangles correspond to a variable repetition rate and a constant current pulsewidth of 1 μs. All the dependences exhibited the following common features: The maximum peak power was attained under supply conditions in which the inverse duty factor was about 10^2. When this value was exceeded, we observed saturation and falloff of the output optical power (see the behavior found for injection currents of 0.4 and 1 A in the inset to Fig. 2). The observed limitations apparently arise, on one hand, because the pulsewidth begins to approach the intrinsic carrier lifetime and, on the other hand, from the limitation of the passband of the recording system. The maximum optical power attained was 2.4 mW at $I=2$ A, $\tau=5.0$ μs, and $f=130$ Hz (an inverse duty factor of 1.6×10^2). It should be pointed out that the given value exceeds the output optical power of HgCdTe LEDs, about 0.048 mW ($\lambda=3.2$ μm, $I=15$ mA), larger pump currents of which were impossible because of high series resistance ($R\sim80$ Ω).[3] Moreover, the powers obtained in this paper are attractive by comparison with the results obtained earlier on InAs/InAsSbP LEDs: about 0.031 mW,[5] 0.33 mW ($I=400$ mA, inverse duty factor about 6),[6] 0.4 mW ($I=200$ mA, inverse duty factor about 2),[7] and 0.05 mW ($I=100$ mA dc)[8] at room temperature and the same wavelengths.

Thus, we have created LEDs with an emission maximum at a wavelength of 3.3 μm and a spectral width (FWHM) of 0.5 μm. The diodes were developed for portable gas analyzers to determine when the maximum permissible concentration is exceeded for the hydrocarbons methane, ethane, propane, and other gases. It has been shown that a continuous optical power of 0.13 mW (dc) and a maximum peak optical power of 2.4 mW (pulsewidth about 5.0 μs, inverse duty factor about 10^2) can be attained at room temperature in diodes based on an InAs/InAsSbP double heterostructure. The character of the dependence of the optical power of the LEDs on the pump-pulse parameters has been demonstrated.

[1] L. S. Rothman, R. R. Gamache, R. H. Tipping, C. P. Rinsland, M. A. H. Smith, D. Chris Benner, V. Malathy Devi, J.-M. Flaud, C. Camy-Peyret, A. Goldman, S. T. Massie, L. R. Brown, and R. A. Toth, J. Quantum Spectrosc. Radiat. Transfer **48**, 469 (1992).
[2] A. Mabbit and A. Parker, Sens. Rev. **16**, 38 (1996).
[3] E. Hadji, J. Bleuse, N. Magnea, and J. L. Pautrat, Appl. Phys. Lett. **67**, 2591 (1995).
[4] N. P. Esina, N. V. Zotova, B. A. Matveev, N. N. Stus', G. N. Talalakin, and T. D. Abishev, Pis'ma Zh. Tekh. Fiz. **9**, No. 7, 391 (1983) [Sov. Tech. Phys. Lett. **9**, 167 (1983)].
[5] A. N. Baranov, A. N. Imenkov, O. P. Kapranchik, V. V. Negreskul, A. G. Chernyavskiĭ, V. V. Sherstnev, and Yu. P. Yakovlev, Pis'ma Zh. Tekh. Fiz. **16**, No. 16, 42 (1990) [Sov. Tech. Phys. Lett. **16**, 618 (1990)].
[6] M. K. Parry and A. Krier, Electron. Lett. **30**, 1968 (1994).
[7] B. Grieteus, S. Nemeth, and G. Borghs, International Conference on Mid-Infrared Optoelectronics. Materials and Devices, Lancaster, UK, Sept. 17–18, 1996.
[8] B. A. Matveev, G. A. Gavrilov, N. V. Zotova, S. A. Karandashov, G. Yu. Sotnikova, N. M. Stus', and G. N. Talalakin, International Conference on Mid-Infrared Optoelectronics. Materials and Devices, Lancaster, UK, Sept. 17–18, 1996.
[9] A. Popov, V. Sherstnev, Yu. Yakovlev, A. Baranov, and C. Alibert, Electron. Lett. **30**, 86 (1997).
[10] A. M. Litvak, M. V. Stepanov, V. V. Sherstnev, and Yu. P. Yakovlev, Zh. Prikl. Khim. **67**, 1957 (1994).
[11] A. A. Andaspaeva, A. N. Baranov, A. A. Guseĭnov, A. N. Imenkov, N. M. Kolchanova, and Yu. P. Yakovlev, Fiz. Tekh. Poluprovodn. **24**, 1708 (1990) [Sov. Phys. Semicond. **24**, 1067 (1990)].

Translated by W. J. Manthey
Edited by David L. Book

Vibrational instability of the charged interface of immiscible electrically conductive liquids

A. I. Grigor'ev, D. F. Belonozhko, S. O. Shiryaeva, and S. I. Shchukin

Yaroslavl State University
(Submitted April 14, 1997)
Pis'ma Zh. Tekh. Fiz. **23**, 32–36 (November 12, 1997)

This paper shows that, in an electrostatic field normal to the flat interface of two viscous electrically conductive liquids, an oscillatory instability of the interface with periodically increasing amplitude can be produced when the electrical conductivity of the upper liquid is substantially greater than that of the lower one. Results are obtained by numerical analysis of the dispersion equation. © *1997 American Institute of Physics.*
[S1063-7850(97)00611-3]

The problem of the stability of the interface of two immiscible liquids that differ in their physicochemical characteristics appears in explaining the ''Dead Sea'' effect,[1] in Rayleigh–Taylor instability theory, in the implosion method of a nuclear explosion,[2] in inertial thermonuclear fusion,[3] and in studying the stability of the interfaces of a multilayer liquid undergoing acceleration.[4] Adding to the system an electrostatic field normal to the interface naturally does not simplify the problem, since the possibility appears of developing instability with respect to the charge accumulated at the interface.[5,6] As will be shown below, besides aperiodic instability of the Tonks–Frenkel type,[5,6] it is possible in the system described here to have oscillatory instability.

The following discussion is based on a model of incompressible viscous conductive liquids filling all of space in a gravitational field. Let the unperturbed interface between the liquids coincide with the XY plane of a Cartesian coordinate system whose Z axis is directed upwards in the direction opposite to that in which the gravitational field acts. The upper liquid, with kinematic viscosity ν_1 and density ρ_1, filling half-space $z>0$, is considered electrically conductive with conductivity σ_1 and permittivity ε_1. The lower liquid fills the half-space $z<0$ and possesses kinematic viscosity ν_2, density ρ_2, permittivity ε_2, and conductivity σ_2. We also assume that the unperturbed interface of the liquids is homogeneously charged with surface charge density $\varkappa$ and possesses surface tension with coefficient γ. We call the electrostatic fields in the upper and lower regions E_1 and E_2, respectively.

The dispersion equation that describes the capillary motion of the liquid in the system under discussion, taking into account the electric-charge relaxation effect, has the form[7]

$$
\begin{aligned}
&-\alpha^2[s^2(1+s\beta)n+sk\theta d]-sk^3H\Lambda\\
&+(1+s\beta)^2[s^4(\rho+1)n-4s^2k^3\nu^2(\rho-1)^2d\\
&+4s^3k^2\nu(\rho-1)m+4\rho s^4k]\\
&+(1+s\beta)[s^3k^2\theta n+s^3k\theta(\rho+1)d\\
&+k^2(H+\Lambda s)(s^2m-2sk\Theta\nu(\rho-1)d)]=0, \qquad (1)
\end{aligned}
$$

where the following notation has been used:

$$
\begin{aligned}
&n=\rho(\sqrt{k^2+s/\nu_2}-k)+(\sqrt{k^2+s/\nu_1}-k),\\
&m=\rho(\sqrt{k^2+s/\nu_2}-k)-(\sqrt{k^2+s/\nu_1}-k),\\
&d=(\sqrt{k^2+s/\nu_1}-k)(\sqrt{k^2+s/\nu_1}-k),\\
&\alpha^2=(1+s\beta)[k(\rho-1)-k^3]+k^2F,\\
&\sigma=\frac{\sigma_1}{\sigma_2},\quad \varepsilon=\frac{\varepsilon_1}{\varepsilon_2},\quad \beta=\frac{\varepsilon_1+\varepsilon_2}{4\pi(\sigma_1+\sigma_2)},\quad \rho=\rho_1,\\
&\theta=W(1-\varepsilon\sigma)\beta\left(1-\frac{1+\sigma}{1+\varepsilon}\right),
\end{aligned}
$$

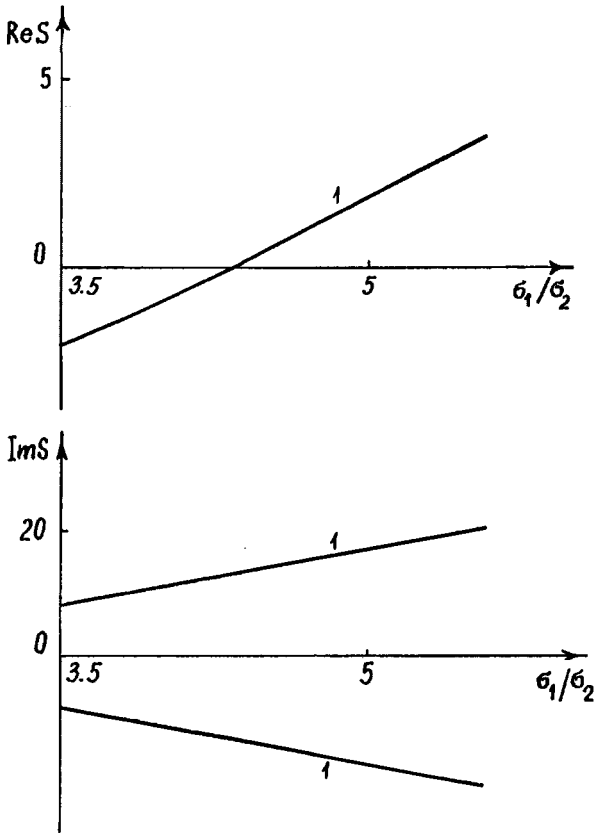

FIG. 1. The real component $\mathrm{Re}S=\mathrm{Re}S(\sigma_1/\sigma_2)$ and the imaginary component $\mathrm{Im}S=\mathrm{Im}S(\sigma_1/\sigma_2)$ of the frequency of capillary motions of a liquid vs the ratio of the conductivities of the upper liquid, σ_1, to that of the lower liquid, σ_2, for $k=1$, $\nu=0.1$, $\varepsilon=0.1$, $\rho=0.01$, $\beta=0.01$, and $W=2.15$.

$$\Lambda = W(1-\varepsilon\sigma)\beta\left(1-\frac{1-\sigma}{1+\varepsilon}\right),$$

$$F = W(1-\sigma)\left(s\beta\frac{1-\sigma}{1+\varepsilon}+\frac{1+\varepsilon\sigma^2}{1+\sigma}\right),$$

$$H = W(1-\varepsilon\sigma)\left(s\beta\left[1-\frac{1-\sigma}{1+\varepsilon}\right]+\frac{2\sigma}{1+\sigma}\right),$$

$$W = \frac{\varepsilon_1 E_{10}^2}{4\pi}.$$

Dimensionless variables in which $g=\rho_2=\gamma=1$ were used in writing dispersion Eq. (1), where the characteristic scales of the dimensional quantities have the form

$$s_* = \left(\frac{\rho_2 g^3}{\gamma}\right)^{1/4}, \quad k_* = \left(\frac{\rho_2 g}{\gamma}\right)^{1/2}, \quad \rho_* = \rho_2,$$

$$\nu_{1*} = \frac{\gamma}{\rho_2 g^3}, \quad \nu_{2*} = \frac{\gamma}{\rho_2 g^3}, \quad \beta_* = \left(\frac{\gamma}{\rho_2 g^3}\right)^{1/4},$$

$$W_* = \sqrt{\rho g \gamma}.$$

Numerical analysis of the dispersion equation (1) shows that, besides the usual spectrum of capillary wave motions produced in such systems (for example, see Refs. 8 and 9), wave motions with exponentially increasing amplitude appear in the system when the densities are small and the electrical conductivities of the upper medium are large; i.e., oscillatory instability of the interface manifests itself, as can be seen from Fig. 1. The physical meaning of the appearance of oscillatory instability in an electrostatic field normal to the interface is associated with the excitation of thermal capillary waves by waves of electric charge redistributed along the interface (accompanied by pressure waves of the electric field). When the electrical conductivity of the upper medium is much greater than that of the lower medium, the wave of the redistributed charge in the upper medium outruns that for the lower medium and transmits additional energy to it. But if the density of the upper medium is much less than that of the lower medium (as is true in the case analyzed here), the interface develops an oscillatory instablity. To all appearances, it is just such instability that appeared in the experiments of M. D. Gabovich *et al.*[10,11]

[1] L. N. Sretenskiĭ, *Theory of the Wave Motions of a Liquid* (Nauka, Moscow, 1977).
[2] E. Fermi, *Collected papers (Note e memorie)* (University of Chicago Press, Chicago, 1962–65; Nauka, Moscow 1972), pp. 490–501 [Russian].
[3] M. Sapir and D. Havazelet, J. Phys. D **18**, 41 (1985).
[4] M. J. Lyell and M. Roh, AIAA J. **29**, 1894 (1991).
[5] L. Tonks, Phys. Rev. **48**, 562 (1935).
[6] Ya. L. Frenkel', Zh. Éksp. Teor. Fiz. **6**, No. 4, 348 (1936).
[7] J. R. Melcher and C. V. Smith, Phys. Fluids **12**, 778 (1969).
[8] O. A. Grigor'ev and S. O. Shiryaeva, Izv. Ross. Akad. Nauk SSSR MZhG No. 1, 98 (1996).
[9] S. O. Shiryaeva, A. I. Grigor'ev, V. A. Koromyslov, Pis'ma Zh. Tekh. Fiz. **22**, No. 4, 89 (1996) [Tech. Phys. Lett. **22**, 173 (1996)].
[10] M. D. Gabovich and V. Ya. Poritskiĭ, PisUma Zh. Éksp. Teor. Fiz. **33**, 320 (1981) [JETP Lett. **33**, 304 (1981)].
[11] M. D. Gabovich and V. A. Khomich, Pis'ma Zh. Tekh. Fiz. **13**, 673 (1987) [Sov. Tech. Phys. Lett. **13**, 279 (1987)].

Translated by W. J. Manthey
Edited by David L. Book

Global stochastic particles in a field-reversed configuration

V. I. Khvesyuk, A. V. Khvesyuk, and A. N. Lyakhov

High-Energy Machine Construction Research Institute, N. É. Bauman Moscow State Technical University
(Submitted October 23, 1996)
Pis'ma Zh. Tekh. Fiz. **23**, 37–39 (November 12, 1997)

This paper discusses the dynamics of the fusion products of the D–He^3 reaction in a field-reversed configuration, with application to a reactor regime with a large value of the plasma β. It shows that, under the conditions in the Artemis-L design [H. Momota and Y. Tomita, J. Plasma Fusion Res. **69**, 801 (1993)], the motion of protons with an initial energy of 14.1 MeV is strongly stochasticized. The confinement time of these particles and the energy transfer from the fusion products to the plasma are very small. © *1997 American Institute of Physics.* [S1063-7850(97)00711-8]

According to the design concept of Artemis-L,[1] the value of β for a D–He^3 reactor based on a field-reversed configuration (FRC) must be about 0.9, while the external magnetic field in the symmetry plane of the trap (outside the separatrix) is $B=6.7$ T. In connection with the development of the concept of a D–He^3 reactor based on an FRC, one of the important problems is to calculate the energy exchange between the fusion products (protons and alpha particles) and the plasma. In this connection, the present paper discusses the proton dynamics under such conditions.

Note that the dynamics of the particles in an FRC have been studied in a number of papers.[2,3] However, questions associated with the confinement of the high-energy products of the D–He^3 reaction as applied to an FRC have not yet been analyzed. This paper uses the model of Ref. 4 of the magnetic field for an FRC (Fig. 1), which takes into account

- the presence of a magnetic field both inside and outside the separatrix,
- the finite value of the plasma β and the attenuation of the magnetic field inside the separatrix caused by this value, and
- the geometrical size and the magnitude of the external magnetic field in the symmetry plane of the FRC, corresponding to the design of Artemis-L.[1]

The stream function of the magnetic field inside the separatrix was taken in the form[4]

$$\psi(r,z)=\frac{B_0 r^2}{2}\left[1-\left(\frac{r}{a}\right)^2-\left(\frac{z}{b}\right)^4\right], \tag{1}$$

where $B_0=2T$. The field created by the magnetic system is $B_z(r=a_w,z=0)=6.7$ T; $a=1$ m, and $b=8$ m.[1]

The results of the calculations showed that taking into account the attenuation of the internal magnetic field causes the motion of the high-energy protons to be highly nonadiabatic. The result that their motion is stochastized at an energy of 14.1 MeV. Figure 2 shows the trajectory of a proton with such an energy on the $R-Z$ plane. A particle in motion, in a manner of speaking, feels the entire surface of the separatrix, finds the narrow opening in the magnetic field near the X point, and leaves the plasma. It can be seen that the trajectory of such particles covers the entire volume of the plasma. We therefore propose to call them ''global stochastic particles,'' in distinction to local stochastic particles, which are confined in the reactor.

As a rule, the confinement time of such protons is less than $\tau_e \sim 10^{-4}$ sec. However, the characteristic relaxation time (for the case of a thermonuclear plasma with a density of $n_0 \approx 10^{21}$ m^{-3}) is $\tau_s \approx 0.6$ sec. The global stochastic particles (the fusion products) will consequently transfer only a small part of their energy to the plasma.

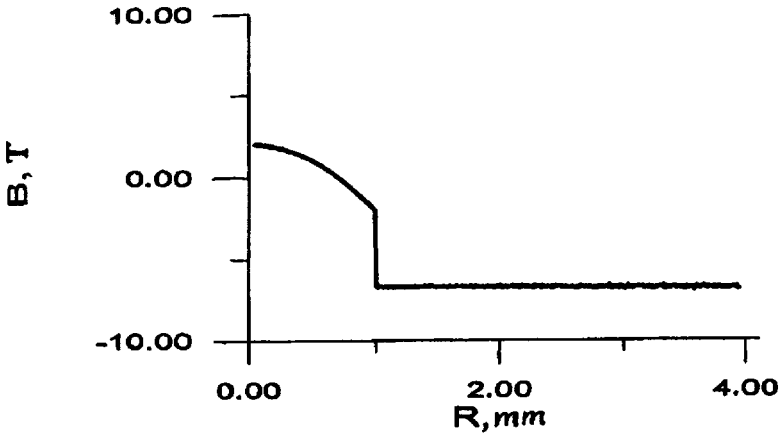

FIG. 1. Radial distribution of the magnetic field in a field-reversed configuration.

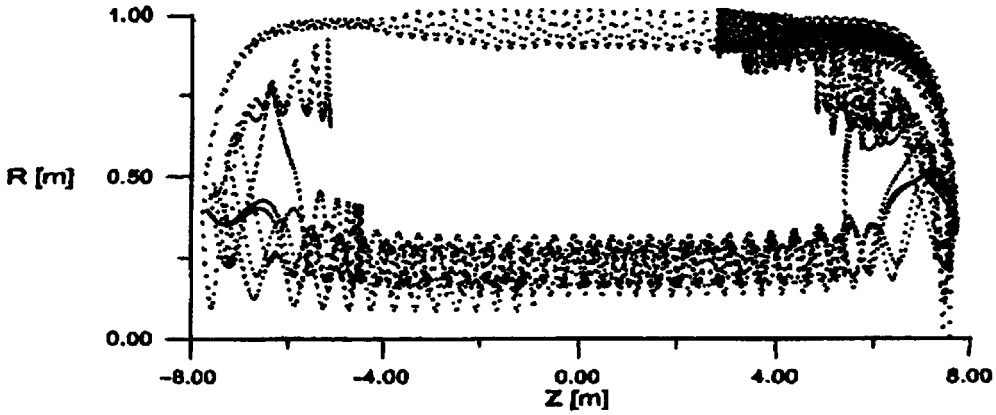

FIG. 2. Stochastic motion of a high-energy proton with $E = 14.1$ MeV.

Note that increasing the magnetic field inside the separatrix by a factor of 2–3 provides substantially better confinement of the high-energy protons. Such an increase can be produced either by reducing the β of the plasma for the given external field of 6.7 T or by increasing the external magnetic field while maintaining the β of the plasma. Thus, in estimating the given values of the magnetic field in the D–He^3 plasma of an FRC, it is necessary to take into account the possibility of global stochastization of the reaction products.

[1] H. Momota and Y. Tomita, J. Plasma Fusion Res. **69**, 801 (1993).
[2] M. Y. Hsiao and G. H. Miley, Nucl. Fusion **24**, 1029 (1984).
[3] M. Y. Hsiao and G. H. Miley, Phys. Fluids **28**, 1440 (1985).
[4] L. Steinhauer, Phys. Fluids B **2**, 3081 (1990).

Translated by W. J. Manthey
Edited by David L. Book

Effect of the post-growth defect system on the orientation of a flat interphase boundary in $PbTiO_3$ crystals

E. A. Dul'kin and V. G. Gavrilyachenko

Scientific Research Institute of Mechanics and Applied Mathematics, Rostov State University
(Submitted October 30, 1996; accepted for publication June 11, 1997)
Pis'ma Zh. Tekh. Fiz. **23**, 40–44 (November 12, 1997)

Optical microscopy and acoustic emission have been used to study the phase transition in $PbTiO_3$ crystals. It is established that the acoustic-emission activity depends on the angle between the normal to the interphase boundary and the direction of a uniform temperature gradient. It is shown that the orientation of the interphase boundary is determined by the post-growth defect system of the crystals. © *1997 American Institute of Physics.* [S1063-7850(97)00811-2]

It is known that a phase transition occurs in $PbTiO_3$ crystals because of the displacement of one or several flat interphase boundaries. In lamellar crystals with dimensions $a>b\gg h$ ([001] axis along h), in the most general case, differently oriented interphase boundaries appear simultaneously during the phase transition because of the different growth rates along the indicated axes. By placing a lamellar crystal in the field of a uniform temperature gradient ∇T and rotating it around an axis perpendicular to the developed faces, it is possible to observe the successive formation of interphase boundaries of definite orientations.[1]

In certain crystals that initially have an $a-c$ domain structure in which the c domains dominate, it was observed that when an isothermal surface was oriented along (010), a (023) interphase boundary formed in the crystals. When an isothermal surface occupied the (230) position, instead of an interphase boundary with the same indices, an interface boundary appeared consisting of a combination of (023) and (320) boundaries. When an isothermal surface was oriented along (320), an interface boundary with the same indices appeared in the crystals. When the crystals were rotated further, single wedges appeared, limiting sections of the (320) and (230) boundaries. After a complete rotation by 90°, when an isothermal surface occupied a (100) position, the number of wedges increased, and the interphase boundary became complicated. The appearance of 90° wedge-shaped twins displaced behind the interphase boundary was observed in the ferroelectric phase, while the crystals became a-domain.

To explain the observed features of the formation of the interphase boundary, Ref. 1 assumed that conditions were created during bulk crystallization in which a definite system of defects arises that acts similarly to mechanical clamping and impedes the crystals from lengthening in the direction of the most rapid growth (the [010] axis, along a), thereby limiting the possible positions of the interphase boundary. A similar phenomenon has also often been observed in virgin crystals with an initial a-domain structure.

To experimentally check the given assumption, we used acoustic emission, whose high sensitivity made it possible to establish the effect of the post-growth defect system on the process of phase work-hardening in $PbTiO_3$ crystals.[2] We studied specially chosen virgin a-domain $PbTiO_3$ crystals by the technique of Ref. 3. The crystal is placed on the polished end of a quartz acoustic waveguide introduced from below into a furnace mounted on the chassis of a polarization microscope. The flat heaters of the furnace are arranged symmetrically along both sides of the waveguide and are supplied from two adjustable independent current sources, which makes it possible to create a temperature gradient. We simultaneously measured the acoustic-emission activity $\dot{N}$ and observed the interphase boundaries of the crystals as they underwent a phase transition to the ferroelectric phase in the field of a temperature gradient $\nabla T=15$ °C/cm with a heating and cooling rate of 1–2 °C/min.

Microphotographs of one of the crystals as it was successively rotated around the [001] axis are shown in Fig. 1a, and the corresponding acoustic-emission values $\dot{N}$ appear in Fig. 2. A (023) interphase boundary and the corresponding

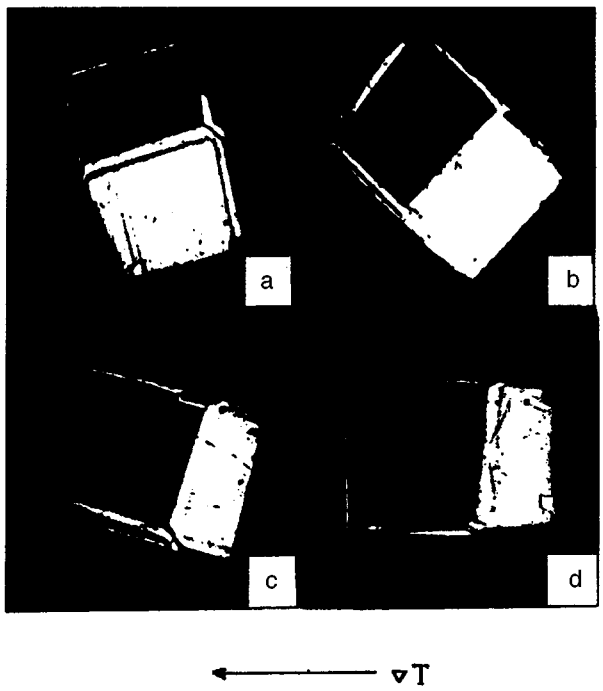

FIG. 1. Microphotographs of the (023) interphase boundary, which maintains its orientation as the a-domain crystal $PbTiO_3$ rotates relative to the direction of temperature gradient ∇T (magnification ×20).

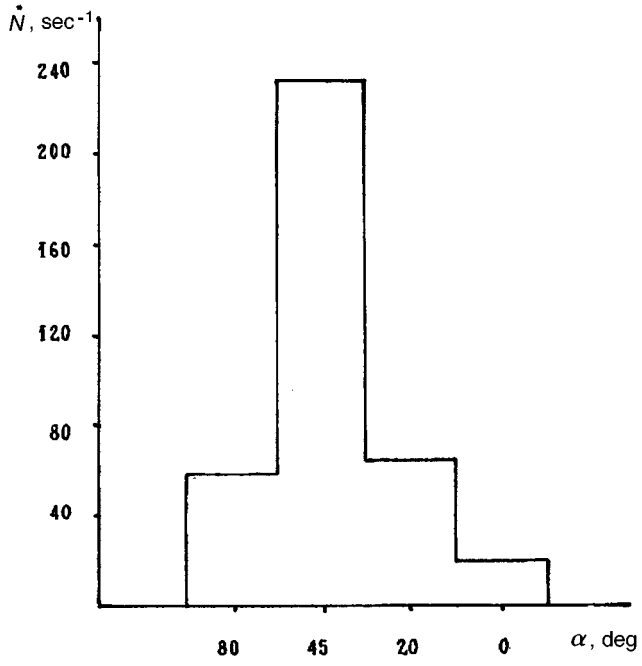

FIG. 2. Acoustic-emission activity $\dot{N}$ vs angle α between the normal to the interphase boundary and the direction of temperature gradient ∇T for successive rotations of an a-domain $PbTiO_3$ crystal around the [001] axis.

$a-c$ domain structure (Fig. 1a) were formed in the crystal during the first thermal cycle. However, after the phase transition was complete, the initial a-domain structure was restored in the crystal. When the crystal was rotated further, only a (023) interphase boundary was formed (Figs. 1b–1d), and the a-domain structure was restored after each phase transition. Optical observations showed that the interphase boundary moved smoothly, without slowdowns or jerks, at approximately the same rate for all angles between [010] and ∇T.

However, the $\dot{N}(\alpha)$ dependence has an extremal character (Fig. 2). As can be seen, as rotation progresses, $\dot{N}$ increases and reaches a maximum at $\alpha=45°$, which corresponds to the maximum angle between the interphase boundary and ∇T, and then again decreases. Similar dependences are observed in the other quadrants: $\dot{N}$ has maxima at $\alpha=135°$, 225° and 315°. A repeated complete rotation confirmed this result, but, when a third rotation was attempted, a crack appeared in the crystal at $\alpha=45°$, cleaving the phase boundary, and further investigation became meaningless.

The observed constancy of the domain structure and the position of the interphase boundary confirm the assumption that the post-growth defect system exerts blocking action similar to clamping of the crystal. Since, in this case, it is the c component that disappears in the phase structure after the phase transition is complete, it is obvious that this clamping occurs over the thickness of the crystal. The increase of $\dot{N}$ at definite rotation angles corresponds to strengthening of the dislocation generation[4] as a result of relaxation of the mechanical stresses developed during the attempt of the interphase boundary to reorient itself to correspond to ∇T.

It is also obvious that it is the evolving stresses that cause the crystals to fracture. Earlier studies show that many $PbTiO_3$ crystals do not survive long thermal cycling but usually fracture.[5] As shown in this paper, virgin a-domain $PbTiO_3$ crystals do not survive even a few cycles, which is explained by the high density of their post-growth defects.

[1] E. G. Fesenko, V. G. Gavrilyachenko, and A. F. Semenchev, *Domain Structure of Multiaxial Ferroelectric Crystals* [in Russian] (Izd. RGU, Rostov-on-Don, 1990).
[2] V. G. Gavrilyachenko, E. A. Dul'kin, and A. F. Semenchev, Fiz. Tverd. Tela **37**, 1229 (1995) [Phys. Solid State **37**, 668 (1995)].
[3] E. A. Dul'kin, V. G. Gavrilyachenko, A. F. Semenchev, Fiz. Tverd. Tela **34**, 1628 (1992) [Phys. Solid State **34**, 863 (1992)].
[4] V. S. Boyko, R. I. Garber, A. M. Kossevich, *Reversible Crystal Plasticity* (American Inst. of Physics, New York, 1994).
[5] E. A. Dul'kin, Kristallografiya **39**, 738 (1994) [Crystallogr. Rep. **39**, 669 (1994)].

Translated by W. J. Manthey
Edited by David L. Book

Structure of the short-lived absorption and luminescence spectra of barium and calcium fluorides accompanying pulsed electron irradiation

V. F. Shtan'ko and E. P. Chinkov

Tomsk Polytechnic University
(Submitted April 28, 1997)
Pis'ma Zh. Tekh. Fiz. **23**, 45–50 (November 12, 1997)

It is established that the optical absorption in the hole and electron components of autolocalized excitons in BaF_2 excited by a pulsed electron beam consists of a collection of overlapping bands with a half-width no greater than 0.1 eV. Simultaneous subexcitation with the stimulated emission of II–VI semiconductors made it possible to isolate three groups of bands, caused, by analogy with CaF_2 [Phys. Solid State **39**, 1060 (1997)], by different configurations of autolocalized excitons in the fluorite lattice. The process of radiative decay of autolocalized excitons in CaF_2 and BaF_2 when they are optically excited in the region of the electron component of the absorption has been detected. The spectral rate parameters of the radiation that appears during simultaneous subexcitation coincide with the characteristics of the radiation ascribed earlier to core–valence transitions. The photostimulated variation of the absorption spectra of autolocalized excitons is accompanied by selective variation of the luminescence spectra of autolocalized excitons, which also is evidence of their complex spectral content. © *1997 American Institute of Physics.* [S1063-7850(97)00911-7]

In studying the formation mechanisms of the primary products of the radiolysis of complex substances, the problem arises of analyzing the absorption and luminescence spectra. It is usually solved by using the Alentsev–Fock method.[1] Spectra with a complex spectral and kinetic content can be analyzed by the double excitation method[2], in which the first (radiation) pulse is used to create defects, and the second (laser) pulse is used to subexcite them. However, a set of lasers with tunable wavelength and with sufficient emission power is needed for selective excitation in a wide spectral range, and this complicates the technique and causes material expenditures.

The problem of selective subexcitation can be solved by using the pulsed cathodoluminescence of direct semiconductors from the II–VI group (and their solid solutions) and the III–V group, which have a stimulated character at high excitation levels ($W>0.05$ J/cm^2).[3,4] The absolute energy output of the stimulated emission increases with increasing excitation density all the way to the threshold values that cause brittle breakdown of the material, while the energy reaches tens of millijoules.[3] This set of semiconductors makes it possible to obtain stimulated emission in the spectral range 1.6–3.7 eV.[5] The position of the maximum of the stimulated emission spectrum is fine-tuned by choosing the geometry and the excitation density.[4]

The stimulated emission of ZnSe ($h\nu_{\max}=2.609$ eV, $\delta=0.011$ eV) and CdSe ($h\nu_{\max}=1.854$ eV, $\delta=0.015$ eV) is used in this paper to study the short-lived absorption and luminescence spectra of barium and calcium fluorides excited by a pulse of accelerated electrons with the parameters $E_{\max}=0.26$ MeV, $t=12$ ns, and $W=0.2$ J/cm^2. The technique of precision measurements of the spectrum is similar to that used in Ref. 6. The samples for the studies were nominally pure crystals grown by the Stockbarger method. The residual impurity concentration was less than 10^{-5} mol%. The luminescence spectra were not corrected.

Electron irradiation of the fluorites at room temperature results in the formation of autolocalized excitons.[7,8] Their optical absorption and luminescence spectra are ordinarily represented as broad bands with weakly resolved structure, which is usually ascribed to measurement errors.

Figure 1 (curve *1*) shows the optical absorption spectra of a BaF_2 crystal, measured 10 ns after the end of a pulse of electrons. It can be seen from the data of the figure that the spectrum has a complex spectral content, even though in form (the envelope of the bands) it qualitatively matches those measured earlier.[7,8] Moreover, we were the first to detect absorption in the $h\nu>5$ eV region, which is characterized by a shorter relaxation time ($\tau\leqslant 100$ ns) than the autolocalized exciton lifetime ($\tau=400$ ns, $h\nu=4.5$ eV, $T=295$ K).

The use of the Alentsev–Fock method made it possible[6] to partially resolve the complex absorption spectrum in the CaF_2 crystal into groups of bands in which one transition from the region of the electron component of the autolocalized exciton absorption corresponded to two or three transitions from the region of the hole component. The complex spectral content of the short-lived absorption in the BaF_2 crystal (Fig. 1, curve *1*) suggests that such transitions (groups of bands) are present, but they are hard to isolate because of strong overlap and similar decay coefficients.

Simultaneous subexcitation of the BaF_2 crystal with CdSe radiation results in selective variations (Fig. 1, curve *2*) in the short-lived absorption spectrum and promotes a more distinct resolution of the total spectrum into separate bands. The arrows in Fig. 1 show groups of bands isolated according to the relative increase (decrease) of the optical density during subexcitation.

The use of optical subexcitation also makes it possible to explain the complex content of the luminescence spectrum of autolocalized excitons in BaF_2 ($h\nu_{\max}=4$ eV, $\tau=400$ ns, $T=295$ K): Both increases and decreases (about 4 eV) in the luminescence intensity can be observed over the spectrum

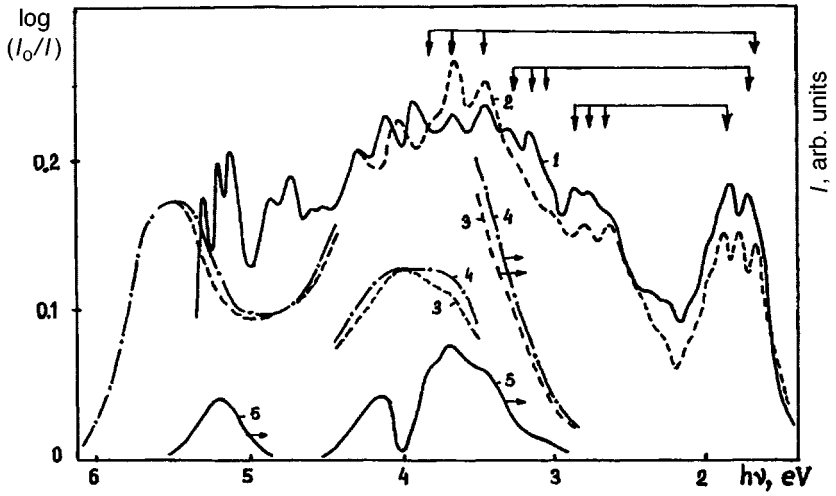

FIG. 1. Optical absorption spectra (*1*, *2*) and luminescence spectra (*3*, *4*) of a BaF_2 crystal measured at 295 K 10 ns after the end of a pulse of accelerated electrons. Spectra *2* and *4* are measured with simultaneous subexcitation by CdSe radiation. Curve *5* is the difference of spectra *3* and *4*.

(Fig. 1, curves *3*–*5*). Moreover, in the region of rapidly damped luminescence ($h\nu_{\max}=5.6$ eV, $\tau<1$ ns), whose nature has not been conclusively established,[8,9] a band can be distinguished with a maximum at about 5.2 eV, in which the luminescence damping time was less than the time resolution of the measurement channel (about 10 ns). The appearance of this luminescence is unambiguous evidence of radiative recombination of autolocalized excitons from excited states populated during optical subexcitation in the electron component of the absorption.

A similar radiative decay effect of autolocalized excitons is detected in a CaF_2 crystal when it is optically subexcited by stimulated ZnSe emission (see the inset in Fig. 2). Unlike BaF_2, rapidly damped luminescence in CaF_2 appears only during subexcitation and has a complex spectral content. We assume that this is associated with more efficient de-exciting action of ZnSe radiation on CaF_2 crystals. Actually, it can be seen from the data in Fig. 2 that optical subexcitation is accompanied by selective changes (curve *3*) over the entire spectrum (compare curves *1* and *2*). The application of the Alentsev–Fock method to resolve the spectrum obtained using the subexcitation of CaF_2 by ZnSe radiation makes it possible to explain the more complex structure in the region of the electron component of the absorption of autolocalized excitons (curve *4*), which substantially supplements the data of Ref. 6.

Thus, the use of the pulsed cathodoluminescence of semiconductors as a source of selective subexcitation has made it possible for the first time to establish the presence of complex structure in the optical absorption and luminescence spectra of autolocalized excitons in BaF_2, to additionally interpret the spectral structure in the region of the electron component of the absorption of autolocalized excitons in CaF_2, and to detect the photostimulated radiative decay of autolocalized excitons both in BaF_2 and in CaF_2. The resulting regularities require a substantial correction to be made in the concepts of the structure of autolocalized excitons in crystals with the fluorite lattice.

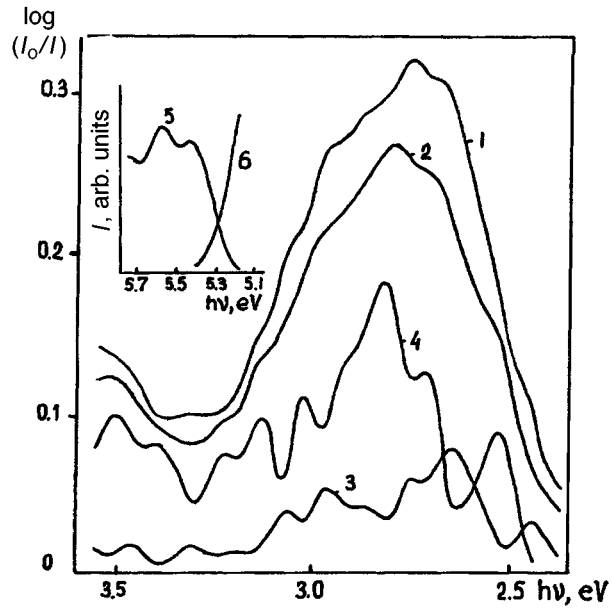

FIG. 2. Optical absorption spectra (*1*, *2*) of a CaF_2 crystal, measured at 295 K 10 ns after the end of a pulse of accelerated electrons. Spectrum *2* is measured with simultaneous subexcitation with ZnSe radiation. Curve *3* is the difference of spectra *1* and *2*. Curve *4* was obtained by resolving spectra *2* and *3* by the Alentsev–Fock method. The inset shows the spectral content of the fast (*5*) and slow (*6*) components of the luminescence damping of CaF_2 with simultaneous subexcitation by ZnSe radiation.

[1] M. V. Fock, Tr. Fiz. Inst. Akad. Nauk SSSR **59**, 3 (1972).
[2] T. Eshita, K. Tanimura, and N. Itoh, Phys. Status Solidi B **122**, 489 (1984).
[3] V. M. Lisitsyn, V. F. Shtan'ko, and V. Yu. Yakovlev, Zh. Tekh. Fiz. **55**, 1187 (1985) [Sov. Phys. Tech. Phys. **30**, 678 (1985)].
[4] V. F. Shtan'ko, V. I. Oleshko, A. V. Namm *et al.*, Zh. Prikl. Spektrosk. **55**, 788 (1991).
[5] S. V. Korolev, I. M. Olikhov, and D. M. Petrov, Elektron. Prom. No 2, 22 (1973).
[6] E. P. Chinkov and V. F. Shtan'ko, Fiz. Tverd. Tela **39**, (1997) [Phys. Solid State **39**, 1060 (1997)].
[7] R. T. Williams, M. N. Kabler, W. Hayes *et al.*, Phys. Rev. B **14**, 725 (1976).
[8] I. P. Denisov, V. A. Kravchenko, A. V. Malovichko *et al.*, Fiz. Tverd. Tela **31**, No. 7, 22 (1989) [Sov. Phys. Solid State **31**, 1110 (1989)].
[9] Yu. M. Aleksandrov, V. N. Makhov, P. A. Rodnyĭ *et al.*, Fiz. Tverd. Tela **26**, 2875 (1984) [Sov. Phys. Solid State **26**, 1741 (1984)].

Translated by W. J. Manthey
Edited by David L. Book

Suppression of plasma fluctuations in the transition to the improved-confinement regime when the current is raised rapidly in the FT-2 tokamak

V. N. Budnikov, V. V. Bulanin, A. V. Vers, L. A. Esipov, E. R. Its, S. I. Lashkul, A. V. Petrov, and A. Yu. Tukachinskiĭ

St. Petersburg State Technical University, A. F. Ioffe Physicotechnical Institute, Russian Academy of Sciences, St. Petersburg
(Submitted July 4, 1997)
Pis'ma Zh. Tekh. Fiz. **23**, 51–57 (November 12, 1997)

Collective scattering of CO_2-laser radiation is used to study the microturbulence of the plasma in the FT-2 tokamak when the current is rapidly raised, while the magnetic-field shear is varied appreciably. The experiment exhibited suppression of the plasma fluctuations, the appearance time of which was correlated with the transition of the discharge to the improved-confinement regime. The resulting data are evidence that the suppression of the oscillations occurred predominantly in the central zone of the tokamak, and a suppression-extending phenomenon or hysteresis is detected. The evolution of the spectral characteristics of the fluctuations during the suppression is analyzed, using model calculations of the magnetic-field shear. © *1997 American Institute of Physics.* [S1063-7850(97)01011-2]

A transition to an improved-confinement regime in the central regions of the plasma has recently been attained on large tokamaks by creating negative magnetic-field shear (see, for example, Ref. 1). Strong suppression (by a factor of up to 40) of the transport rates of the charged particles and energy has been detected. In connection with these results, to elucidate how perturbations of the $q(r)$ profile affect plasma confinement in small tokamaks, experiments with a rapid rise of plasma current I_p were undertaken on the FT-2 tokamak ($R=5$ cm, $a=8$ cm, $B_t=2.2$ T).[2] A current increase ΔI_p from 22 to 30 kA maintained for 3 ms produced a transition to a regime with an increase by as much as a factor of 3 in the charged-particle lifetime and the ion energy. A similar transition was also observed in discharges which combined raising of the current and additional heating by rf radiation in the lower-hybrid range (LHR). The aggregate of experimental data[2] indicated that a transport barrier similar to that observed on large toroidal devices appears in the central regions of the discharge.

According to theoretical concepts, the transition to the improved-confinement regime is associated in the final analysis with suppression of turbulent fluctuations of the plasma.[4] To experimentally determine this connection, studies of the behavior of small-scale plasma turbulence (0.01–1 cm) were carried out on the FT-2 tokamak by the method of collective scattering of CO_2-laser radiation at small angles. The diagnostic system developed on the FT-2 permitted parallel analysis of the K spectrum of the fluctuations.[3] Homodyne detection was used to simultaneously record the scattering at fluctuations of four different spatial scales for the wave-number range $K_\perp=6.3$–40 cm^{-1} and in the frequency region from 0.02 to 2 MHz. The laser beam was directed along the central vertical chord of the minor cross section ($X=0$) and along peripheral chords at distances $X=+6$ cm and $+6.5$ cm from the axis of the discharge toward the outer circumference of the torus. At small scattering angles, under the conditions of the experiment on the FT-2, when the radiation scattered over the entire length of the laser beam in the volume of the plasma was measured, the power spectra $P_s(F)$ of the output signals of the detectors was determined from the integral of the local power spectrum of the electron-density fluctuations along the entire probing chord.

Figure 1a compares the time dependence of the relative value of $P_s/(\langle n_e\rangle)^2$, averaged in the band of frequencies F from 100 to 800 kHz, for an ohmic discharge and a discharge with a current increase of ΔI_p. The power is normalized to the square mid-chord plasma density $\langle n_e\rangle$ in order to eliminate from consideration the increase of P_s because of the increase of $\langle n_e\rangle$ always observed during a current rise and lower-hybrid heating. The data for the two wave numbers $K_\perp$ obtained by central probing ($X=0$) are represented in the same arbitrary units. It can be seen that switching on additional current immediately reduced the fluctuation level. It is noteworthy that a low turbulence level was maintained for a long time after the flat part of the additional current pulse ended.

This time dependence in the suppression of small-scale fluctuations correlates with a long time of existence of a high level of plasma density when improved confinement of charged particles occurs.[2] A decrease of the fluctuation intensity was also noted in combined discharges (LHR$+\Delta I_p$) (see Fig. 1b). This attenuation of the fluctuations was localized in the wave number range 15–25 cm^{-1}. As in the case with a current rise, the low fluctuation level was noted for a long time, which corresponded to the increase of the confinement time of the ion energy detected in the same discharges.[2] In considering the resulting data, it should be kept in mind that the radiation scattered in a volume extending along the entire vertical probing chord was recorded in the experiment. Therefore, the relatively small decrease of the output signals of the photodetectors (Fig. 1) can actually reflect the fact of strong suppression of the fluctuations in a narrow interval along the minor radius of the tokamak.

It was impossible to directly determine in the measurements the zone of greatest suppression. However, by shifting

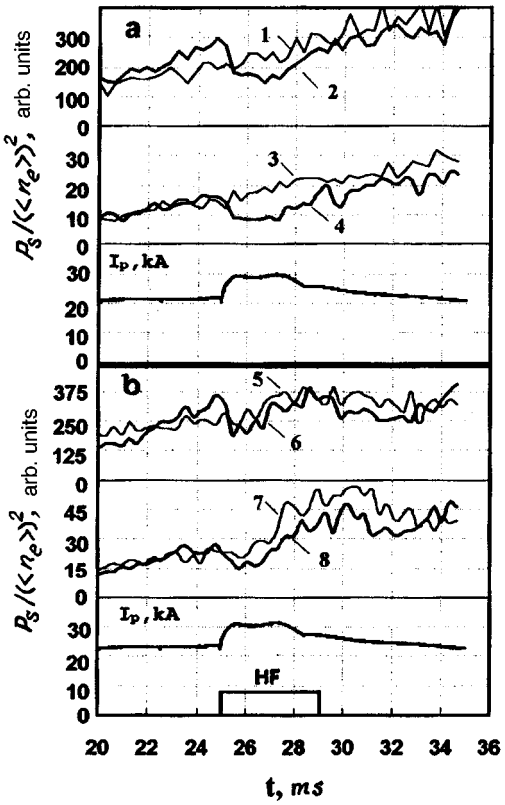

FIG. 1. (a) Time dependence of the relative value of $P_s/(\langle n_e\rangle)^2$ for the ohmic regime of the discharge (*1, 3*) and for a discharge with a current increase (*2, 4*) for central probing ($X=0$); $K_\perp = 12.7\ \mathrm{cm}^{-1}$ for *1* and *2*, and $K_\perp = 18.2\ \mathrm{cm}^{-1}$ for *3* and *4*. (b) The same in the ohmic (*5, 7*) and combined regimes (LHR+ΔI_p) (*6, 8*); *5, 6*—$K_\perp = 12.7\ \mathrm{cm}^{-1}$; *7, 8*—$K_\perp = 18.2\ \mathrm{cm}^{-1}$.

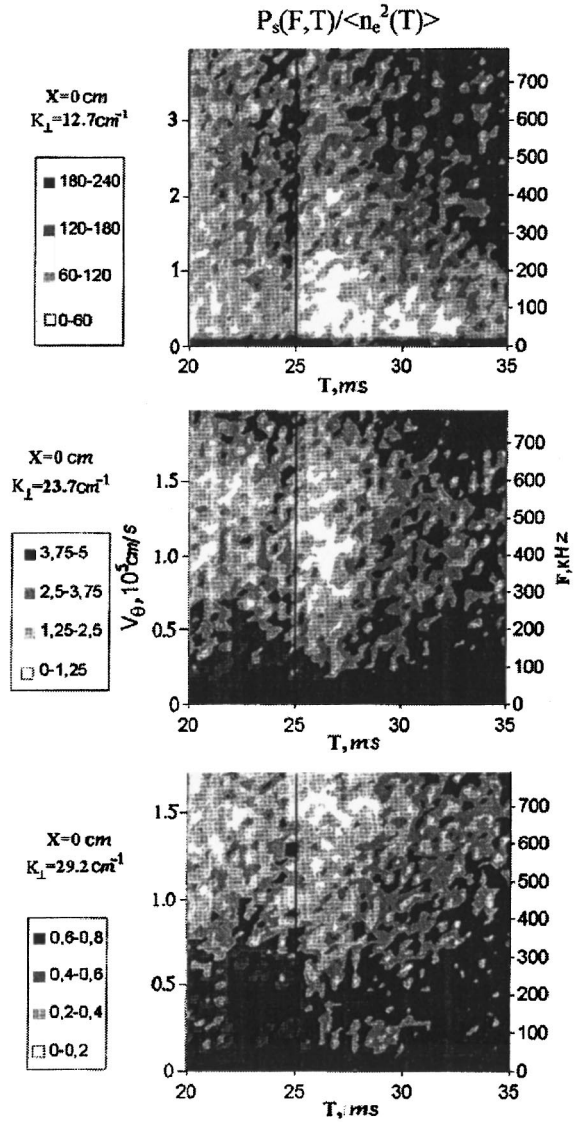

FIG. 2. Time evolution of the relative fluctuation spectra $P_s(F)/(\langle n_e\rangle)^2$ in a regime with a current rise with central probing.

the scattering volume along the major radius of the tokamak, it was possible to indirectly estimate the spatial region in which the microturbulence was suppressed. Measurements undertaken with this purpose, with peripheral placement of the probing chord, showed that the fluctuation level either does not change at all as the current is raised or decreases slightly only at the beginning of the additional current pulse. These data are apparently evidence that, at least 2 ms after the beginning of the current increase, the suppression of fluctuations, unlike the usual L–H transition (see Ref. 4) covers the central region of the discharge ($r<5$ cm).

Other indirect data on the position of the zone in which microturbulence is suppressed can be obtained from spectral measurements of the scattered radiation. Figure 2 shows the time evolution of the relative fluctuation spectra $P_s(F)/(\langle n_e\rangle)^2$ in the regime with a current rise, obtained with central probing. It can be seen that, with the beginning of the current rise, noted in Fig. 2 by a vertical line, the fluctuations begin to be suppressed in a wide frequency band. This band, which corresponds to a reduced oscillation level even in the ohmic stage of the discharge, is clearly displaced as $K_\perp$ increases toward higher frequencies. The spectral suppression zone becomes narrower after 3 ms but is observable up to 10 ms after the start of the additional current. The shift of the suppression region with increasing $K_\perp$ allows an interpretation based on the fact that the appearance of each frequency component in the spectra is determined by the Doppler shift $F = K_\perp V_\theta/2\pi$ (V_θ is the poloidal propagation rate of the oscillations), while the presence of many frequency components in the $P_s(F)$ spectrum for fixed $K_\perp$ is mainly associated with the radial inhomogeneity of V_θ in the scattering volume extending along the entire vertical chord. If P_s is represented in the form of a dependence on velocity V_θ (Fig. 2), it can be seen that the suppression at the initial stage of the current rise manifests itself for different $K_\perp$ in approximately the same wide region of velocities $V_\theta = 5\times10^4 - 2\times10^5$ cm/sec. As time passes, this interval narrows to a range close to $V_\theta \approx 10^5$ cm/sec. For a known radial profile $V_\theta(r)$, this range can be correlated in velocity with the region of suppression of fluctuations over the minor radius. According to neoclassical estimates, a velocity of 10^5 cm/sec corresponds to a gradient region with $r \approx 4$ cm.

Thus, suppression of small-scale plasma fluctuations is observed when the current is raised. The period during which this suppression is observed correlates with the time during which improved confinement of the charged particles and of

the ion energy appears. According to theoretical concepts, fluctuation suppression can be associated with the appearance of regions with negative or zero magnetic-field shear $s=(r/q)dq/dr$. The evolution of the $q(r)$ profile and accordingly of $s(r)$ under the conditions of the FT-2 tokamak were estimated by modelling the process of the current rise by means of the ASTRA code. This modelling showed that a region with a flattened distribution $s(r)>0$ appears at the beginning of the current pulse at the periphery of the discharge and, as time passes, moves toward the axis of the discharge, where a wide zone with $s\approx 0$ is formed in 1.5–2 ms. However, as can be seen from Fig. 2, strong suppression of the fluctuations in a wide spectral band was observed even before the appearance of the region with $s\approx 0$ in the central zone. It can be assumed that, under the conditions of the experiment, the suppression of oscillations is associated with a small time-dependent flattening of the profile with $s(r)>0$, which arise as the current diffuses. However, the fact that the fluctuations are immediately suppressed over a wide frequency region makes the assumption more likely that the decrease of the turbulence level is associated with rapid reconstruction of the rotational shear. Such a reconstruction can be expected, for example, because the rate of the Ware pinching varies when a strongly inhomogeneous longitudinal electric field appears in the plasma.[2] As shown by the modelling, the perturbed distribution $q(r)$ relaxes to the equilibrium steady-state profile corresponding to the total current in the plasma in the relatively short time of 5 ms. Therefore, the maintenance of a reduced fluctuation level at long times (>5 ms) is a form of hysteresis phenomenon, apparently not associated with the deformation of $q(r)$. Similar phenomena are noted in large tokamaks and are confirmed in various models of the transition to improved confinement (see, for example, Ref. 5).

This work was carried out with the support of the Russian Fund for Fundamental Research (Grant 97-02-18119), INTAS (Grant 94-2236), and INTAS–RFBI (Grant 95-1351).

[1] F.M. Levinton, M. C. Zarnstorff, S. H. Batha *et al.*, Phys. Rev. Lett. **75**, 4417 (1995).
[2] S. I. Lashkul, V. N. Budnikov, V. V. Bulanin *et al.*, Abstracts of the Twenty-Fourth European Physical Society Conference on Controlled Fusion and Plasma Physics, 1997, p. 199.
[3] V. N. Budnikov, V. V. Bulanin, V. V. Dyachenko *et al.*, in *Proceedings of the Twenty-Third European Physical Society Conference on Controlled Fusion and Plasma Physics*, 1996, V20C, pp. 855–858.
[4] K.H. Burrell, Phys. Plasmas **4**, 14909 (1997).
[5] V. Rozhanksy, M. Tendler, and T. Voskoboynikov, in *Proceedings of the Twenty-Third European Physical Society Conference on Controlled Fusion and Plasma Physics*, 1996, V20C, pp. 444–447.

Translated by W. J. Manthey
Edited by David L. Book

Zinc oxide whiskers

B. M. Ataev, I. K. Kamilov, and V. V. Mamedov

Physics Institute, Dagestan Scientific Center, Russian Academy of Sciences, Makhachkala
(Submitted April 29, 1997)
Pis'ma Zh. Tekh. Fiz. **23**, 58–63 (November 12, 1997)

This paper describes the first experiments on the production of zinc oxide whiskers in air without crystallization chambers or reactors, using CO_2-laser radiation. The features of their exciton luminescence are studied, and they are compared with bulk single crystals and epitaxial layers of ZnO. © *1997 American Institute of Physics.* [S1063-7850(97)01111-7]

Interest in crystal whiskers arises from a number of unusual properties that they have, in particular mechanical strength close to the theoretical limit and from the possibility of obtaining submicron structures and in general of studying the growth mechanisms and kinetics of the crystal in the one-dimensional approximation.[1] It is well known that zinc oxide has a tendency to form an acicular habit of single-crystal whiskers extended along the *C* axis and, depending on the process parameters, attaining a length of from several microns to several centimeters (see, for example, Refs. 2 and 3). It is also well known that the use of laser radiation makes it possible to grow single crystals by a crucible-free method in an arbitrary atmosphere, including vacuum.[4,5] Moreover, the simplicity of the method, the low thermal lag, and the free access for observing the crystallization front broaden the experimental possibilities for studying the crystallization processes, including those affected by external fields.

In this paper, we describe the first experiments on the production of zinc oxide whiskers in air—without crystallization chambers or reactors—using laser radiation. There is also interest in studying the features of the exciton luminescence of filamentary microcrystals and in comparing them with bulk single crystals and epitaxial layers of zinc oxide.

A commercial LG-25 cw CO_2 laser with a power of 25 W was used in the experiments. When a Ge lens with $f=20$ cm was used for focusing, the power density on the surface of a pellet reached 10^5 W/cm^2. Pellets prepressed from VHP powdered zinc oxide, about 1 cm in diameter and height, were annealed in a muffle furnace at a temperature of 800 °C for 1 h to ensure mechanical strength. The irradiation procedure took 1–3 min. After a short time (about 10 sec) in the local irradiation region, the temperature reaches the value (direct measurements are made difficult both by the size of the samples and by the substantial temperature gradient) necessary to decompose the zinc oxide: $T_{\text{dec}} \geqslant 1800°$. The beginning of the decomposition of the material in the region of the focus and homogeneous formation of ZnO at a distance of 1 cm from the focal region could be seen with the naked eye from a jet of white smoke directed straight upwards. A pure finely dispersed powder of zinc oxide with a grain size no greater than 10 nm was condensed on a cold glass substrate placed in the jet of smoke at a distance of 1–3 cm from the focal point, whereas the initial powder possessed a grain size of 1 μm. A liquid phase ($T_m \geqslant 1950$ °C) apparently forms after a certain time needed to reach T_m, taking into account all thermal losses and the deepening of the crater, which slows them down.

Reference 6 pointed out that the liquid can be swept out of a shallow crater by the recoil force of the vapors if they act for a long enough time and if the irradiation zone is small, which corresponds to our case. When the edge of the crater is formed, sweeping out of the liquid, along with removal of matter in the gas phase, can play an appreciable role if the radiation intensity does not exceed the threshold of developed vaporization. The possibility of melting under the conditions of the experiment, at least inside the crater, is indicated by vitrification of the inner surfaces of the crater and of the opening observed under a microscope after cracking open the pellet. We were especially interested in this question, since, because the decomposition and melting temperatures of zinc oxide are very different, it is considered problematical to melt it under ordinary conditions. At the same time, the presence of at least a quasi-liquid phase, close to the state of a dense gas and containing relatively active growth sections, is essential in the PZhK growth model of whiskers.[1]

The size of the crater in the irradiation region reached 3–4 mm, depending on the time and the initial power density. Bumps or thickenings visible to the naked eye are formed on the edges of the crater. When they are examined under a microscope with moderate magnification (10–100), it is clear that the edge of the crater consists of discrete oval formations about 1 mm across, separated from each other by the same distance. A fragment of the crater's edge is shown in Fig. 1. It can be seen that whiskers grow in radial directions on each such formation, excluding their inner conical surface, close to the irradiation zone. The size of these crystals reached several millimeters along the *C* axis, and several microns in directions perpendicular to the *C* axis. X-ray structural measurements were made difficult by the size of the samples.

The length of the acicular crystals made it possible to excite photoluminescence by submerging a pellet with crystals directly into liquid nitrogen. To monitor it, in order to avoid recording the radiation of the pellet itself, the exciton luminescence of individual whiskers pressed between two transparent sapphire substrates was also studied. The exciton luminescence was excited by the 313-nm line of a mercury lamp and a N_2 laser. The spectra were recorded using synchronous detection and an SPM-2 monochromator with a photomultiplier.

FIG. 1. Microphotograph of a fragment of the edge of a crater, illustrating the radial growth direction of zinc oxide whiskers.

A characteristic exciton luminescence spectrum of zinc oxide whiskers, obtained at 77 K, is shown in Fig. 2, curve *1*. For comparison, the same figure shows the exciton luminescence spectra of texturized layers and of single crystals and epitaxial layers of ZnO (curves *2* and *3*, respectively). It can be seen that the fundamental bands of the epitaxial layers, observed in the whiskers, are close to 369.3, 374.3, and 382.6 nm. At the same time, the radiation of the 367.2-nm peak, corresponding to the annihilation of a free Al exciton (see, for example, Ref. 7) and a series of subsequent equidistant bands—the phonon sidebands of Al—predominate in the spectra of single crystals and of perfect epitaxial layers of zinc oxide.

The band with λ_{max} at 369.3 nm was identified earlier as the radiation of an exciton associated with the neutral donor J_D.[8] The exciton luminescence of the whiskers has the features that the radiation from the free Al exciton is absent, the radiation in the band of J_D is relatively weak, and the intensity of the 1LO band is anomalously high. Since bulk single crystals and high-quality epitaxial layers are dominated by the radiation in the Al band and have the smallest 1LO/2LO intensity ratio,[7] the features of whiskers pointed out above, as well as the broadening of the phonon sidebands, are in our opinion evidence that they have a significant number of defects.

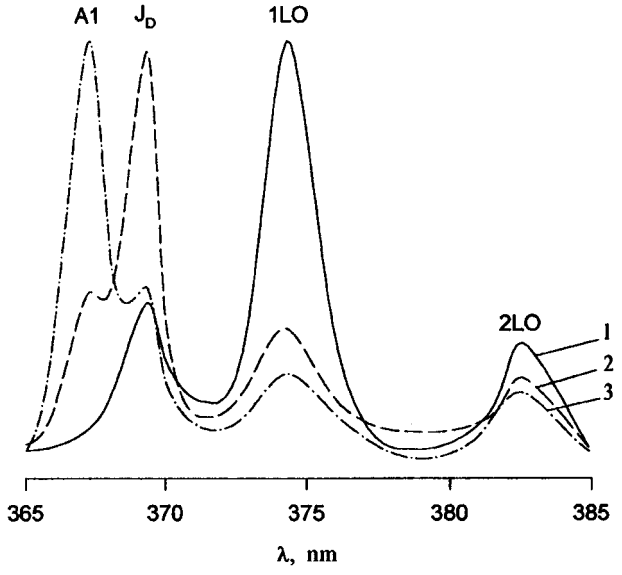

FIG. 2. Exciton luminescence spectra of whiskers (*1*), texturized films (*2*), single crystals, and epitaxial layers (*3*) of zinc oxide at 77 K.

Reference 1 explains the high mechanical strength of whiskers relative to bulk single crystals in terms of their high structural perfection (for thicknesses less than 1 μm), associated with a decreased probability that the crystallization front will capture liquid inclusions, which cause the growth of dislocations during solidification. This is apparently valid for whiskers obtained under special conditions (closer to steady state). In our case, with temperature gradients exceeding 10^3 K/cm, it is obvious that there are substantial mechanical stresses that are associated with the presence of defects and, as a consequence, with the observed features of the exciton luminescence of zinc oxide whiskers.

The authors are grateful to A. Kh. Abdulev for help in carrying out the experiment.

This work was carried out with the financial support of the Russian Fund for Fundamental Research, Grant 02-4554.

[1] E. I. Givargizov, *Growth of Crystal Whiskers and Lamellae from Vapor* (Nauka, Moscow, 1977).
[2] Y. S. Park and D. C. Reynolds, J. Appl. Phys. **38**, 756 (1967).
[3] M. Ishii and H. Hashimoto, Jpn. J. Appl. Phys. **8**, 1107 (1969).
[4] J. F. Ready, *Effects of High-Power Laser Radiation* (Academic Press, Orlando, Fla., 1971; Mir, Moscow, 1974).
[5] V. V. Ryabchenkov, ''Synthesis of refractory single crystals heated by laser,'' Author's abstract of dissertation for candidate degree, IKAN, Moscow, 1987.
[6] V. B. Fedorov, ''Quasi-steady-state optical discharges on solid targets,'' Tr. IOFAN **10**, 75 (1988).
[7] A. Kh. Abduev, A. D. Adukov, B. M. Ataev *et al.*, Opt. Spektrosk. **50** , 1137 (1981) [Opt. Spectrosc. (USSR) **50**, 626 (1981)].
[8] T. V. Butkhuzi, A. N. Georgobiani, E. Zada-Uly *et al.*, ''UV luminescence of single-crystal layers of zinc oxide obtained by a quasi-epitaxial method,'' Tr. Fiz. Inst. Akad. Nauk SSSR 182. 140, 164 (1987).

Translated by W. J. Manthey
Edited by David L. Book

The degree of relative ordering accompanying a nonequilibrium phase transition in a system consisting of a thin film of high-temperature current-carrying superconductor and boiling coolant

V. N. Skokov

Thermal Physics Institute, Ural Branch, Russian Academy of Sciences, Ekaterinburg
(Submitted June 9, 1997)
Pis'ma Zh. Tekh. Fiz. **23**, 64–68 (November 12, 1997)

From experimental implementations of thermal oscillations in the region of a nonequilibrium phase transition accompanying the Joule self-heating of thin films of high-temperature superconductors in boiling nitrogen, an estimate is made of the relative ordering of the system, using the *S*-theorem criterion. It is shown that, according to this criterion, the two-phase state of the system is more ordered than the homogeneous single-phase state. © *1997 American Institute of Physics.* [S1063-7850(97)01211-1]

Self-organization processes accompanying nonequilibrium phase transitions have attracted the attention of investigators for many years. The criteria for self-organization in this case remain an issue of high priority. Yu. L. Klimontovich formulated a criterion for the relative degree of ordering of open systems, based on the *S* theorem (see, for example, Refs. 1–4). In particular, it was concluded in Ref. 4 that, for type-II phase transitions, the subcritical state ($T<T_c$) is more ordered than the supercritical state ($T>T_c$). It is a difficult task to directly determine the degree of ordering from the experimental data for ordinary thermodynamic phase transitions, since, to do this, the distribution function of the thermal fluctuations must be measured close to the critical point. In the present paper we compare the relative degree of ordering according to the experimental data for a critical nonequilibrium phase transition in the complex nonlinear system consisting of a superconductor with a current and a boiling coolant.

It was experimentally shown in Refs. 5–8 that, when thin films of high-temperature superconductors undergo Joule heating in liquid nitrogen, a critical nonequilibrium phase transition associated with the interaction of nonlinear thermal processes occurs in the current-carrying superconductor and the boiling coolant. The amplitude of the temperature oscillations sharply increases in the transition region in this case, and macroscopic wide-band $1/f$ noise is observed.[8] It is possible to bring about subcritical, critical, and supercritical nonequilibrium phase transitions by varying the parameters of the electric circuit.

Oscilloscope tracings of the voltage drop on the potential contacts of a thin-film $YBa_2Cu_3O_{7-x}$ bridge were measured in the experiments under conditions of Joule self-heating by a transport current in boiling nitrogen. The oscillations of the voltage drop are associated with the oscillations of the heat output as the nitrogen boils on the surface of the superconductor. In this case there is feedback in the system between the processes of boiling and of the dynamics of the normal-phase domain in the superconductor.

Anomalies in the behavior of the system were observed during strong heating, corresponding to a local crisis of thermal evolution.[7] These features can be regarded as a nonequilibrium phase transition. Different regimes can be implemented by varying the slope of the load line of the electric circuit with respect to the current–voltage characteristic, which has a characteristic S shape.[5–8] If the load line has one intersection with the current–voltage characteristic, a supercritical transition is observed. When there are two intersection points, a type-I nonequilibrium phase transition or a subcritical transition occurs. Finally, when the load line is tangent to the current–voltage characteristic, a critical transition occurs.

Figure 1 shows typical distribution functions of the amplitudes of oscillations in the supercritical (a) and subcritical (b) regimes. In going from the supercritical to the subcritical region (by varying the slope of the load line with respect to the current–voltage characteristic), the amplitude of the oscillations increased according to the power law $A\sim R^{1/2}$, where A is the half-width of the distribution function, and R is the load resistance of the electric circuit. Such an increase occurs until the system splits up into phases (Fig. 1b).

To compare the degree of ordering in the supercritical and subcritical regimes, we used the criterion of the *S* theorem, the essence of which is to compare states with different values of a control parameter, reduced to the same mean effective energy of the system.[1–4] The load resistance of the electric circuit can be used as the control parameter. Let us consider the states for two values of the control parameter, R_0 and R_1. These states correspond to the voltage drop at the potential contacts at two times, and accordingly to two distribution functions, f_0 and f_1. We take the state with $R=R_0$ for the state of physical chaos and, following Refs. 2 and 3, we introduce the effective function

$$H_{\text{eff}}=-\ln f_0, \quad \int f_0(x)dx=1. \tag{1}$$

Because of the openness of the system, the effective Hamiltonian is not in general conserved as the control parameter varies. To compare the two states, we introduce the renormalized value $\tilde{f}_0$ in order to satisfy the condition of equality of the mean effective energy in the two states, i.e.,

$$\int H_{\text{eff}}\tilde{f}_0 dx=\int H_{\text{eff}}\, f_1 dx. \tag{2}$$

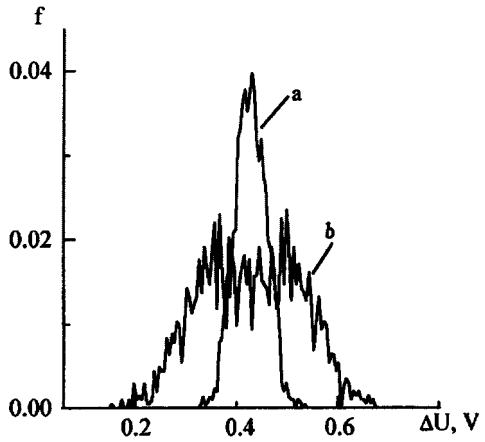

FIG. 1. Distribution functions of the oscillation amplitudes of the voltage drop on a sample in the supercritical (a) and subcritical (b) regimes.

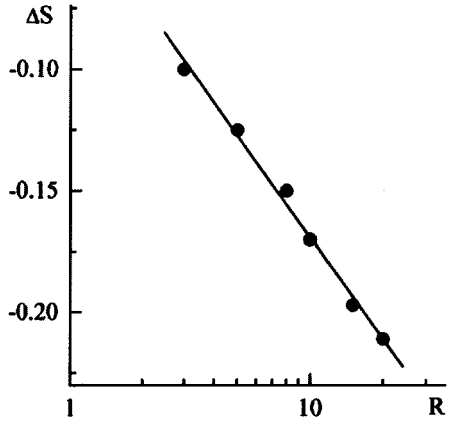

FIG. 2. Entropy change in going from the supercritical to the subcritical region as a function of the control parameter.

The renormalized function $\tilde{f}_0$, according to Refs. 1–4, is represented in canonical form:

$$\tilde{f}_0 = \exp \frac{\tilde{F} - H_{\text{eff}}}{\tilde{T}}, \quad \int \tilde{f}_0 dx = 1, \tag{3}$$

where $\tilde{F}$ and $\tilde{T}$ are the effective free energy and the effective temperature in the renormalized state. Equations (1) and (3) make it possible to determine the effective temperature $\tilde{T}$ from the experimentally known functions f_0 and f_1. The criterion of the S theorem states that, for $\tilde{T} > 1$, the assumption that the chosen reference state 0 is highly random holds. The entropy change

$$\Delta S = S_1 - \tilde{S}_0 = -\int f_1 \ln \frac{f_1}{f_0} dx < 0 \tag{4}$$

serves as the measure of the randomness of state 0 (or of the self-organization of state 1).

The supercritical state (Fig. 1a) with $R = R_0$ was chosen as the reference state in calculating the measure of the relative ordering. States with $R > R_0$ were compared with the reference state. It was found by numerically solving Eqs. (1)–(3) using the experimental realizations that, in states with $R > R_0$, the corresponding effective temperatures were $\tilde{T}_{\text{eff}}(R) > 1$; i.e., according to the criterion of the S theorem, self-organization of the system occurs as one goes from the supercritical to the subcritical region. When the reference state was inverted, i.e., when state 1 ($R < R_0$) was chosen as the state of physical chaos, values $\tilde{T}_{\text{eff}} < 1$ were obtained. This is evidence that it is correct to choose the state with the smallest R as the state of physical chaos. Equation (4) was used to calculate the entropy change ΔS for a given mean effective energy of the system as a function of the control parameter R. The $\Delta S(R)$ dependence is given in Fig. 2 (the scale of the horizontal axis in Fig. 2 is logarithmic). It can be seen from the figure that the results are a good approximation of the $\Delta S \sim -\ln R$ dependence (the solid line in Fig. 2).

The application of the Klimontovich S theorem to a nonequilibrium phase transition in a system consisting of a current-carrying superconductor and a boiling coolant thus shows that, as one goes from the supercritical (single-phase) to the subcritical (two-phase) state, the entropy of the system, calculated from the experimental data under the condition that the mean effective energy is constant, decreases; i.e., self-organization occurs in the system.

This work was carried out with the support of the Russian Fund for Fundamental Research (Project No. 96-02-16077a).

[1] Yu. L. Klimontovich, Pis'ma Zh. Tekh. Fiz. **9**, 1412 (1983) [Sov. Tech. Phys. Lett. **9**, 606 (1983)].
[2] Yu. L. Klimontovich, Pis'ma Zh. Tekh. Fiz. **14**, 2226 (1988) [Sov. Tech. Phys. Lett. **14**, 966 (1988)].
[3] Yu. L. Klimontovich, *Statistical Theory of Open Systems* (Kluwer Academic, Boston, 1995).
[4] Yu. L. Klimontovich, Phys. Lett. A **210**, 65 (1996).
[5] V. N. Skokov and V. P. Koverda, Cryogenics **33**, 1072 (1993).
[6] V. N. Skokov, V. P. Koverda, and I. B. Ivakin, Pis'ma Zh. Tekh. Fiz. **18**, No. 3, 59 (1992) [Sov. Tech. Phys. Lett. **18**, 82 (1992)] .
[7] V. N. Skokov, V. P. Koverda, V. P. Skripov, I. B. Ivakin, and N. M. Semenova, Teplofiz. Vys. Temp. **34**, 802 (1996).
[8] V. P. Koverda, V. N. Skokov, and V. P. Skripov, JETP Lett. **63**, 775 (1996).

Translated by W. J. Manthey
Edited by David L. Book

Formation of an ''inverse'' kink in optically bistable systems based on increasing absorption

O. A. Gunaze and V. A. Trofimov

M. V. Lomonosov State University, Moscow
(Submitted March 21, 1997)
Pis'ma Zh. Tekh. Fiz. **23**, 69–73 (November 12, 1997)

Using the well-known property of the focusing of hollow beams, it is shown that a high-absorption domain can be created in the end of a sample cell. The results can serve as one method of recording information in the interior of a medium. The implementation of such a domain can serve as a new mechanism for developing autowave processes for varying the output intensity of a light beam. © *1997 American Institute of Physics.* [S1063-7850(97)01311-6]

Optical bistability based on increasing absorption has been studied in the literature for a long time. This is apparently because it is relatively simple to implement in physical experiments and because it has been observed in a wide variety of nonlinear media (for example, semiconductors, chemically active gas mixtures, and various glasses).[1] Interest in the problem of optical bistability is also caused by the prospect of constructing new optical information-processing methods and optical computers.[1]

Among the different phenomena that accompany optical bistability based on increasing absorption, we note in particular the formation of longitudinal kinks observed in semiconductors.[2,3] Similar spatial structures in a chemically active gas mixture in which light energy is absorbed by a reaction product were also obtained in Ref. 4. It is important to emphasize that the region in which the characteristic of the medium had a high value was close to its input cross section when collimated light beams acted on it. However, temperature kinks, for example, can be formed close to the output cross section of a semiconductor by focusing optical radiation on the back face of the crystal.[5–7] Note that an initially Gaussian beam was used for this purpose in the indicated papers.

This paper, taking into account the diffraction of optical radiation and using optical bistability based on a chemically active gas mixture as an example, shows that, when an initially hollow collimated light beam acts on it, an ''inverse'' kink of the concentration of the reaction product is formed. The word *inverse* emphasizes that it is formed at the back wall of the sample cell: a region of high concentration of the product is located close to the output cross section of the medium and is preceded by a region in which its concentration is low. This paper also discusses the mechanism by which pulsations of the high-absorption domain and of transmitted optical radiation intensity are developed, based on the mechanism described here by which kinks are formed under the action of collimated hollow beams.

Note that the necessity of taking into account the diffraction and self-action of optical radiation when it propagates in an optically bistable cavityless system manifests itself in other ways besides the decrease in the initial beam radius, since its diffraction length shortens in the process of the interaction both because its transverse size is reduced as a consequence of the absorption of light energy and because it breaks up into parts because its energy is consumed in the region where the intensity is highest. The influence of diffraction can therefore be substantial, even if the diffraction length is initially several times as great as the length of the nonlinear medium.

The propagation of the axisymmetric collimated hollow beam that we studied is described by the following system of dimensionless equations:

$$\frac{\partial A}{\partial z}+iD\Delta_{\perp}A+\delta_0 NA=0,\quad 0<z<1,\quad 0<r<R,$$

$$\varepsilon\frac{\partial T}{\partial t}=\chi\Delta_{\perp}T+qN|A|^2+\gamma f,\quad \Delta_{\perp}=\frac{1}{r}\frac{\partial}{\partial r}\left(r\frac{\partial}{\partial r}\right),\quad t>0,\tag{1}$$

$$\frac{\partial N}{\partial t}=D_N\Delta_{\perp}N+f,\quad f=(1-N)\exp\left(-\frac{1}{T}\right)-kN\exp\left(-\frac{T_c}{T}\right)$$

with initial and boundary conditions

$$A_{z=0}=A_0(r)[1-\exp(-10t)],\quad A_0(r)=\frac{r^2}{a^2}\exp\left(-\frac{r^2}{a^2}\right),\tag{2}$$

$$A|_{r=R}=\left.\frac{\partial A}{\partial r}\right|_{r=0}=\left.\frac{\partial N}{\partial r}\right|_{r=0,R}=\left.\frac{\partial T}{\partial r}\right|_{r=0}=0,$$

$$\chi\left.\frac{\partial T}{\partial r}\right|_{r=R}=-\eta(T-T_0),\quad T|_{t=0}=T_0,\quad f|_{t=0}=0.$$

The description of the parameters of Eqs. (1) and (2) is given in detail in Ref. 8. Therefore we only point out here that A is the normalized complex amplitude of the beam, N is the dimensionless concentration of the reaction product, T is the normalized temperature of the medium, z is the longitudinal coordinate normalized to the diffraction length, q characterizes the input power of the beam, and a is the normalized initial radius of the beam, retained, as is D, for convenience in carrying out the calculations.

Let us consider the interaction of optical radiation under the conditions of weak diffusion and thermal conductivity of a medium with the following parameters:

$$R=1,\quad \eta=2\chi,\quad D=0.0025,\quad \varepsilon=1,$$

$$D_N=\chi=10^{-7},\quad T_c=0.375,$$

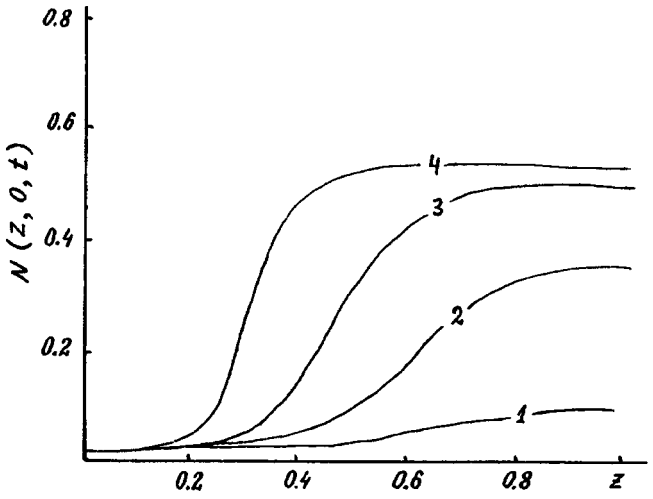

FIG. 1. Longitudinal distribution of the concentration of the reaction product on the axis of the beam at time $t=35$ (*1*), 55 (*2*), 80 (*3*), 150 (*4*) for $\delta_0=4$, $\gamma=0$, $q=0.5$, $a=0.1$, $D=0.0025$, and $D_N=\xi=10^{-7}$.

$$T_0=0.125, \quad a=0.1, \quad k=0.5, \quad \gamma=0,$$
$$q=0.5, \quad \delta_0=4. \tag{3}$$

We can make several remarks regarding the values of the parameters in Eq. (3). First, the concentration and temperature have a bistable dependence on the input intensity of the optical radiation for these values. The regularities of the implementation of the optical bistability for q, χ, D_N, are D values larger than those in Eqs. (3) were studied in Ref.9, where it was shown that it is possible to form multidomain structures. Second, the value of the initial power q is such that no high-concentration region is formed close to the input cross section of the sample cell.

As is well known, a hollow beam is transformed into a Gaussian beam at a definite distance (depending on the position of its maximum and the size of the region with nonzero intensity). When this happens, its maximum intensity can exceed its input value. By using this property of a hollow beam, it is easy to make it intense enough to switch a chemical-medium–laser-beam system to the upper state close to the output face of the cell; this also causes a high-concentration region (an inverse kink) to be formed here. The time during which it exists and its longitudinal size depend on many parameters, in particular the diffusion, thermal conduction, and absorption coefficients. As an illustration, Fig. 1 shows the dynamics of the formation of an inverse kink on the beam axis. As can be seen from the figure, a kink is generated at the end of the sample cell. This is because the diffracted hollow beam is focused on the output face of the cell. A kink is then formed within a certain region of the medium. The boundary of this region is determined by the diffusion, the thermal conductivity, and the inverse reaction rate. In particular, a situation is possible in which the switching wave comes to a halt. It is this case that is shown in Fig. 1. We should emphasize that the diffusion and thermal conductivity coefficients must be small for this case to occur.

If the processes of longitudinal and transverse diffusion or thermal conductivity are sufficiently well developed, the region of high concentration or temperature reaches the input cross section within a certain time. As a result, the absorption coefficient increases here, the intensity decreases at the end of the sample cell, and the kink disappears. Since the intensity close to the input cross section is insufficient to keep the system in the upper bistable state, in the absence of an inflow of the reaction product or of heat, the absorption coefficient close to the input cross section decreases. Because of this, the intensity increases at the end of the sample cell, which again causes a kink to form there. This process is then repeated. The output intensity of the beam and the power transmitted through the cell will consequently oscillate. We should point out that the mechanism of these processes was predicted in Ref. 10. Thus, the mechanism of oscillations of the output intensity explained here is similar to that described in Ref. 5 and to the output-power mechanism when optical radiation is focused on the back face of a semiconductor, experimentally implemented in Refs. 6 and 7.

This work was carried out with the support of the Russian Fund for Fundamental Research (Grant No. 95-02-04448).

[1] H. M. Gibbs, *Optical Bistability: Controlling Light with Light* (Academic Press, Orlando, Fla., 1985; Moscow, 1988).
[2] H. M. Gibbs *et al.*, Phys. Rev. A **32**, 692 (1985).
[3] M. Lindberg, S. W. Koch, and H. Haug, Phys. Rev. A **33**, 407 (1986).
[4] M. I. Kalinichenko, and V. A. Trofimov, Opt. Spektrosk. **61**, 182 (1986) [Opt. Spectrosc. (USSR) **61**, 117 (1986)].
[5] N. N. Rozanov, A. V. Fedorov, and G. V. Khodova, Phys. Status Solidi B **150**, 545 (1988).
[6] S. E. Esipov and V. A. Stadnic, Phys. Status Solidi B **150**, 501 (1988).
[7] V. A. Stadnik, Fiz. Tverd. Tela (Leningrad) **30**, 3571 (1988) [Sov. Phys. Solid State **30**, 2052 (1988)].
[8] O. A. Gunaze and V. A. Trofimov, Izv. Ross. Akad. Nauk Ser. Fiz. **60**, No. 6, 65 (1996).
[9] O. A. Gunaze and V. A. Trofimov, Pis'ma Zh. Tekh. Fiz. **22**, No. 16, 1 (1996) [Tech. Phys. Lett. **22**, 642 (1996)].
[10] O. A. Gunaze, and V. A. Trofimov, Bull. Roy. Astron. Soc. Physics Supplement, Physics of Vibrations **57**, 193 (1993).

Translated by W. J. Manthey
Edited by David L. Book

Angular momentum of the fields of a few-mode fiber: I. A perturbed optical vortex

A. V. Volyar and T. A. Fadeeva

Simferopol State University
(Submitted March 25, 1997)
Pis'ma Zh. Tekh. Fiz. **23**, 74–81 (November 12, 1997)

This paper presents the results of studies of the physical nature of the electrodynamic angular momentum of a stable CV_{+1}^{+} vortex in a few-mode fiber. It shows that the angular momentum of a CV_{+1}^{+} vortex can be conventionally divided into orbital and spin angular momenta. The longitudinal component of the fundamental HE_{11}^{+} mode on the axis of the fiber has a pure screw dislocation with a topological charge of $e=+1$. The longitudinal component of a CV_{+1}^{+} vortex also has a pure screw dislocation on the axis of the fiber with a topological charge of $e=+2$. Therefore, perturbation of a CV_{+1}^{+} vortex by the field of the fundamental HE_{11}^{+} mode removes the degeneracy of the pure screw dislocations of the longitudinal and transverse components of the field and breaks down the structural stability of the CV_{+1}^{+} vortex. As a result, an additional azimuthal flux of energy with an angular momentum opposite to that of the fundamental flux is induced. An analogy is drawn between the stream lines of a perturbed CV vortex and the stream lines of an inviscid liquid flowing around a rotating cylinder. Studies of the evolution of a CV vortex in a parabolic fiber show that they are structurally stable when acted on by the perturbing field of the HE_{11}^{+} mode. However, perturbing a CV_{+1}^{+} vortex of a stepped fiber with the field of the HE_{11}^{+} mode destroys the structural stability of the vortex. It is found that the propagation of a circularly polarized CV vortex can be represented as a helical wavefront screwing into the medium of the fiber. The propagation of a linearly polarized vortex in free space is characterized by the translational displacement (without rotation) of a helical wavefront.
[S1063-7850(97)01411-0]

The physical nature of optical vortices in few-mode fibers is inextricably associated with the azimuthal energy fluxes of these fields and consequently with the angular momentum of the wave field. In its general features, the problem of the angular momentum **M** of an electromagnetic field on a quantum level has been touched on in Refs. 1 and 2. However, interest in this phenomenon has increased only in recent years in connection with the study of the properties of optical vortices in free space[3] in order to use them as optical traps of microparticles and optical tweezers.[4]

In our opinion, the problem of transporting angular momentum in optical fibers has two aspects: (1) the electrodynamic task of shaping and converting the angular momentum of the light waves in a fiber, and (2) the quantum-mechanical task of transforming the angular momentum of directed fields in a fiber into the mechanical angular momentum of microparticles.[5]

In this paper, we consider only the first part of this problem: the properties of the angular momentum of the field of a stable CV vortex in a few-mode fiber when it is perturbed by the circularly polarized field of the HE_{11} mode.

1. When a stable CV_{+1}^{+} vortex is excited in a few-mode fiber,[6] the right-circularly polarized HE_{11}^{+} mode is usually excited at the same time. The field of this mode perturbs the field of the vortex and alters the location of the pure screw dislocations. Unlike fields in free space, the CV vortex and the HE_{11} mode contain longitudinal components of the electric field $\mathbf{E}_z$ and the magnetic field $\mathbf{H}_z$. Moreover, the $\mathbf{E}_z$ and $\mathbf{H}_z$ components of these fields on the fiber axis ($R=0$) have pure screw dislocations. Therefore, the process of perturbing the CV vortex by the HE_{11} mode reduces to studying the interaction of the singularities of the transverse and longitudinal fields. Let a CV_{+1}^{+} vortex with a topological charge $e=1$ and the HE_{11}^{+} mode, both right-circularly polarized, be excited in an optical fiber. Expressions for the electric field **e** can be written as[7,8]

$$\mathbf{e}=\mathbf{e}_t(CV_{+1}^{+})+a\mathbf{e}_z(HE_{11}^{+}):$$

$$\mathbf{e}_t=\hat{\mathbf{e}}^{+}(F_1(R)\exp\{i(\phi+\beta_1^1 z)\}+aE_0(R)\exp\{i\beta_0 z\}), \tag{1}$$

$$\mathbf{e}_z=i\frac{\sqrt{2\Delta}}{V}(G_1^{-}(R)\exp\{i(2\phi+\beta_1^1 z)\}$$
$$+aG_0(R)\exp\{i(\phi+\beta_0 z)\}), \tag{2}$$

where a is the relative weight of the HE_{11} mode, $\hat{\mathbf{e}}^{+}$ is the unit vector of the right-circular polarization, $F_1(R)$ and $F_0(R)$ are radial functions of the transverse fields,[7] and β_1^1 and β_0 are the propagation constants of the CV_{+1}^{+} and HE_{11}^{+} fields, respectively.

It follows from Eq. (2) that the $\mathbf{e}_z$ component of the CV_{+1}^{+} vortex transports a topological charge of $e=+2$, while that of the HE_{11}^{+} mode transports the topological charge $e=+1$. The positions of the zeroes of the $\mathbf{e}_t$ and $\mathbf{e}_z$ fields can be determined from the conditions[9] $\mathrm{Re}(\mathbf{e})=\mathrm{Im}(\mathbf{e})=0$. For the fields of Eqs. (1) and (2), the azimuthal coordinates of the position of the pure screw dislocations of the $\mathbf{e}_t$ and $\mathbf{e}_z$ fields are identical and equal

$$\phi=\pi+(\beta_0-\beta_1)z. \tag{3}$$

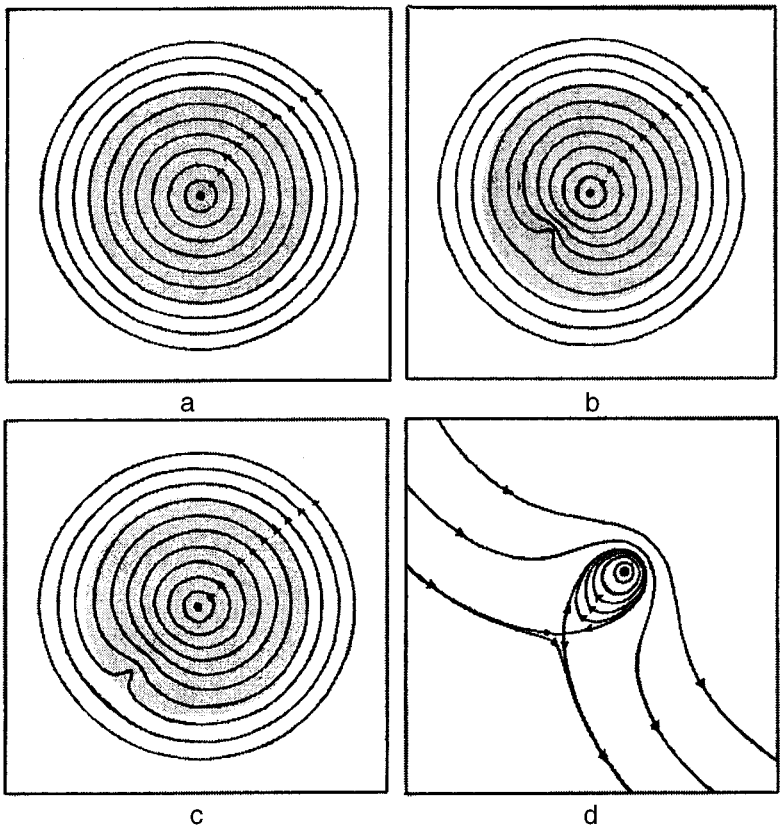

FIG. 1. Current lines of the Poynting vector $\mathbf{P}_t$ in the cross section of a fiber $\delta\beta_{21}z=\pi/4$: (a) $a=0$, (b) $a=0.5$, (c) $a=0.7$, (d) shows the neighborhood of the induced vortex, $a=0.5$. The shading denotes the fiber core.

The radial coordinates of these dislocations are different and are the solutions of the equations

$$F_1(R)-aF_0(R)=0, \tag{4}$$

$$G_1^-(R)-aG_0(R)=0. \tag{5}$$

It follows from Eqs. (3)–(5) that the field dislocations lie on circles with radii $R_0=0$, R_1, and R_2 and rotate with velocity $w=d\phi/dz=\beta_0-\beta_1$. For a stepped fiber with a core radius of $\rho_0=3.5\ \mu$m and a waveguide parameter of $V=3.6$, the velocity of the dislocations is $w=1.38\times10^4\ \mathrm{m}^{-1}$. Only the dislocation $\mathbf{e}_t$ of the field component with the coordinate $R=R_1$ is recorded in a direct physical experiment, since the observed value is $P_z=\mathrm{Re}(e_xh_y-e_yh_x)$, which is a component of the Poynting vector. We shall analyze a method of measuring the dislocation $\mathbf{e}_z$ of the component separately.

2. Let us consider the evolution of the angular momentum $\mathbf{M}$ of a perturbed CV_{+1}^{+} vortex. The electrodynamic angular momentum $\mathbf{M}$ can be defined by[1]

$$\mathbf{M}=\mathbf{r}\times\mathbf{P}, \tag{6}$$

where

$$\mathbf{P}=\varepsilon_0\mu_0(\mathbf{e}\times\mathbf{h}^*+\mathbf{e}^*\times\mathbf{h})/2 \tag{7}$$

is the Poynting vector. Based on Ref. 7, we write the components of the magnetic field $\mathbf{h}$ of the CV_{+1}^{+} vortex and the HE_{11}^{+} mode in the form

$$\mathbf{h}=-in_{co}(\varepsilon_0/\mu_0)^{1/2}\mathbf{e}. \tag{8}$$

Then, substituting the fields of Eqs. (1), (2), and (8) into Eq. (7), we find the components of the energy flux of a perturbed CV_{+1}^{+} vortex in a few-mode fiber:

$$P_\phi=-2K\{F_1G_1^-+a^2F_0G_0+a(F_0G_1^-+F_1G_0)\times\cos(\phi-wz)\}, \tag{9}$$

$$P_r=2Ka(F_0G_1^-F_1G_0)\sin(\phi-wz), \tag{10}$$

$$K=1/(2c^2)n_{co}(\varepsilon_0/\mu_0)^{1/2}(\sqrt{2\Delta}V). \tag{11}$$

It is easy to determine the z component of angular momentum $\mathbf{M}$ from Eq. (9) as

$$\mathbf{M}_z=\rho\mathbf{P}_\psi, \tag{12}$$

where ρ is the running radius of the cross section of the fiber. We determine the stream lines of the vector field $\mathbf{P}$ in a fiber from[10]

$$\frac{dx}{P_x}=\frac{dy}{P_y},\quad \frac{dy}{P_y}=\frac{dz}{P_z}, \tag{13}$$

The singular points of the stream line pattern in a cross section of the fiber are found from

$$\mathbf{P}_\phi=\mathbf{P}_r=0, \tag{14}$$

from which it follows that

$$(F_1-aF_0)(G_1^-aG_0)=0. \tag{15}$$

Equation (15) shows that there will be three such singularities: for $R=R_1$, the position of the dislocation of the $\mathbf{e}_t$ component, and, for $R=0$ and $R=R_2$, the positions of the dislocations of the $\mathbf{e}_z$ component, while Eq. (15) is a combination of Eqs. (4) and (5). The point $R=0$ corresponds to the center of the main azimuthal flux; the point $R=R_1$ is a singular point of the saddle type, at which the branches of the

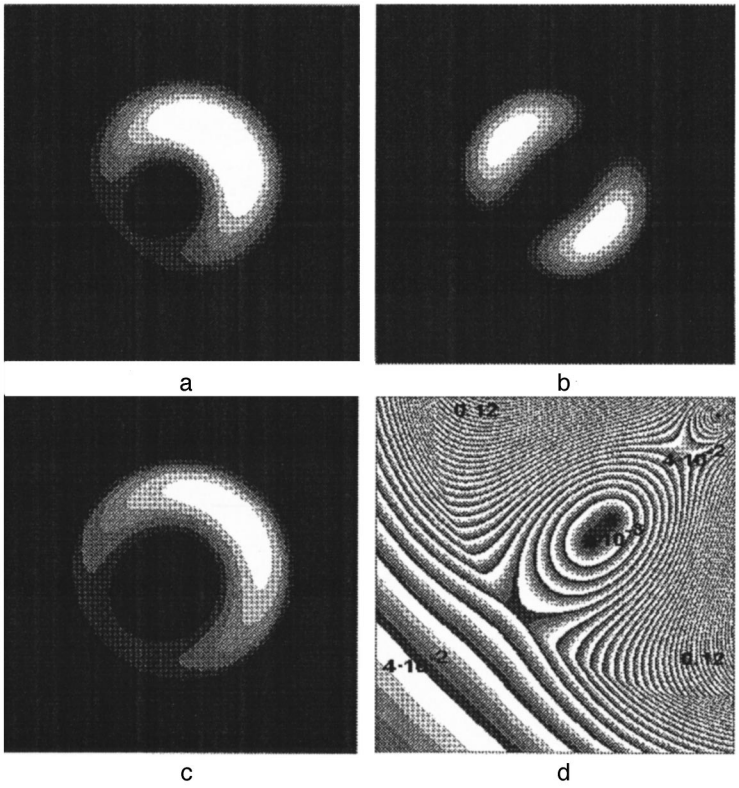

FIG. 2. Distribution in the cross section of a fiber $\delta\beta_{21}z=\pi/4$ of: (a) $\mathbf{P}_z$, (b) $\mathbf{P}_r$, (c) $\mathbf{P}_\phi$, (d) shows the lines of the absolute value of the transverse flux $\mathbf{P}_t$ in the neighborhood of an induced vortex (the normalized value $P_t/P_{t_{(\max)}}$ is shown).

separatrix intersect and at which a pure screw dislocation $\mathbf{e}_i$ of the field component is located. The center of the induced vortex is placed at the point $R=R_2$. Since, in the absence of perturbation ($a=0$), the singular points of the field are degenerate at a point of the type of the center point, whereas three singular points are generated when a perturbation acts ($a\neq 0$), the CV_{+1}^{+} vortex is structurally unstable[11] with respect to the action of a perturbation of a right-circularly polarized HE_{11}^{+} mode. For the stepped fiber whose parameters are given above, a diagram of the lines of force of the transverse Poynting vector $\mathbf{P}_t$ is shown in Fig. 1 for certain values of perturbation parameter a. For a CV vortex in a parabolic fiber, $\mathbf{P}_r=0$ holds in the entire region of the cross section, and $R_1=R_2$. In this case, the stream lines of P_t form concentric rings centered at $R=0$, coinciding with the diagram of stream lines with no perturbation (Fig. 1a). A CV_{+1}^{+} vortex in a parabolic fiber is therefore structurally stable with respect to perturbation by the HE_{11}^{+} mode. In a stepped fiber, as the perturbation parameter a increases, the region of localization of induced azimuthal flux of opposite sign (Figs. 1b and 1c) increases. We should especially note that the stream lines of an induced vortex are analogous in their formal attributes to the stream lines that appear when an inviscid liquid flows around a rotating cylinder.[12]

Figure 2 shows diagrams of the energy distribution in $\mathbf{P}_z$, $\mathbf{P}_\phi$, and $\mathbf{P}_r$ of the fluxes for a stepped fiber with the corresponding values of the perturbation parameter a.

A numerical calculation shows that the ratio of the absolute values of the total flux is $\alpha=|\mathbf{P}_t|/|\mathbf{P}_z|=4.32\times 10^{-2}$ for a stepped fiber and $\alpha=4.88\times 10^{-2}$ for a gradient fiber. As the perturbation increases, the share of the azimuthal flux decreases; thus, $\alpha=3.7\times 10^{-2}$ when $a=0.5$, and it reaches saturation $\alpha=2.58\times 10^{-2}$ when $a>8$. It can be shown that perturbation of a CV_{+1}^{+} vortex by the left-circularly polarized HE_{11}^{-} mode does not remove the degeneracy of the singular points, and the vortex field remains structurally stable against the action of the perturbation. Studies of the perturbation of a CV_{-1}^{-} vortex by the HE_{11} mode gave identical results.

The projection of the angular momentum of an unperturbed CV_{+1}^{+} vortex onto the z axis is written as $M_z=-2K\rho F_1 G_1^{-}$. Expressing function G_1^{-} in terms of F_1, according to Ref. 7, we find

$$M_z=-2K\rho\left(\frac{1}{2}\frac{dF_1^2}{dR}-\frac{F_1^2}{R}\right). \tag{16}$$

A CV_{+1}^{+} vortex has right-circular polarization $\hat{\mathbf{e}}^{+}$ and transports topological charge $e=+1$. Both the circular polarization of the vortex and its topological charge correspond to a certain angular momentum. According to Ref. 3, the angular momentum of a vortex in free space can be divided into orbital angular momentum $\mathbf{M}_e$, associated with the value e of the topological charge, and spin $\mathbf{M}_s$, associated with circular polarization. By comparing Eq. (16) with Eq. (10) of Ref. 3, we can conventionally divide the angular momentum for a few-mode fiber into a spin part [the first term in Eq. (16)] and an orbital part [the second term in Eq. (16)].

The propagation of circularly polarized CV vortices is represented as the screwing of a helical wave front into the fiber core according to the right-hand rule. Plane-polarized free-space vortices are characterized by translational displacement (with no rotation) of the wavefront helicoid.

[1] A. A. Sokolov, *Introduction to Quantum Electrodynamics* (GIFML, Moscow, 1958).
[2] W. Heitler, *The Quantum Theory of Radiation* (Clarendon Press, Oxford, 1954; IL, Moscow, 1956).
[3] L. Allen, M. W. Beijersbergen, and R. J. C. Spreeuw, Phys. Rev. A **45**, 8185 (1992).
[4] H. He, N. R. Heckenmberg, and H. Rubinsztein-Dunlop, J. Mod. Opt. **42**, 217 (1995).
[5] H. He, M. E. Friese, and N. R. Heckenber, Phys. Rev. Lett. **75**, 826 (1996).
[6] A. V. Volyar and T. A. Fadeeva, Pis'ma Zh. Tekh. Fiz. **22**, No. 17, 69 (1996) [Tech. Phys. Lett. **22**, 719 (1996)].
[7] A. W. Snyder and J. D. Love, *Optical Waveguide Theory* (Chapman and Hall, New York, 1983; Radio i Svyaz', Moscow, 1987).
[8] A. V. Volyar and T. A. Fadeeva, Pis'ma Zh. Tekh. Fiz. **22**, No. 8, 63 (1996) [Tech. Phys. Lett. **22**, 333 (1996)].
[9] I. V. Basistiy, V. Yu. Bazhenov, M. S. Soskin, and M. V. Vasnetsov, Opt. Comm. **103**, 422 (1993).
[10] Ya. B. Zel'dovich and A. D. Myshkis, *Elements of Applied Mathematics* (Mir, Moscow, 1976).
[11] T. Poston and I. Stewart, *Catastrophe Theory and Its Applications* (Pitman Publishing, Marshfield, Mass., 1978; Mir, Moscow, 1980).
[12] P. Zhermen, *Mechanics of Continuous Media* (Mir, Moscow, 1965).

Translated by W. J. Manthey
Edited by David L. Book

IR-spectroscopic study of the deformation of alkane molecules on a metal surface at high temperature

V. I. Vettegren' and A. I. Tupitsyna

A. F. Ioffe Physicotechnical Institute, Russian Academy of Sciences, St. Petersburg
Institute of Problems of Machine Construction, Russian Academy of Sciences, St. Petersburg
(Submitted June 10, 1997)
Pis'ma Zh. Tekh. Fiz. **23**, 82–86 (November 12, 1997)

An increase of the valence angle in the CH_2 groups of alkane molecules is detected when the crystallites in samples of ceresin grease melt on an aluminum substrate. This effect is explained by compression of the sample because the adhesion to the substrate is strengthened as the crystallites melt. © *1997 American Institute of Physics.* [S1063-7850(97)01511-5]

Samples of OKB-122-7-5 ceresin grease of thickness 1–10 μm on an aluminum substrate have been studied at room temperature and near 90 °C.

The IR spectra of the grease at room temperature contain a doublet at 720–730 cm^{-1} (Fig. 1), which results from the frequency splitting of the pendulum vibrations of the methylene groups in the orthorhombic crystal cell.[1] When the samples are heated to about 85 °C, the indicated doublet disappears, which is a sign of thermal breakdown of the crystallites with an orthorhombic cell.

Figure 2 shows sections of the IR spectra of the grease in the 3000–2800-cm^{-1} region at room temperature and 90 °C. Three strong bands are observed in this region, at 2850, 2920, and 2960 cm^{-1}. It can be seen that the ratio of the intensity of the 2920-cm^{-1} band (A_{2920}) to that of the 2850-cm^{-1} band (A_{2850}) increased upon heating. These bands belong to the symmetric and antisymmetric valence vibrations of the methylene groups.[1] Moreover, the maxima of the indicated bands in the spectra of the melts are shifted toward shorter wavelengths by 5–6 cm^{-1} (the 2920-cm^{-1} band) and by 2–3 cm^{-1} (the 2850-cm^{-1} band).

The intensity in the IR spectra is directly proportional to the square of the derivative of the dipole moment of the transition with respect to the normal coordinate.[2] Let us consider the expressions for the derivatives of the dipole moment of the CH_2–CH_2 group with respect to the normal coordinates $\partial\mu/\partial Q$ of vibrations of type B_{2u} (symmetric) and B_{3u} (antisymmetric).[2]

For B_{2u} vibrations,

$$\partial\mu/\partial Q=\sqrt{2}(\partial\mu_1/\partial q_1+\partial\mu_1/\partial q_2)\cos(\varphi/2)l_{q(sl)}, \quad (1)$$

and, for B_{3u} vibrations,

$$\partial\mu/\partial Q=\sqrt{2}(\partial\mu_1/\partial q_1-\partial\mu_1/\partial q_2)\cos(\varphi/2)l_{q(sl)}, \quad (1a)$$

where $\partial\mu_1/\partial q_1$ and $\partial\mu_1/\partial q_2$ are the derivatives of the dipole moment of the C–H bond in the CH_2 group with respect to its own coordinate and the ''opposite'' coordinate, φ is the valence angle in the CH_2 group, and $l_{q(sl)}$ is the form factor of the vibration.

It follows from Eqs. (1) and (1a) that

$$A_{2920}/A_{2850}=K\tan^2\varphi/2, \quad (2)$$

where K is a factor that depends on the derivatives of the dipole moment of the transition of the CH vibrations with respect to the natural coordinates. It follows from Eq. (2) that the increase of the ratio A_{2920}/A_{2850} can be explained by the increase of the angle φ between the C–H bonds.

When the crystallites in the samples of grease melt, the ratio A_{2920}/A_{2850} increases by a factor of 1.2–1.3. If the initial value of φ is taken to be equal to 109°, it follows from Eq. (2) that such a variation of the intensity ratio of the bands of interest corresponds to a variation of the angle by 5–6°. However, the resulting values may be somewhat overestimated, since we neglected the weak dependence of the term $\partial\mu_1/\partial q_2$ on the valence angle.

The change of the geometry of the CH_2 group must cause several of the terms in the matrices of the kinematic coefficients and the force constants of the molecule to change and consequently must change the characteristic frequencies.[2]

We have calculated the characteristic frequencies of the valence vibrations of the CH_2–CH_2 group with a variable valence angle. The values of the force constants for the original geometry of the $(CH_2)_2$ group were taken from Ref. 3. It was assumed that the frequency shifts of the vibrations of interest were mainly caused by a change of the valence angle in the CH_2 group, and therefore only the terms containing the corresponding coordinate varied in the force-constant matrix. Insignificant variations of the interaction force constants of

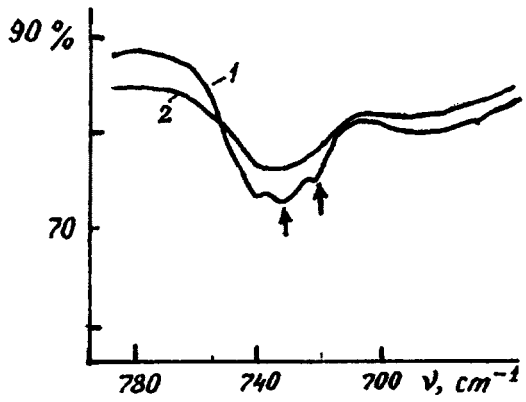

FIG. 1. IR transmission spectrum of OKB-122-7-5 grease on an aluminum substrate in the region 700–800 cm^{-1}. The layer is about 1.5 μm thick. ν is the wave number. The arrows show the 720–730-cm^{-1} doublet. *1*—T=25 °C. *2*—T=90 °C.

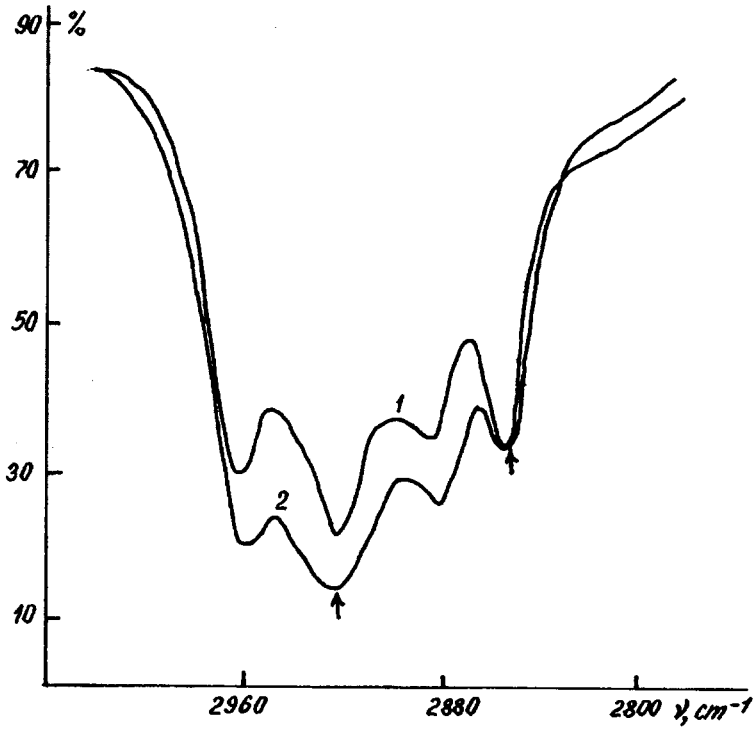

FIG. 2. IR transmission spectrum of OKB-122-7-5 grease on an aluminum substrate in the region 3000–2800 cm^{-1}. The layer is about 5 μm thick. ν is the wave number. The arrows show the bands of the antisymmetric vibrations of the CH groups (about 2920 cm^{-1}) and of the symmetric vibrations of the CH_2 groups (about 2850 cm^{-1}). *1*—T=25 °C, *2*—T=90 °C.

the angular coordinates have no effect on the frequencies of the valence vibrations of the CH bonds. In summary, shifts that agreed with experiment were obtained by increasing φ by 4° and decreasing the force constant of the interaction of the coordinates of the CH bond and angle φ by 0.3×10^6 cm^{-1} (the initial value of this force constant was assumed[3] to be equal to 0.6×10^6 cm^{-1}).

The short-wavelength shifts of the bands of the CH valence vibrations when the crystallites melt can be caused by an increase of the concentration of levo conformers,[4] but increasing the concentration of the levo conformers reduces the total intensities of the bands of interest.[5] We did not detect any decrease of the total integral intensities of the bands of the CH valence vibrations of the methylene groups when the samples were heated to 90°. The total integrated intensities of the bands of interest remain unchanged when the crystallites are melted for samples 1.5 μm thick, whereas they increase for thicker samples (Fig. 1). Consequently, the concentration of levo conformers in the alkane molecules does not increase when the crystallites in the samples of interest melt, and the observed short-wavelength shifts of the bands of interest are caused by an increase of the valence angle in the CH_2 group.

It is well known that the valence angles and the bonds in the molecules vary when the sample is compressed, producing a short-wavelength shift of the characteristic frequencies and changing the band intensities in the IR spectra.[6] The formation of levo conformers is difficult in this case because of steric hindrances that appear when the sample is compressed.

Thus, the changes in the IR spectra of ceresin grease when the samples are heated to 90 °C show that the samples studied here are compressed when the crystallites melt.

This effect, in our opinion, is explained by strengthening of the wetting of the metal substrate (of regions of strong intermolecular interaction) by the sample when the crystallites melt, as well as by an increase of the surface-contact area of the two materials. The strengthening of the adhesion attraction of the alkane molecules to the aluminum substrate can serve as the cause of the compression of the sample.

[1] R. G. Snyder, J. Chem. Phys. **71**, 3229 (1979).
[2] M. V. Vol'kenshteĭn, L. A. Gribov, M. A. El'yashevich, and B. I. Stepanov, *Vibrations of Molecules* (Nauka, Moscow, 1972).
[3] G. A. Gribov, V. A. Dement'ev, and A. T. Todorovskiĭ, *Interpreted Vibrational Spectra of Alkanes, Alkenes, and Benzene Derivatives* (Nauka, Moscow, 1986).
[4] R. G. Snyder, H. L. Strauss, and C. A. Elliger, J. Phys. Chem. **86**, 5145 (1982).
[5] H. L. Casal, D. G. Cameron, and H. H. Mantch, Can. J. Chem. **84**, 1736 (1983).
[6] P. T. T. Wong, T. E. Chagwedera, and H. H. Mantch, J. Chem. Phys. **87** (1987).

Translated by W. J. Manthey
Edited by David L. Book

The effect of laser radiation on the permeability of porous membranes

I. K. Meshkovskiĭ, O. V. Klim, and S. N. Dmitriev

St. Petersburg State Institute of Precision Mechanics and Optics (Technical University)
(Submitted June 18, 1997)
Pis'ma Zh. Tekh. Fiz. **23**, 87–90 (November 12, 1997)

This paper discusses studies of the effect of laser radiation on the permeability of thin porous polymeric membranes performed at the Joint Institute for Nuclear Research, Dubna. It is shown that the electrodiffusion rate through the membrane is substantially reduced when molecular ions are efficiently photoexcited. The effect of temperature on the electrodiffusion process is studied. [S1063-7850(97)01611-X]

A number of papers[1–3] have shown that photoexcitation of the electronic and vibrational subsystems of molecules in the gas phase reduces their mobility in porous membranes. Moreover, studies have been made of how laser radiation affects the mobility of dissolved molecular ions[3] on samples of porous glass.

The purpose of the present work was to investigate how laser radiation affects the electrodiffusion flux of molecular ions of certain laser dyes dissolved in ethanol in connection with electromigration through thin porous polymeric membranes. This is a question of keen interest for the study of laser action on biological objects.

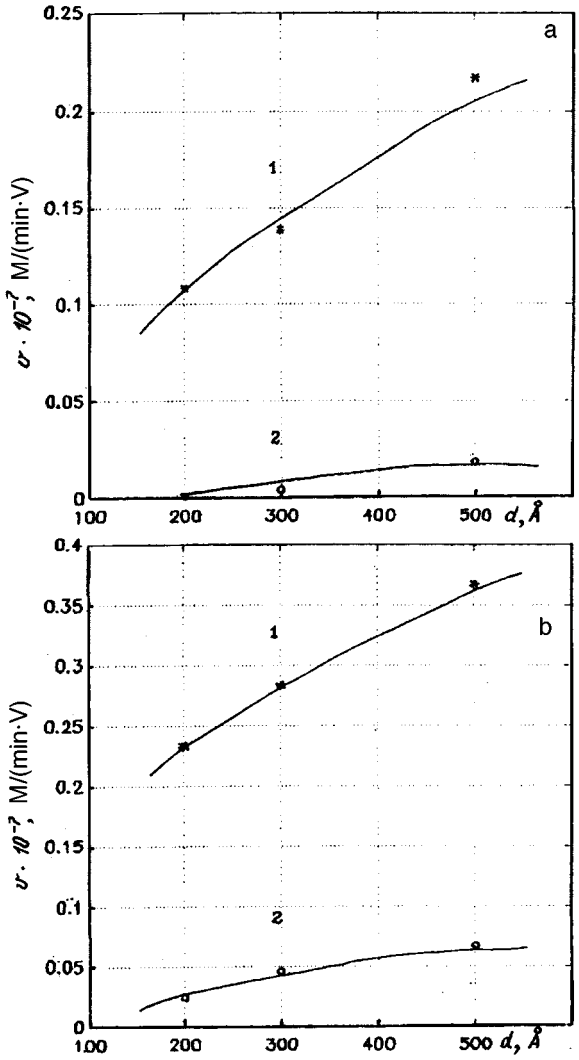

FIG. 1. Electrodiffusion rate of dye vs membrane pore diameter without laser irradiation. (a) for rhodamine G: *1*—at a temperature of 60 °C, *2*—at 20 °C; (b) for thionine: *1*—at 60 °C, *2*—at 20 °C.

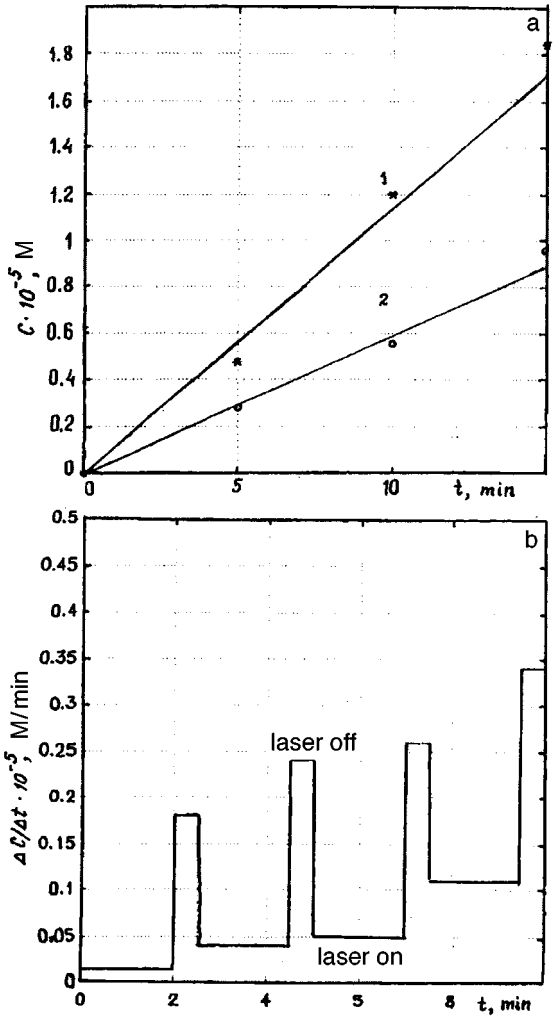

FIG. 2. (a) Time variation of the concentration of rhodamine G during electrodiffusion through a membrane with a pore diameter of 30 nm for a voltage of 900 V across the electrodes: *1*—with no laser irradiation, *2*—with simultaneous laser irradiation; (b) electrodiffusion rate of thionine vs time during electrodiffusion through a membrane with a pore diameter of 20 nm for a voltage of 900 V across the electrodes.

Experimental part. Porous nylon membranes 10 μm thick, with 20-, 30-, and 50-nm pores were used for the experiment. The experiments were carried out in a sample cell consisting of two sections that were partitioned off by a porous membrane. The left-hand part of the cell was filled with an ethanol solution of dye with a concentration of 10^{-3} M and contained the anode, while the right-hand part of the cell contained pure ethanol, the cathode, and a photometric fiber-optic probe. The surface of the membrane was accessible to radiation from an LG-106M-1 argon laser.

An automatic spectrophotometric apparatus was used to measure the diffusion flux through the membrane.

Figure 1a shows how the electrodiffusion rate of the dye rhodamine G for membranes depends on pore diameter at temperatures of 20 and 60 °C without laser irradiation. Figure 1b shows the corresponding curves for thionine.

When membranes with pore diameters of 30 and 20 nm are irradiated by an argon laser with a power density of about 15 W/cm^2, the diffusion flux rate is substantially reduced; this is illustrated by the curves shown in Fig. 2, where trace *1* of Fig. 2a and the dependence in Fig. 2b are plotted taking into account the photobleaching dynamics of the dye. Reducing the applied radiation power to 5 W/cm^2 for thionine and to 1.5 W/cm^2 for rhodamine G caused the observed slowdown of the diffusion flux to disappear. No effect of the laser radiation on the electrodiffusion rate was observed for membranes with a pore diameter of 50 nm.

Discussion of the results. It follows from the data of Figs. 1a and 1b that the electromigration rate increases with increasing temperature. The data of Figs. 2a and 2b show that irradiating the molecules with exciting laser radiation substantially reduces the electrodiffusion rate. These results correspond to those obtained by studying the analogous behavior for porous glass.

The results show that the slowdown of the molecular ions during electromigration through thin polymeric membranes has a threshold dependence on the laser radiation power and largely depends on the size of the membrane pores and the molecular structure of the ion.

The results obtained in Refs. 1–3, as well as the materials of this paper, make it possible to conclude that the action of exciting radiation reduces the permeability of porous membranes. This conclusion can explain certain physiological effects that accompany laser irradiation of biological objects.

Moreover, the detected regularity makes it possible to carry out application-oriented work on the separation and purification of materials.

[1] N. V. Karlov, I. K. Meshkovskiĭ, N. P. Petrov, Yu. N. Petrov, and A. M. Prokhorov, JETP Lett. **30**, 42 (1979).
[2] V. A. Kravchenko, E. N. Lotkova, I. K. Meshkovskiĭ, and Yu. N. Petrov, Pis'ma Zh. Tekh. Fiz. **7**, 1197 (1981) [Sov. Tech. Phys. Lett. **7**, 512 (1981)].
[3] I. K. Meshkovskiĭ and O. V. Klim, Pis'ma Zh. Tekh. Fiz. **23**, No. 10, 4 (1997) [Tech. Phys. Lett. **23**, 378 (1997)].

Translated by W. J. Manthey
Edited by David L. Book

Polarization switching with four-wave mixing of copropagating light waves in birefringent fibers

S. A. Podoshvedov

Chelyabinsk State Technical University
(Submitted October 16, 1996; accepted for publication May 14, 1997)
Pis'ma Zh. Tekh. Fiz. **23**, 91–95 (November 12, 1997)

A system of equations is graphically solved that describes the copropagating interaction of four waves in a birefringent fiber. It is proposed to use this type of interaction for polarization switching. © *1997 American Institute of Physics.* [S1063-7850(97)01711-4]

Four-wave mixing of counterpropagating light waves that are nondegenerate in frequency but have coincident polarizations was discussed in Ref. 1, where the optical power-switching effect was predicted. This paper presents an analysis of interaction in birefringent fibers of four copropagating waves that are nondegenerate both in frequency and in polarization. By solving this question, it becomes possible to use copropagating four-wave mixing in a birefringent fiber for purposes of polarization switching. With polarization switching, the polarization state of one light wave participating in the interaction sharply changes at the output from the fiber when there is a slight change of the initial polarization state of another wave. As shown by the analysis, the polarization-switching effect with four-wave copropagating mixing is possible at any wavelength.

In a birefringent fiber, an elliptically polarized wave decays into two linearly polarized waves. The total electric field of the two initally elliptically polarized waves with frequencies ω_1 and ω_2 can therefore be represented as

$$\mathbf{E}=\frac{1}{2}\left\{\hat{\mathbf{x}}\sum_{i=1}^{2}E_{ix}(z)F_{ix}(x,y)\exp[-i(\omega_i t-k_{ix}z)]+\hat{\mathbf{y}}\sum_{i=1}^{2}E_{iy}(z)F_{iy}(x,y)\exp[-i(\omega_i t-k_{iy}z)]\right\}, \quad (1)$$

where $F_i(x,y)$ is the spatial distribution of the field over the cross section of the waveguide, $k_i=(n_i\omega_i)/c$, n_i are the effective refractive indices for the corresponding modes of the lightguide, $\hat{\mathbf{x}}$ is the slow axis, and $\hat{\mathbf{y}}$ is the fast axis of the fiber. The evolution of amplitudes E_i obeys a system of four coupled equations, which in the paraxial approximation have the form

$$\frac{dE_{1x}}{dz}=iR\frac{2}{3}f_{1234}E_{2x}^{*}E_{1y}E_{2y}e^{-i\Delta kz}+iRE_{1x}\left(f_{11}|E_{1x}|^2+2f_{12}|E_{2x}|^2+\frac{2}{3}f_{13}|E_{1y}|^2+\frac{2}{3}f_{14}|E_{2y}|^2\right), \quad (2a)$$

$$\frac{dE_{2x}}{dz}=iR\frac{2\lambda_1}{3\lambda_2}f_{2134}E_{1x}^{*}E_{1y}E_{2y}e^{-i\Delta kz}+iRE_{2x}\frac{\lambda_1}{\lambda_2}\times\left(2f_{21}|E_{1x}|^2+f_{22}|E_{2x}|^2+\frac{2}{3}f_{13}|E_{1y}|^2+\frac{2}{3}f_{14}|E_{2y}|^2\right), \quad (2b)$$

$$\frac{dE_{1y}}{dz}=iR\frac{2}{3}f_{3412}E_{2y}^{*}E_{1x}E_{2x}e^{i\Delta kz}+iRE_{1y}\left(\frac{2}{3}f_{31}|E_{1x}|^2+\frac{2}{3}f_{32}|E_{2x}|^2+f_{33}|E_{1y}|^2+2f_{34}|E_{2y}|^2\right), \quad (2c)$$

$$\frac{dE_{2y}}{dz}=iR\frac{2\lambda_1}{3\lambda_2}f_{4312}E_{1y}^{*}E_{1x}E_{2x}e^{i\Delta kz}+iRE_{2y}\frac{\lambda_1}{\lambda_2}\left(\frac{2}{3}f_{41}|E_{1x}|^2+\frac{2}{3}f_{42}|E_{2x}|^2+2f_{43}|E_{1y}|^2+f_{44}|E_{2y}|^2\right). \quad (2d)$$

Here the following notation has been introduced: $R=(\pi n_2)/\lambda_1$ (n_2 is the nonlinear refractive index), $\Delta k=k_{1x}-k_{1y}+k_{2x}-k_{2y}$ is the detuning of the wave vectors, and $f_{ijkl}=(\langle F_i^{*}F_j^{*}F_kF_l\rangle)/((\langle|F_i|^2\rangle\langle|F_i|^2\rangle\langle|F_k|^2\rangle<|F_l|^2)^{1/2})$ is the overlap integral (the brackets denote averaging over the cross section of the fiber). It was assumed that $\chi^{(3)}_{xyyx}=\chi^{(3)}_{xyxy}=\chi^{(3)}_{xxyy}=\chi^{(3)}_{xxxx}/3=\chi^{(3)}_{yyyy}/3$. Equations (2) are the most general equations; they contain the terms responsible for the self- and cross-phase modulation effects, as well as for energy exchange. To simplify the formulas, it will be assumed in what follows that all the overlap integrals are approximately identical; i.e., $f_{ijkl}\simeq f_{ij}\simeq 1/A_{\text{eff}}$, where A_{eff} is the effective area of the mode. Then $R=(\pi n_2)/(\lambda_1 A_{\text{eff}})$. The system of equations (2) allows the existence of the following conserved quantities (integrals of motion): $|E_{1x}|^2-(\lambda_2/\lambda_1)|E_{2x}|^2=D_1$, $|E_{1y}|^2-(\lambda_2/\lambda_1)|E_{2y}|^2=D_2$, and $|E_{1x}|^2+(\lambda_2/\lambda_1)|E_{2x}|^2+|E_{1y}|^2+(\lambda_2/\lambda_1)|E_{2y}|^2=P$. After replacing variables $E_{1x}=q\sqrt{P}$, $E_{2x}=q_2\sqrt{(\lambda_1 P)/\lambda_2}$, $E_{1y}=q_3\sqrt{P}$, and $E_{2y}=q_4\sqrt{(\lambda_1 P)/\lambda_2}$, the system of Eqs. (2) can be transformed to a system of two differential equations for the real quantities $\eta(s)=|q_1|^2$ and $\psi(s)=\varphi_{1x}+\varphi_{2x}-\varphi_{1y}-\varphi_{2y}+ks$. The new system has the form $\partial\psi/\partial s=\partial H/\partial\eta$, $\partial\eta/\partial s=-\partial H/\partial\psi$, where H is the Hamiltonian

$$H=\frac{2}{3}\cos\psi\sqrt{\eta}\sqrt{\eta-d_1}\sqrt{1+d_1+d_2-2\eta}\sqrt{1+d_1-d_2-2\eta}+\frac{\eta^2}{3}\left(4+\frac{\lambda_1}{\lambda_2}+\frac{\lambda_2}{\lambda_1}\right)+\left[-\frac{d_1}{3}\left(8+\frac{3\lambda_1}{2\lambda_2}+\frac{\lambda_2}{2\lambda_1}\right)+\frac{d_2}{6}\left(\frac{\lambda_1}{\lambda_2}-\frac{\lambda_2}{\lambda_1}\right)-\frac{1}{3}\left(4+\frac{\lambda_1}{2\lambda_2}+\frac{\lambda_2}{2\lambda_1}\right)+k\right]\eta. \quad (3)$$

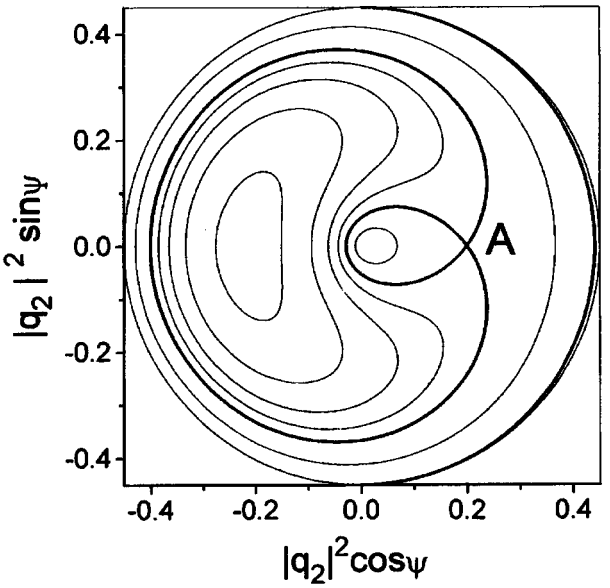

FIG. 1. Phase portrait of the system of equations (3) for $k=0.1$.

Here $d_1=D_1/P$, $d_2=D_2/P$, $s=z\rho$, $\rho=1/L_{\rm nl}=(RP\lambda_1)/\lambda_2$, $k=\Delta k/\rho$; $|q_2|^2$, $|q_3|^2$, $|q_4|^2$ are expressed in terms of η: $|q_2|^2=\eta-d_1$, $|q_3|^2=(1+d_1+d_2-2\eta)/2$, and $|q_4|^2=(1+d_1-d_2-2\eta)/2$. To analyze the system of Eqs. (3), we assume the following values: $\lambda_1=1.06$ μm, $\lambda_2=0.9$ μm, and $d_1=d_2=0.05$. For the given values, Fig. 1 shows the graphical solution of the system of Eqs. (3) ($H=$ const) for $|q_2|^2$ when $k=0.1$. The stable eigenmodes are the centers on the phase plane, while the unstable eigenmode is a point of the unstable saddle type (denoted by A), which gives the beginning of a two-branch separatrix (the eigenmodes are determined from the condition[1,2] $\partial H/\partial\eta_{(\eta_e,\psi_e)}=\partial H/\partial\psi_{(\eta_e,\psi_e)}=0$. Besides the two-loop separatrix, there exists a simple separatrix (all the separatrices are distinguished by thicker lines) beginning at the point $\eta=0.45$, $\psi=(3\pi)/2$ and ending at the point $\eta=0.45$, $\psi=\pi/2$. Let us consider the possibility that the polarization-switching effect will appear. Figure 2 shows the $E_{2x}(s)|^2/P_{in}$ dependence, ($P_{in}=|E_{1x}(s=0)|^2+|E_{2x}(s=0)|^2+|E_{1y}(s=0)|^2+|E_{2y}(s=0)|^2$, $P_{in}\neq$ const) as a function of $s=z/L$ (L is the length of the fiber). Curve *1* corresponds to the case in which the final polarization state of a light wave with frequency ω_2 remains unchanged (we assume the length of the fiber to be equal to the oscillation period of curve *1*). As can be seen from Fig. 2, a ''slight'' change of the polarization state of the light wave with wavelength λ_1 (a change of the power of the $\hat{\mathbf{x}}$ and $\hat{\mathbf{y}}$ modes of the pump wave of the order of hundredths of a percent of the total power) greatly strengthens the light wave with wavelength λ_2, polarized along the fast axis (E_{2y}) at the output from the fiber (curve *2*). Moreover, the ratio of $|q_{2\max}|^2$ (curve *1*) to $|q_{2\min}|^2$ (curve *2*) equals 9.43 for almost identical boundary conditions.

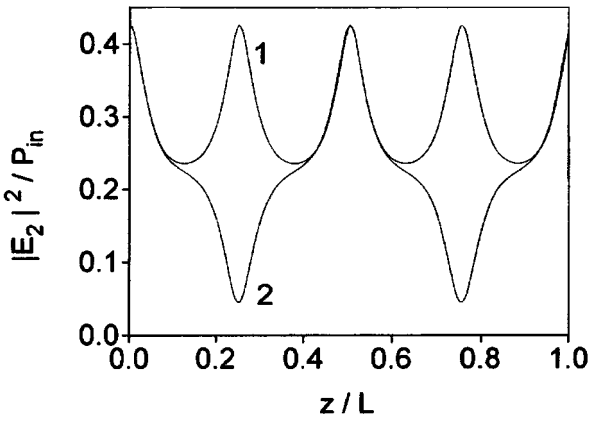

FIG. 2. Relative power ($|E(s)_{2x}|^2/P_{in}$) of the light wave with frequency ω_2 and polarization directed along the slow axis $\hat{\mathbf{x}}$, as a function of distance $s=z/L$ (L is the length of the fiber). Curves *1* and *2* correspond to the cases in which the initial points on the phase portrait lie outside and inside the separatrix ($L/L_{nl}=50$).

[1] S. A. Podoshvedov, Opt. Spektrosk. **83** (in press) [Opt. Spectrosc. **83** (to be published)].
[2] S. Trillo and S. Wabnitz, Opt. Lett. **17**, 1572 (1992).

Translated by W. J. Manthey
Edited by David L. Book

Stress field at the boundary of a wedge-shaped twin

V. S. Savenko and O. M. Ostrikov

Moscow State Pedagogical Institute
(Submitted November 28, 1996; resubmitted May 17, 1997)
Pis'ma Zh. Tekh. Fiz. **23**, 1–6 (November 26, 1997)

A model is proposed to calculate the stress field at the boundary of a wedge-shaped twin which can allow for its degree of coherence. It is shown that the stress field decreases exponentially with increasing distance from the twinning boundary. © *1997 American Institute of Physics.* [S1063-7850(97)01811-9]

When studying the interaction between dislocations and a wedge-shaped twin, the authors of Ref. 1 represented this twin as infinitely thin compared with its dimensions and compared with the distance between it and the dislocations. In this case, the twin was modeled as a dislocation wall. This model allows the stress field to be calculated fairly accurately at large distances from the twin. However, for calculations of the stress field in the immediate vicinity of the twin, the dislocation wall model yields appreciable errors[2,3] and to avoid these, the twinning boundary must be modeled as a dislocation pile-up which would take into account the characteristics of its dislocation structure. These conditions are satisfied by our proposed model whereby the twinning boundary may be represented as a dislocation ladder, i.e., a pile-up of edge dislocations in which each dislocation is positioned relative to the other such that the entire combination forms an infinite number of steps distributed along some straight line (Fig. 1). In this case, the Burgers vectors of all the dislocations are directed along the X axis in the same direction. The components of the stress tensor created by this dislocation pile-up in an isotropic medium are defined by the expressions:

$$\sigma_{xx}=-hA\sum_{n=-\infty}^{\infty}\frac{(n+q)[3d^2(n+p)^2+h^2(n+q)^2]}{[d^2(n+p)^2+h^2(n+q)^2]^2},$$

$$\sigma_{yy}=hA\sum_{n=-\infty}^{\infty}\frac{(n+q)[d^2(n+p)^2-h^2(n+q)^2]}{[d^2(n+p)^2+h^2(n+q)^2]^2}, \qquad (1)$$

$$\sigma_{xy}=dA\sum_{n=-\infty}^{\infty}\frac{(n+p)[d^2(n+p)^2-h^2(n+q)^2]}{[d^2(n+p)^2+h^2(n+q)^2]^2},$$

where n is the dislocation number.

The following notation is introduced in formula (1)

$$A=\frac{bG}{2\pi(1-\nu)}, \quad p=\frac{x}{d}, \quad q=\frac{y}{h}. \qquad (2)$$

Here b is the Burgers vector, G is the shear modulus, ν is the Poisson ratio, and d and h are the projections of the segment connecting neighboring dislocations on the X and Y axes, respectively (Fig. 1). The projections of the Burgers vector are obviously $b_x=b$, $b_y=0$, and $b_z=0$. Applying the theory of Fourier series,[4] the sums (1) may be reduced to the form

$$\sigma_{xx}=-\frac{hA}{d^2+h^2}\left(\zeta_1 I_2+\xi_1\frac{\partial I_1}{\partial q}+\gamma_1\frac{\partial J}{\partial q}\right),$$

$$\sigma_{yy}=\frac{hA}{d^2+h^2}\left(\zeta_2 I_2+\xi_2\frac{\partial I_1}{\partial q}+\gamma_2\frac{\partial J}{\partial q}\right), \qquad (3)$$

$$\sigma_{xy}=\frac{dA}{d^2+h^2}\left(\zeta_3 I_1+\xi_3\frac{\partial I_2}{\partial p}+\gamma_3\frac{\partial J}{\partial p}\right).$$

Here, we have

$$\zeta_1=3d^2+h^2, \quad \zeta_1=\zeta_2=2d^2(q-p),$$

$$\gamma_1=\gamma_2=-2d^2q(q-p),$$

$$\zeta_2=\zeta_3=d^2-h^2, \quad \xi_3=2h^2(q-p), \quad \gamma_3=h^2(p^2+q^2),$$

$$I_1=\frac{\pi}{d(d^2+h^2)}\frac{d\,\sin\alpha+h\,\sinh\beta}{\cosh\beta-\cos\alpha},$$

$$I_2=\frac{\pi}{h(d^2+h^2)}\frac{h\,\sin\alpha-d\,\sinh\beta}{\cosh\beta-\cos\alpha},$$

$$\frac{\partial I_1}{\partial q}=\frac{2\pi^2 h}{d(d^2+h^2)}\frac{\sin\alpha\,\sinh\beta}{(\cosh\beta-\cos\alpha)^2},$$

$$\frac{\partial I_2}{\partial p}=\frac{d^2}{h^2}\frac{\partial I_1}{\partial q},$$

$$\frac{\partial J}{\partial q}=\frac{\pi}{dh(q-p)^2}\frac{\sinh\beta}{\cosh\beta-\cos\alpha}-\frac{2\pi^2}{d(d^2+h^2)(q-p)}\times\frac{d(1-\cosh\beta\,\cos\alpha)-h\,\sinh\beta\,\sin\alpha}{(\cosh\beta-\cos\alpha)^2},$$

$$\frac{\partial J}{\partial p}=-\frac{\pi}{dh(q-p)^2}\frac{\sinh\beta}{\cosh\beta-\cos\alpha}+\frac{2\pi^2}{h(d^2+h^2)(q-p)}\times\frac{h(1+\cosh\beta\,\cos\alpha)+d\,\sinh\beta\,\sin\alpha}{(\cosh\beta-\cos\alpha)^2}$$

The following notation is introduced in these functions:

$$\alpha=2\pi\frac{d^2p+h^2q}{d^2+h^2}, \quad \beta=2\pi\frac{dh(q-p)}{d^2+h^2}.$$

For a computer analysis of the results it is convenient to use the ratio σ_{ij}/A, which does not have any special physical meaning in itself, but allows the numerical value of the con-

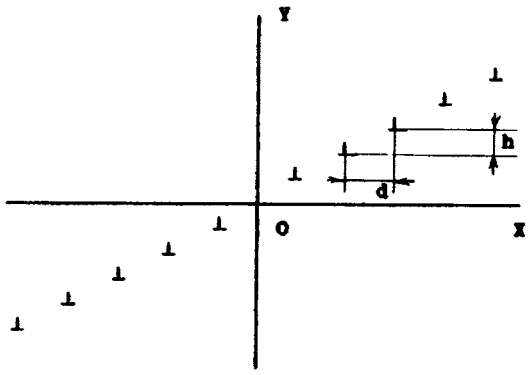

FIG. 1. View of twinning boundary.

stant A to be neglected in the calculations, since the curves of σ_{ij}/A and σ_{ij} as a function of p and q are almost identical in form.

Curves of σ_{ij}/A as a function of p and q are shown schematically in Fig. 2, where d and h are taken to be unity. It can be seen from these curves that the stresses are highest at the twinning boundary which lies in the pOq plane and passes through the origin at angle of 45° (since d and h are equal) to the p axis. With increasing distance from the boundary, the stress fields decay exponentially.

The configuration of the fields of normal stresses generated along the X axis (Fig. 2a) resembles that of the stress fields created around a single dislocation. This similarity was also observed in Ref. 3 but for an analysis of a dislocation wall. Figure 2b, which gives σ_{yy}/A as a function of p and q, clearly shows exponentially decaying stresses with increasing distance from the twinning dislocations, i.e., partial dislocations forming the twinning boundary being studied. The difference between the normal stresses σ_{xx} and σ_{yy} can be explained by the fact that this twinning boundary consists of dislocations of the same sign, creating different stresses in mutually perpendicular directions. The form of the cleavage stresses (Fig. 2c) shows that they decrease rapidly with increasing distance from the dislocation pile-up modeling the twinning boundary.

The proposed model to calculate the stress fields at a twinning boundary has some advantages over that considered in Ref. 1. It can take into account the degree of coherence of the twinning boundary, defined by the ratio HL, where L is the length of the twin and H is the width at its mouth. These values are proportional to d and h:

$$\frac{H}{L}=\frac{h}{2d}. \tag{4}$$

Having determined the expansion angle of the wedge-shaped twin α (here $\alpha=\arctan(H/L)$), we can use expression (4) to find the relation between the parameters d and h which describe the relative position of the twinning dislocations, and the experimentally observed values L and H. This means that formula (3) can be used to determine the stresses at the boundaries of these twins. This cannot be achieved with the model proposed in Ref. 1 because this only uses one parameter h, which determines the distance between the dislocations and is unrelated to the experimentally observed values.

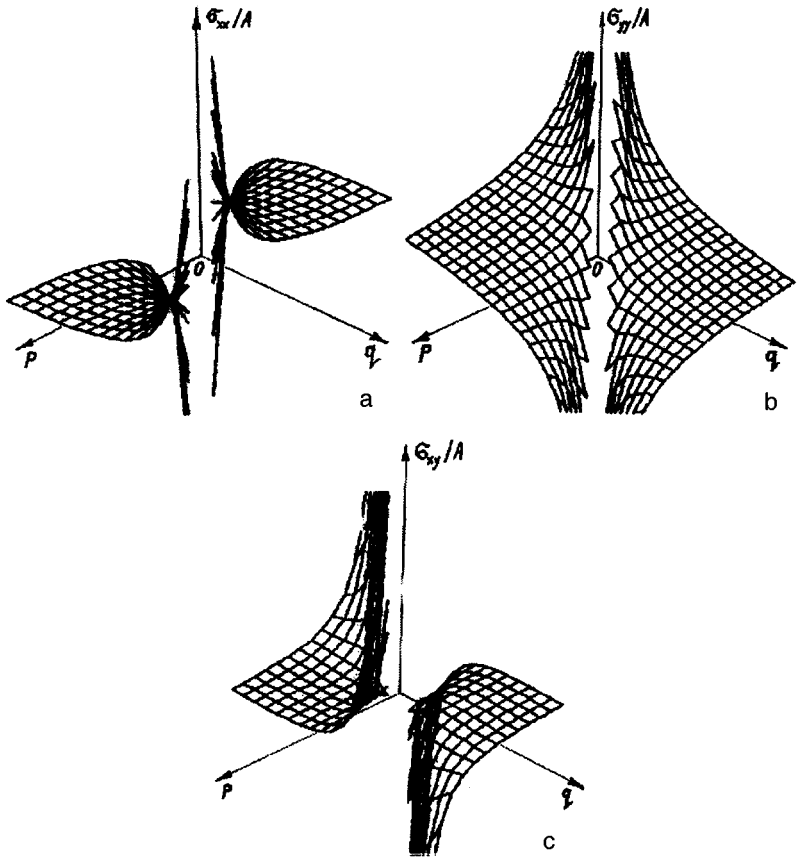

FIG. 2. Curves of σ_{ij}/A as a function of p and q: a — σ_{xx}/A, b— σ_{yy}/A, and c — σ_{xy}/A.

[1] V. I. Bashmakov, M. E. Bosin, and M. M. Brodskiĭ, Izv. Vyssh. Uchebn. Zaved. Fiz. No. 2, 110 (1974).
[2] J. P. Hirth and J. Lothe, *Theory of Dislocations* (McGraw-Hill, New York, 1967; Atomizdat, Moscow 1972).
[3] A. A. Predvoditelev, N. A. Tyapunina, G. M. Zinenkova, and G. V. Bushuev, *Physics of Crystals with Defects* [in Russian], Moscow State University Press, Moscow (1986).
[4] A. P. Prudnikov, Yu. A. Brychkov, and O. I. Marichev, *Integrals and Series*, Vols. 1–3 (Gordon and Breach, New York, 1986, 1986, 1989) [Russ. original, Vols. 1–3, Nauka, Moscow, 1981, 1983, 1986].

Translated by R. M. Durham

Dynamic laws and superhydrodynamics

G. E. Skvortsov

St. Petersburg State University
(Submitted March 5, 1997)
Pis'ma Zh. Tekh. Fiz. **23**, 7–11 (November 26, 1997)

Dynamic laws are formulated which provide the basis of the macroscopic theory of highly nonequilibrium processes — superhydrodynamics.
[S1063-7850(97)01911-3]

Qualitative laws governing the behavior of systems exposed to strong perturbations were formulated and discussed in Refs. 1 and 2.

Here an analysis is made of the main dynamic laws which can be used to obtain a closed description (equation) of highly nonequilibrium processes: the ''rate-action' law, the balance law, the principle of abbreviated description, and also the antipode of Le Chatelier's principle for active systems.

These laws provide the basis for a macrodynamic theory of highly nonequilibrium processes — superhydrodynamics. This theory is designed to describe processes in a wide range of systems, in nuclei and atoms containing more than a hundred nucleons and electrons, gases and condensed media, and also in stellar systems.

1. The rate-action law relates the time variation of an object — a system of velocity characteristics — with an internal or external action on the system.

An example of the application of this law may the Newton-Meshcherskiĭ equations

$$d_t\mathbf{x}=\mathbf{v}, \quad d_t\mathbf{v}=\frac{1}{m}\mathbf{f}(\mathbf{xv}t), \quad d_t m=j_m(\mathbf{xv}t). \tag{1}$$

The second and third equations respectively imply that the rate of change in velocity is equal to the action (force) with the coefficient $1/m$ and the rate of change in mass is equal to its rate of loss or gain.

All known and new equations for any physical quantities can be obtained similarly by using suitable balance relations for internal actions.

2. The balance relations reflect an extremely general law of balance. This law is an expression of the action of opposite influences of significant quantities (forces, energies, other resources). All dynamic systems fluctuate in a balanced way. Stability of these systems is achieved by means of balance.

Balance relations — the law of active masses — are used to obtain chemical kinetics equations. Stability criteria are balance relations[3] and the degree of nonequilibrium has a balance nature.[2]

The balance of resource A, generally an energy flux entering and leaving the system, determines the transition from a passive (absorption predominates) to an active system (emission predominates):

$$\Delta A(t)=A_{in}(t)-A_{out}(t)<0. \tag{2}$$

This generally occurs when the internal reservoir of resource A is opened as a result of the action A_{in}.

Active or activated systems include explosive and combustible substances, media with a fairly high concentration of electronically excited particles, the strongly overheated phase, and so on.

It may be stated that for active systems or systems in an active state, the antipode of Le Chatelier's principle holds: the reaction of the system amplifies the action exerted upon it. The system deactivates and is transferred to its preactivation form in the presence of a limiter, or it breaks up and becomes a different system (explosion, combustion, gravitational collapse).

3. The principle of abbreviated description is an important factor for obtaining equations for highly nonequilibrium processes.

This principle follows as a necessary consequence of the law of ''universal relation and mutual influence'' and consists of three propositions: 1) the unbounded ''expansion'' of a system as the intensity of the process increases necessitates a suitable abbreviation of the description; 2) a system consisting of more than hundreds of particles should be considered as a suitable continuous medium having a structure; 3) the abbreviation of the description and the transition to a continuous medium are accomplished most effectively by means of a projection method. In the first proposition the ''expansion'' of the system implies the involvement of deeper and deeper levels of the system structure in the process and also a wider and wider environment as the source of action in unstable states of the system typical of highly nonequilibrium processes.

4. To demonstrate an abbreviated description, let us obtain simple variant of superhydrodynamics.

Let us take as the initial equation the general dynamic equation for a quantity f describing the microdynamics and select a set of macroscopic quantities A of interest to us, which correspond to a subspace with the projector P. Let us take

$$\partial_t f=\mathcal{E}f, \quad f=Pf+Qf, \quad Q=1-P, \quad PQ=0. \tag{3}$$

The separation of f into P and Q components is completely analogous to isolating the final sum and residue of a Fourier series, respectively.

Assuming for simplicity that the evolution operator $\mathcal{E}$ is linear and the projector P is steady-state, we formally obtain a closed equation for the quantity $Pf\equiv f_A$ (Ref. 4):

$$\partial_t f_A = P\mathcal{E} f_A + P\mathcal{E}[\partial_t - \hat{\mathcal{E}}]^{-1} f_A, \quad \hat{\mathcal{E}} \equiv Q\mathcal{E}. \tag{4}$$

Considering for simplicity the density $Pf = \rho$, we obtain from Eq. (4) the superdiffusion equation (in the Laplace–Fourier representation)

$$z\rho - \rho_0 = -\mathbf{u}_s \cdot i\mathbf{k}\rho + ik_i K_d^{(ij)} ik_j \rho, \tag{5}$$

$$K_d^{(ij)}(zkF) = \langle \hat{v}_i, [z - \hat{\mathcal{E}}]^{-1} \hat{v}_j \rangle \tag{6}$$

i.e., the nonequilibrium diffusion tensor.[4]

The most general nonlinear system for obtaining superhydrodynamics can be found in Ref. 5. In this general case, the determining relations — expressions for the fluxes J_n in terms of the forces X_e — are defined by the kinetic operators $K_{ne}[X]$. In accordance with their general expressions,[5] for high velocities, gradients, and forces these also possess qualitative asymptotic behavior

$$K_{ne} \sim \frac{c_1}{\partial/\partial t}, \quad \frac{c_2}{|\nabla|}, \quad \frac{c_3}{|F|}. \tag{7}$$

Similar dependences with specific values of c_k are also found for K_d (6).

The rate asymptotic expression agrees with the phenomenological relaxation theory; the gradient asymptotic form gives the first-order theory in terms of gradients with dissipation; the force asymptotic form indicates a weak dependence of the corresponding current on the force when this is large.

5. The general nature of the description abbreviation procedure allows different microdynamic equations to be used as the initial equation: the general kinetic equation for structure-kinetic elements,[4,5] the Liouville equation (Mori, Zwanzig, Richardson), and also the Schrödinger equation for a molecular system.

In this last case, a nonequilibrium variant of the Born–Oppenheimer theory is obtained to abbreviate the description in terms of the nuclear degrees of freedom of the molecule. The description abbreviation procedure, as applied to a nucleus, is a very useful superhydrodynamic model of the nucleus.

By applying the projection operator method to the corresponding problem in quantum field theory, it was possible to calculate the Lamb shift naturally without an artificial renormalization procedure.[6]

By applying this method of abbreviated description to the Liouville equation, it is possible to demonstrate the transition from a reversible to an irreversible description. To achieve this, it is sufficient for the Liouville operator to have a continuous spectrum, which is physically obvious. The defect of vanishing relaxation frequency, indicated by the author,[4] can then be eliminated.

The Fokker–Krylov problem of atomic decay, solved using the projection operator method, specifies an exponential dependence for moderately long times.

In the problem of boundary-layer flow of a turbulent liquid a strict expression for the turbulent viscosity was first given to obtain equations for the averaged motion based on the Navier-Stokes equation with a random force simulating the stochastic interaction of the vortices.[7]

To conclude, it should be noted that the principle of abbreviated description prescribes a dependence of various characteristics, including quasiparticle ones, on the dynamic state of the system. Characteristics such as the quasiparticle mass, nonequilibrium transport coefficients, and the apparent mass of a body in hydrodynamics, may alter their values by an order of magnitude in the course of the process. Similar effective characteristics should be obtained by the projection operator method using an interpolation-asymptotic method of specification, as was done in Refs. 4 and 5.

[1] G. E. Skvortsov, Pis'ma Zh. Tekh. Fiz. **17**(6), 15 (1990) [Sov. Tech. Phys. Lett. **17**, 1647 (1990)].
[2] G. E. Skvortsov, Pis'ma Zh. Tekh. Fiz. **23**(6), 85 (1997); **23**(7), 23 (1997); **23**(10), 17 (1997) [Tech. Phys. Lett. **23**, 246 (1997); **23**, (1997); **23**, 383 (1997)].
[3] E. N. Perevoznikov and G. E. Skvortsov, Zh. Tekh. Fiz. **52**, 2353 (1982) [Sov. Phys. Tech. Phys. **27**, 1451 (1982)].
[4] G. E. Skvortsov, Zh. Eksp. Teor. Fiz. **63**, 502 (1972); **68**, 956 (1975) [Sov. Phys. JETP **36**, 266 (1973); **41**, 473 (1975)].
[5] G. E. Skvortsov, Vestn. Lenin. Gos. Univ. No. 13, 94 (1979).
[6] J. Seke, J. Phys. A **24**, 2121 (1991).
[7] G. E. Skvortsov, Zh. Tekh. Fiz. **59**(3), 62 (1989) [Sov. Phys. Tech. Fiz. **34**, 289 (1989)].
[8] E. N. Perevoznikov and G. E. Skvortsov, Zh. Tekh. Fiz. **61**(9), 1 (1991) [Sov. Phys. Tech. Phys. **36**, 967 (1991)].

Translated by R. M. Durham

''Semiconductor–metal'' conductivity phase transition temperature in chalcogenide glassy semiconductors and overheating effect

É. A. Lebedev and K. D. Tséndin

A. F. Ioffe Physicotechnical Institute, Russian Academy of Sciences, St. Petersburg
(Submitted July 12, 1997)
Pis'ma Zh. Tekh. Fiz. **23**, 12–17 (November 26, 1997)

It is shown that thin films of chalcogenide glassy semiconductors may repeatedly withstand short-term heating to temperatures substantially in excess of the ''semiconductor–metal'' transition temperature and the melting point T_m without being damaged. © *1997 American Institute of Physics.* [S1063-7850(97)02011-9]

It is known that in chalcogenide glassy semiconductors exposed to a strong electric field ($\sim 10^5$ V/cm), a reversible phase transition takes place from semiconducting conductivity $\sigma=\sigma_0\exp(-\Delta E/kT)$ to temperature-independent metal conductivity.[1–3] The reversibility of the phase transition implies that after the electric field has been removed, the sample returns to its initial semiconducting state. The number of cycles of transitions from the semiconducting to the metal state and back can cover many orders of magnitude, and is called the degree of reversibility.

In the literature there is no common viewpoint on the nature of this phase transition. Its most important characteristic — the transition temperature — has been the subject of particular controversy.[3,4] As a result of filamentation of the current in a strong field, the volume of the metal phase is usually a few cubic micron. It is extremely difficult to make direct measurements of the temperature in such a small volume and it is therefore estimated from indirect measurements.

In Refs. 1 and 2 the phase transition temperature $T_{\rm pt}$ was obtained as ~500–600 K, which was appreciably higher than the temperature of the surrounding medium $T_0=300$ K but much lower than the value of $T_{\rm pt}$ measured directly in solid samples exposed to a field, which was ~1000 K (Ref. 5). Thus, it was noted in Refs. 2 and 4 that equally important factors for a phase transition in a strong field are the Joule heating by the current and the change in the electronic properties of chalcogenide glassy semiconductors in a strong field, which reduce $T_{\rm pt}$ from 1000 K to 500–600 K. According to a different viewpoint, the conductivity phase transition in a field takes place without any heating, i.e., $T_{\rm pt}=T_0$ and is only caused by changes in the electronic microscopic properties of the medium in a strong electric field.[3]

One of the most powerful arguments in support of the $T_{\rm pt}=T_0$ theory is the high reversibility of the phase transition, since it is assumed that a repeated transition from semiconductor to metal and back without any change in the properties of the material can only take place in the absence of any appreciable heating. Here we show that under short-term action small volumes of chalcogenide glassy semiconductors may be repeatedly heated to temperatures considerably in excess of T_m without being damaged. It is thus demonstrated that high reversibility does not imply the absence of any appreciable heating during a conductivity phase transition in a strong field.

For the investigations we used films of $Te_{81}As_4Ge_{15}$ chalcogenide glassy semiconductors with $\Delta E\approx 0.45$ eV and thickness $L=0.15$–0.3 μm, prepared by vacuum deposition on a glass substrate. When films having this composition are heated, a ''glass–crystal'' structural phase transition is observed at the crystallization temperature $T_c\approx 500$ K (Ref. 6). The melting point for this compound is $T_m\approx 650$ K (Ref. 7). The samples were exposed to $\lambda=0.514$ μm optical radiation pulses from an argon laser, of length τ in the range $(0.2\times 10^{-6}$–$1)$ s, focused into a spot having the area $S\approx 20$ μm^2. The results of the irradiation were monitored from the change in the transmission of an optical probe beam ($\lambda=0.63$ μm) focused at the irradiation point, and by an additional examination under a transmission microscope.

The films initially underwent thermal annealing at ~540 K, causing crystallization, which was determined from an approximately tenfold decrease in the transmission of the probe light. Crystallization could also be initiated by illuminating as-grown amorphous film with an argon laser. In Fig. 1, the ''a'' marker indicates the pulse power and length W_a = 5–6 mW and $\tau=50$ μs at which crystallization is initiated (the transmission is reduced by ~30%). For the thermally crystallized films we determined the minimum pulse power W_1 needed for hole burning as a function of τ (curve *1*). Also plotted is the pulse power W_2 which bleached the film twice as a result of partial amorphization, as a function of τ (curve *2*). For films with $L\leqslant 1$ μm the transition takes place in the electric field in 10^{-6} s or less. Thus, attention will mainly be focused on this time interval. We show that the strong dependence of W_1 on τ for short times indicates that the transient heating temperature T_i is considerably higher than T_m (overheating effect) and that T_i increases with decreasing time for points lying within region A in the figure. Each point in this region corresponds to power levels which bleach the crystallized films more than twice $(W(\tau)>W_2(\tau))$ but do not burn through them $(W(\tau)<W_1(\tau))$. For many points in region A the ''darkening-bleaching'' cycle was observed repeatedly.

We first consider how the power should depend on time if the samples were always heated to the same constant temperature which does not depend on τ. The thermal relaxation time τ_r for a film of thickness $L\approx 0.3$ μm is ~0.3 μs (Ref. 2). For $\tau<\tau_r$ heating of the volume LS may be considered to be adiabatic

$$W_\tau=\rho cLS(T-T_0), \tag{1}$$

where ρ is the density and c is the specific heat. If T does not

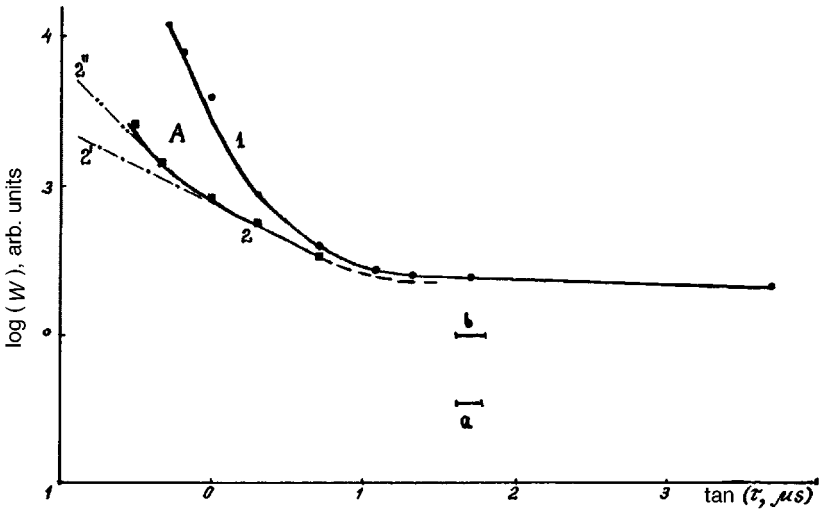

FIG. 1. Pulse power versus pulse length. For explanation see text.

depend on τ, it then follows that $W \sim 1/\tau$. For $\tau \geqslant \tau_r$ the heated volume includes part of the substrate so that the characteristic size of this volume is $l=(D\tau)^{1/2}$, where $D=k/\rho c$ and k is the thermal conductivity. Assuming that the thermal constants of the substrate and the film are similar, and substituting l instead of L in formula (1), we obtain $W \sim 1/\tau^{1/2}$. As τ increases further, equilibrium is established and W ceases to depend on time. This lack of dependence of $W_{1,2}$ on τ is observed for $\tau > 10^{-5}$ s, where the difference between W_1 and W_2 is only 10–20% so that they are difficult to distinguish. Thus, $W_2(\tau)$ is shown schematically for these times by the dashed line. We now estimate the steady-state heating temperature T_s in this region. The power W_a at which crystallization is initiated is ~ 7 times lower than W_1. From this we obtain $W_1/W_a = \Delta T_{s1}/\Delta T_{sa} = 7$, where $\Delta T_{s1,sa} = T_{s1,sa} - T_0$. Under thermal annealing, crystallization is initiated after heating by $\Delta T = 50$ K (Ref. 8). After identifying this heating with ΔT_a we find that $\Delta T_1 = 350$ K, i.e., $T_{s1} = 650$ K. We obtain an upper estimate by equating W_1 and the power W_b (denoted by ''b'') required to darken the fresh film ~ 2.4 times. This darkening was achieved in thermal annealing as a result of heating by ≈ 220 K (Ref. 8). Since $W_1/W_b \approx 2$, it then follows that $\Delta T_1 = 440$ K, i.e., $T_{s1} = 740$ K. Thus, for $\tau > 10$ μs, T_{s1} lies in the range 650–740 K, whose lower limit coincides with T_m. This estimate is supported by the fact that in this range of times, the power W_2 causing bleaching, which is associated with melting followed by partial amorphization, is only 10–20% lower than W_1.

Completely different behavior is observed for $\tau < 10$ μs, where W_1 increases substantially and there is a large difference between W_1 and W_2. We first consider the dependence of W_2. For times ~ 3–0.3 μs this dependence accurately obeys the law $\sim 1/\tau^{1/2}$ which is shown by curve $2'$ for clarity. At times shorter than ~ 0.3 μs a hint of a transition to the dependence $\sim 1/\tau$ (curve $2''$) is observed. Thus, for $\tau < 3$ μs the W_2 dependence is determined by heating to constant temperature. The fact that W_1 is much higher than W_2 for these times indicates that the temperature corresponding to the power W_1 increases substantially with decreasing time. We estimate this temperature for $\tau \approx 0.4$ μs assuming that the heating corresponding to W_2 is $\Delta T_{i2} \sim 350$ K. Then, from the equality of W_1/W_2 and $\Delta T_{i1}/\Delta T_{i2}$, we find that ΔT_{i1} is ~ 2250 K. Thus, we found that whereas for large τ the temperatures T_1 and T_2 were similar and were close to T_m, for small τ the temperature T_1 is considerably higher than T_2, reaching at least 2250 K at the end of the time interval. Thus, in the entire range $W_1 > W > W_2$ corresponding to region A in Fig. 1, the films withstand repeated heating to temperatures appreciably higher than the melting point without being damaged.

Thus, these results indicate that a reversible semiconductor–metal phase transition may take place repeatedly in a strong field at temperatures of 500–600 K determined in Refs. 1 and 2 since films of chalcogenide glassy semiconductors can withstand much greater heating without being damaged.

These results are also of practical importance since they show that the known advantages of optical and electrical recording and rerecording of information using short pulses are possibly related to the existence of a wide power range for short times (region A) whereas this range is appreciably narrower for long times.

The authors would like to thank V. I. Kochenev for assistance with the measurements, M. A. Tagirdzhanov for useful discussions, and the Russian Fund for Fundamental Research for financial assistance (Grant No. 97-02-18079).

[1] P. J. Walsh, R. Vogel, and E. J. Evans, Phys. Rev. **178**, 1274 (1969).
[2] B. T. Kolomiets, É. A Lebedev, and K. D. Tséndin, Fiz. Tekh. Poluprovodn. **15**, 304 (1981) [Sov. Phys. Semicond. **15**, 175 (1981)].
[3] A. Meden and M. Sho, *Physics and Applications of Amorphous Semiconductors* [Russ. transl., Mir, Moscow, 1991].
[4] É. A Lebedev, and K. D. Tséndin, *Electronic Effects in Chalcogenide Glassy Semiconductors*, edited by K. D. Tséndin [in Russian], Nauka, St. Petersburg, (1996).
[5] D. L. Thomas and J. C. Male, J Non-Cryst. Solids **8–10**, 522 (1972).
[6] A. L. Glazov, S. B. Gurevich, N. N. Il'yashenko *et al.*, Pis'ma Zh. Éksp. Teor. Fiz. **12**, 138 (1986) [*sic*].
[7] H. Fritzsche and S. R. Ovshinsky, J. Non-Cryst. Solids **2**, 148 (1970).
[8] N. K. Kiselëva, V. I. Kochenov, and É. A. Lebedev, Fiz. Tverd. Tela (Leningrad) **30**, 1965 (1988) [Sov. Phys. Solid State **30**, 1135 (1988)].

Translated by R. M. Durham

Oscillatory instability of a highly charged droplet

D. F. Belonozhko

Yaroslaval State University
(Submitted June 10, 1997)
Pis'ma Zh. Tekh. Fiz. **23**, 18–23 (November 26, 1997)

A dispersion equation is obtained for the capillary oscillations of a charged viscous droplet of electrically conducting liquid in a conducting medium allowing for the charge relaxation effect and it is shown that this droplet may undergo oscillatory instability. © *1997 American Institute of Physics.* [S1063-7850(97)02111-3]

Studies of the laws governing the buildup of instability of highly charged droplets are of interest for numerous applications in physics, geophysics, and technology.[1,2] The aperiodically occurring Rayleigh instability of a droplet relative to its own charge is well known and has been studied in detail.[1,2] The oscillatory instability of a highly charged droplet has been little studied although indirect experimental evidence of its possible existence has been reported.[3,4]

We shall consider a system consisting of two immiscible incompressible liquids having the densities $\rho^{(1)}$ and $\rho^{(2)}$ and the kinematic viscosities $\nu^{(1)}$ and $\nu^{(2)}$. In the absence of gravitational forces, the internal liquid, identified by the superscript (1), has the form of a spherical droplet of radius R as a result of the action of surface tension forces whose coefficient is denoted by γ. At the interface between the two liquids there is a charge Q which is kept constant by means of a current flowing between a point electrode at the center of the droplet and a concentric spherical electrode located in the external medium at a very large distance from the interface. The influence of the electrodes on the flow of the media will be neglected in these model calculations. We assume that the liquid in the droplet has the conductivity σ_1 and permittivity ε_1, and the medium is conducting with the characteristics σ_2 and ε_2. We shall seek the dispersion equation for the capillary motion in the system using a method described in Ref. 5.

The system of hydrodynamic equations describing the liquid motion inside the droplet and in the surrounding medium, linearized near the equilibrium spherical state, has the form:

$$\frac{\partial \mathbf{u}^{(j)}}{\partial t} = -\frac{1}{\rho^{(j)}}\nabla p^{(j)} + \nu^{(j)}\Delta \mathbf{u}^{(j)}, \quad \operatorname{div}\mathbf{u}^{(j)} = 0, \quad j = 1;\ 2,$$

$$r = R: \quad u_\theta^{(1)} = u_\theta^{(2)}, \quad u_\varphi^{(1)} = u_\varphi^{(2)}, \quad u_r^{(1)} = u_r^{(2)} = \frac{\partial \xi}{\partial t},$$

$$\Pi_{1\theta} + \rho^{(1)}\nu^{(1)}\left[\frac{1}{r}\frac{\partial u_r^{(1)}}{\partial \theta} + \frac{\partial u_\theta^{(1)}}{\partial r} - \frac{1}{r}u_\theta^{(1)}\right] = \Pi_{2\theta} + \rho^{(2)}\nu^{(2)}\left[\frac{1}{r}\frac{\partial u_r^{(2)}}{\partial \theta} + \frac{\partial u_\theta^{(2)}}{\partial r} - \frac{1}{r}u_\theta^{(2)}\right],$$

$$\Pi_{1\varphi} + \rho^{(1)}\nu^{(1)}\left[\frac{1}{r\sin\theta}\frac{\partial u_r^{(1)}}{\partial \varphi} + \frac{\partial u_\varphi^{(1)}}{\partial r} - \frac{1}{r}u_\varphi^{(1)}\right] = \Pi_{2\varphi} + \rho^{(2)}\nu^{(2)}\left[\frac{1}{r\sin\theta}\frac{\partial u_r^{(2)}}{\partial \varphi} + \frac{\partial u_\varphi^{(2)}}{\partial r} - \frac{1}{r}u_\varphi^{(2)}\right],$$

$$-p^{(1)} + 2\rho^{(1)}\nu^{(1)}\frac{\partial u_r^{(1)}}{\partial r} + p_\gamma - p_E = -p^{(2)} + 2\rho^{(2)}\nu^{(2)}\frac{\partial u_r^{(2)}}{\partial r},$$

$$\int_\Omega \xi(\theta,\varphi,t)\,d\Omega = 0, \qquad \int_\Omega \xi(\theta,\varphi,t)\,\mathbf{e}_r\,d\Omega = 0.$$

Here ξ, $\mathbf{u}$, and p denote perturbations of the interface profile, the velocity field, and the pressure field, respectively, and p_γ is the perturbation of the pressure of the surface tension forces.[6]

$$p_\gamma(\xi) = -\frac{\gamma}{R^2}(2 + \Delta_\Omega)\xi,$$

p_E is the perturbation of the electric field pressure P_E caused by the interface perturbation ξ (Ref. 7), $\Pi_{j\theta}$ and $\Pi_{i\varphi}$ are the electrical components of the tangential component of the stress tensor caused by the currents of charge undergoing redistribution as a result of the deformation of the droplet surface

$$P_E = \frac{1}{8\pi}[\varepsilon_1 E_{2n}^2 - \varepsilon_2 E_{1n}^2] + (\varepsilon_2 - \varepsilon_1)\frac{E_{2\tau}}{8\pi},$$

$$\Pi_{j\tau} = \frac{\varepsilon_j}{4\pi}E_{jn}E_{j\tau}, \quad j = 1;2.$$

E_{jn} and $E_{j\tau}$, $j = 1;\ 2$ are the normal and tangential components of the electric field strength vector, $\mathbf{n}$, $\boldsymbol{\tau} \equiv \mathbf{e}_\theta$, and $\mathbf{e}_\varphi$ are the unit vectors of the normal and two tangents to the surface of the droplet.

The required dispersion equation is obtained in the form

$$\det a_{ij} = 0, \quad 1 \leqslant i,j \leqslant 5, \tag{1}$$

$$a_{11} = 1, \quad a_{12} = -1, \quad a_{13} = f_m^{(1)}(x_1) + (m+1),$$

$$a_{14} = f_m^{(2)}(x_2) + m, \quad a_{15} = 0,$$

$$a_{21}=2(m-1)\rho^{(1)}\nu^{(1)}+\frac{Q^2}{4\pi}\frac{(\sigma_2-\sigma_1)}{g_2(\varepsilon_j,\sigma_j)}\times\frac{(m(m+1))^2}{Z_m}(1-R_0^{(2m+1)}),$$

$$a_{22}=2(m+2)\rho^{(2)}\nu^{(2)},$$

$$a_{23}=\rho^{(1)}\nu^{(1)}[-2f_m^{(1)}(x_1)+x_1^2+2(m-1)(m+1)]+\frac{Q^2}{4\pi}\frac{(\sigma_2-\sigma_1)}{g_2(\varepsilon_j,\sigma_j)}\frac{(m(m+1))^2}{Z_m}\times(1-R_0^{(2m+1)})\{f_m^{(1)}(x_1)+(m+1)\},$$

$$a_{24}=-\rho^{(2)}\nu^{(2)}[2f_m^{(2)}(x_2)+x_2^2+2m(m+2)],$$

$$a_{25}=\frac{Q^2(\sigma_2-\sigma_1)}{4\pi(g_2(\varepsilon_j,\sigma_j))^2}\frac{m(m+1)}{Z_m}g_3(\mu_j,\sigma_j),$$

$$a_{31}=m,\quad a_{32}=(m+1),\quad a_{33}=m(m+1),$$

$$a_{34}=-m(m+1),\quad a_{35}=0,\quad a_{41}=m,$$

$$a_{42}=0,\quad a_{43}=m(m+1),\quad a_{44}=0,\quad a_{45}=-S,$$

$$a_{51}=\rho^{(1)}[S+2m(m-1)\nu^{(1)}]-\frac{Q^2}{4\pi}\frac{1}{g_2(\varepsilon_j,\sigma_j)}\times\frac{m(m+1)}{Z_m}g_5(\varepsilon_j,\sigma_j),$$

$$a_{52}=-\rho^{(2)}S-2(m+1)(m+2)\rho^{(2)}\nu^{(2)},$$

$$a_{53}=2\rho^{(1)}\nu^{(1)}m(m+1)[f_m^{(1)}(x_1)+(m-1)]-\frac{Q^2}{4\pi}\frac{1}{g_2(\varepsilon_j,\sigma_j)}\frac{m(m+1)}{Z_m}g_5(\varepsilon_j,\sigma_j)\times\{f_m^{(1)}(x_1)+(m+1)\},$$

$$a_{54}=\rho^{(2)}\nu^{(2)}2m(m+1)[f_m^{(2)}(x_2)+(m+2)],$$

$$a_{55}=(m-1)(m+2)+\frac{Q^2}{4\pi}\frac{1}{(g_2(\varepsilon_j,\sigma_j))^2}\times\frac{g_4(\mu_j,\varepsilon_j,\sigma_j,b)}{Z_m},$$

$$f_m^{(1)}(x_1)\equiv x_1\frac{i_{m+1}(x_1)}{i_m(x_1)},\quad f_m^{(2)}(x_2)\equiv x_2\frac{k_{m-1}(x_2)}{k_m(x_2)},$$

$$\lambda_j\equiv S\varepsilon_j+4\pi\sigma_j,\quad \mu_j\equiv\lambda_j+m(m+1)D_s\varepsilon_j,$$

$$Q\equiv 4\pi\varkappa_0,$$

$$d_1(y_j)\equiv y_1m+y_2(m+1)+(y_1-y_2)(m+1)R_0^{(2m+1)},$$

$$y_j=\mu_j,\varepsilon_j,\lambda_j,$$

$$Z_m=d_1(\lambda_j)+m(m+1)[D_sd_1(\varepsilon_j)+Qb(1-R_0^{(2m+1)})],$$

$$g_1\equiv(2\lambda_1-\lambda_2)\sigma_2-\lambda_2\sigma_1,\quad g_2\equiv\varepsilon_2\sigma_1-\varepsilon_1\sigma_2;$$

$$h_1\equiv\varepsilon_1\sigma_2-\varepsilon_2\sigma_2-g_2,$$

$$\eta_1\equiv g_1(\lambda_j,\sigma_j)+m(m+1)D_sh_1,$$

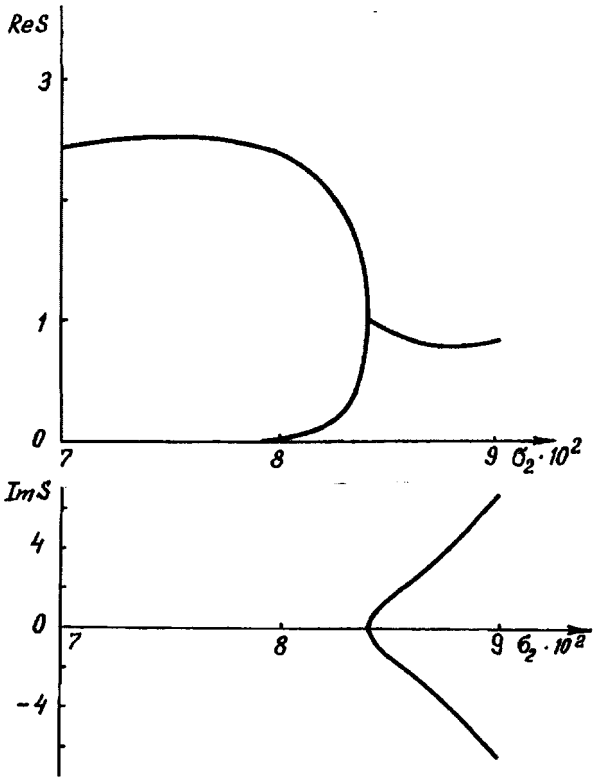

FIG. 1. Dependences of the real $\mathrm{Re}\,S=\mathrm{Re}\,S(\sigma_2)$ and imaginary $\mathrm{Im}\,S=\mathrm{Im}\,S(\sigma_2)$ parts of the complex frequency on the conductivity of the external medium σ_2 for $\sigma_1=10^4$, $m=2$, $\nu_1=\nu_2=0.002$, $\rho_1=1$, $\rho_2=10^{-3}$, $\varepsilon_1=50$, $\varepsilon_2=5$, $b=10^{-2}$, $D_s=10^{-5}$, and $W=22$.

$$g_3\equiv[((m+2)\lambda_1+m\lambda_2)\sigma_2-\lambda_2\sigma_1]+[((m-1)\lambda_1-m\lambda_2)\sigma_2+\lambda_2\sigma_1]R_0^{(2m+1)},$$

$$h_3\equiv h_1(1-R_0^{(2m+1)})+\sigma_2d_1(\varepsilon_j),$$

$$\eta_3\equiv g_3+m(m+1)D_s\,h_3,$$

$$g_4\equiv\varepsilon_2\sigma_1\{(m+1)\eta_3-(m-1)\sigma_1\times[d_1(\mu_j)+m(m+1)Qb(1-R_0^{(2m+1)})]\}+\varepsilon_1\sigma_2\{[m+(m+1)R_0^{(2m+1)}]\eta_1+2\sigma_2d_1(\mu_j)-\sigma_2m(m+1)Qb[(m-2)+(m+3)R_0^{(2m+1)}]\},$$

$$g_5\equiv[(m+1)\varepsilon_2\sigma_1+m\varepsilon_1\sigma_1]-(m+1)g_2R_0^{(2m+1)},$$

$$x_j=\sqrt{\frac{S}{\nu_j}};$$

$i_m(x)$ and $k_m(x)$ are modified Bessel functions of the first and third kinds, respectively.

The results of the numerical calculations using Eq. (1) are plotted in Fig. 1 as dependences of the real and imaginary parts of the complex frequency on the conductivity of the external medium σ_2. It is easy to see that for a Rayleigh-supercritical droplet charge, there is a region of σ_2 values in which oscillatory instability exists.

To conclude, a highly charged droplet of electrically conducting liquid in a conducting medium may undergo oscillatory instability caused by a phase advance (as a result of

redistribution of the charge in the presence of capillary oscillations) of the electric field pressure compared with the capillary waves.

[1] A. I. Grigor'ev and S. O. Shiryaeva, Zh. Tekh. Fiz. **61**(3), 19 (1991) [Sov. Phys. Tech. Phys. **36**, 258 (1991)].
[2] S. O. Shiryaeva, M. I. Munichev, and A. I. Grigor'ev, Zh. Tekh. Fiz. **66**(7), 1 (1996) [Tech. Phys. **41**, 635 (1996)].
[3] J. J. Billings and D. G. Holland, J. Geophys. Res. **74**, 6881 (1969).
[4] J. Zeleny, Phys. Rev. **3**, 69 (1914).
[5] S. O. Shiryaeva, A. É Lazaryants *et al.*, *Method of Scalarizing Vector Boundary-Value Problems*, Preprint No. 27 [in Russian], Institute of Mathematics, Russian Academy of Sciences, Yaroslavl (1994).
[6] V. G. Levich, *Physicochemical Hydrodynamics* [in Russian], Fizmatgiz, Moscow (1959).
[7] L. D. Landau and E. M. Lifshitz, *Electrodynamics of Continuous Media*, transl., of 1st Russ. ed. (Pergamon Press, Oxford, 1960) [Russ. original, later ed., Nauka, Moscow, 1982].

Translated by R. M. Durham

Traveling vortex breakdown

S. V. Alekseenko and S. I. Shtork

Institute of Heat Physics, Siberian Branch of the Russian Academy of Sciences, Novosibirsk
(Submitted June 3, 1997)
Pis'ma Zh. Tekh. Fiz. **23**, 24–28 (November 26, 1997)

A new type of propagating perturbations on a vortex filament — traveling vortex breakdown — has been observed experimentally. A method of controlled external action on a vortex flow with known parameters is used. Data are obtained on the absolute propagation velocity of the perturbations as a function of the conditions in the vortex chamber, which determine the vortex characteristics. [S1063-7850(97)02211-8]

Vortex breakdown plays a fundamental role in the dynamics of extended vortices. Extended vortices are observed at the microscale level (vortex filaments in superfluid helium, vortex structure elements in turbulence) and at the macroscale level (twisted flow in a vortex chamber, sandstorms and tornados). The most dramatic stage in the evolution of vortices is their sudden collapse — known as vortex breakdown. A fairly comprehensive bibliography on this problem is now available (see the review presented in Ref. 1). Vortex breakdown was first observed in flow around a delta wing at a large angle of attack. However, most studies are concerned with breakdown in a weakly expanding tube which allows the experimental conditions to be strictly monitored. Vortex breakdown leads to a fundamental rearrangement of the flow structure and the onset of turbulence. In particular, the formation and breakdown of vortex structures is found in various scenarios for the evolution of turbulence in detached and boundary-layer flows.[2] Vortex breakdown and its unpredictability is one of the main factors lowering the efficiency and therefore holding back the development of vortex technologies.[3]

A fairly large number of theoretical models have been

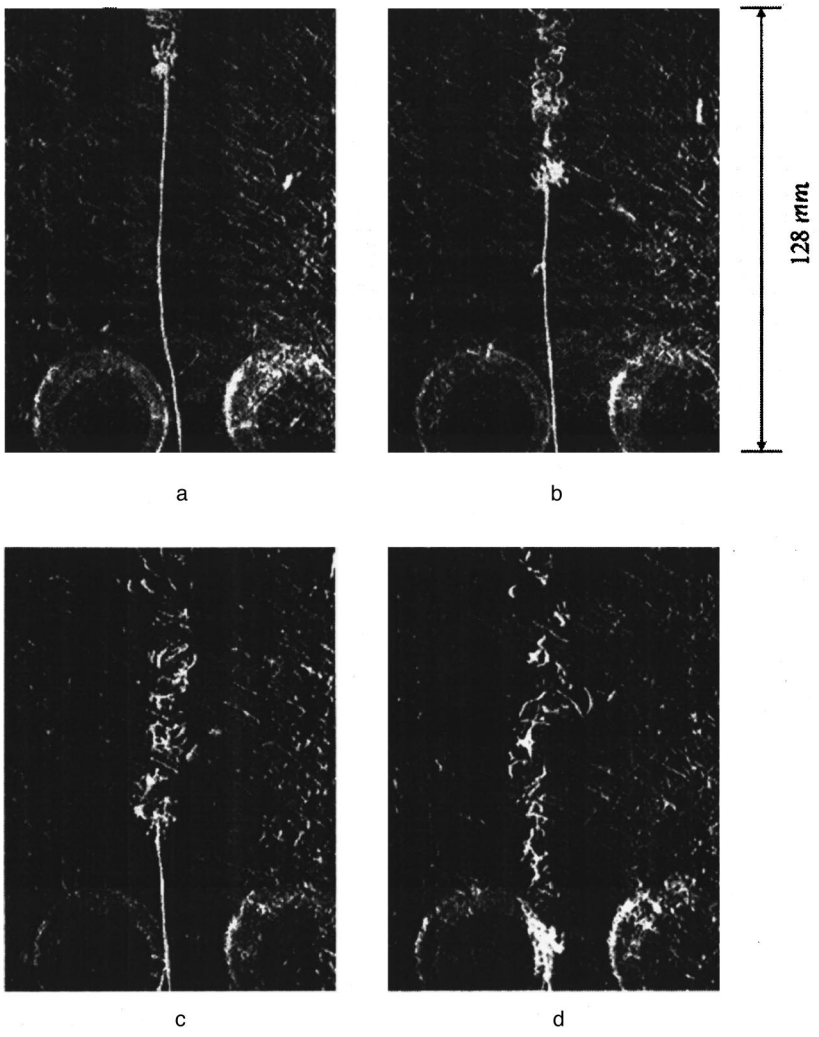

FIG. 1. Photo sequence showing forced traveling vortex breakdown. The time interval between frames is 80 ms. The vortex flow moves upward. The vortex core was perturbed at a distance of 50 mm from the upper edge of the frame: $Q=1.3$ l/s, $S=3.5$.

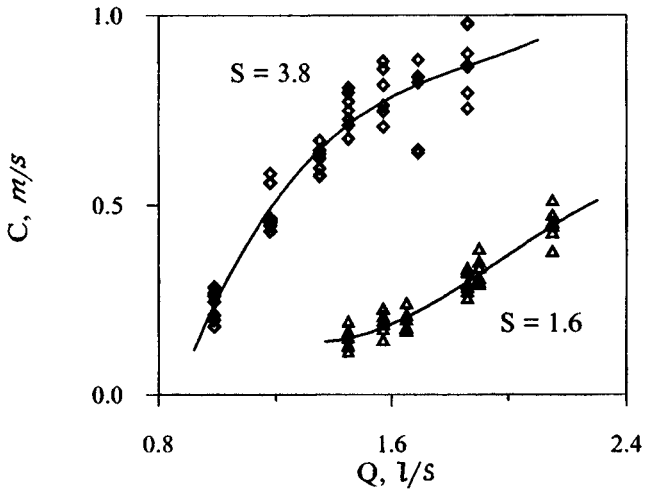

FIG. 2. Absolute propagation velocity of traveling breakdown as a function of conditions in vortex chamber.

proposed for vortex breakdown.[1] However, there are no adequate theories which can sufficiently accurately predict the instant, position, and type of vortex breakdown. Some of the promising approaches must include the wave theories.[1,4] It is hypothesized that flow instability or an external influence may produce such an intense solitary wave (such as a Korteweg-de-Vries soliton) that return motion occurs locally, leading to breakdown or rearrangement of the flow. However, these theories are extremely difficult to check because most of the experiments described in the literature have a spatially fixed breakdown position. Here, we describe the first experimental observations of traveling vortex breakdown generated under controlled conditions. These results shed light on new properties of the breakdown phenomenon and may be used as the basis to develop a wave approach since this offers the possibility of studying the entire breakdown formation process in space and time. The most important factor is that the breakdown effect can be controlled by altering the conditions used to generate the initial perturbations and the parameters of the vortex filament in the vortex chamber.

The experiments were carried out using a hydraulic vortex chamber having a 188×188 mm square cross section and a height up to 630 mm (see Ref. 5). It was shown in experiments with cylindrical inserts, that the shape of the cross section did not play a fundamental role when studying vortex filaments. Twelve rotatable rectangular nozzles whose axes were directed along the tangent to a certain circle were used to supply liquid and produce twisted flow. The characteristics of the vortex motion (the circulation, the velocity along the axis of the vortex, and the vortex diameter) could be varied fairly easily by changing the design twist parameter (the angle of rotation of the nozzles), the flow rate Q, and the diameter of the exit aperture in the diaphragm. The parameters of the vortex core were determined by measuring the velocity profiles near the vortex axis along particle tracks and by measuring the static pressure at the end wall. The experimental points lie on empirical curves which accurately describe the profiles of the tangential V and axial W components of the velocity in canonical vortex systems:[6,7]

$$V=A[1-\exp(-Br^2)]/r,$$

$$W=W_1+W_2\exp(-Br^2),$$

where A, B, W_1, and W_2 are empirical coefficients, and r is the radial distance from the vortex axis.

The characteristic diameter of the vortices at which perturbations were initiated did not exceed 4 mm and their characteristic length was greater than 400 mm. Since the transverse width of the chamber is 188 mm, it follows that the vortex in the chamber may be interpreted as an isolated vortex filament. The vorticity and axial motion are concentrated in the thin core of this filament, i.e., the axial and tangential velocities are considerably higher than the velocities in the surrounding medium.

A flow perturbation was created at a distance of 80 mm from the exit aperture of the diaphragm by passing a 6 mm diameter rod through the vortex core. This method can influence the vortex filament without significantly perturbing the average flow. As a result, a breakdown region was formed, which propagated upstream, forming an almost cylindrical wake, and the surrounding liquid remained unperturbed up to the breakdown point. The flow was visualized by using small air bubbles. As a result of the sharp pressure drop on the axis of the concentrated vortex, the bubbles collect on the axis, forming an air filament which effectively visualizes the vortex axis. The characteristic diameter of the breakdown region was of the order of 10 mm. The visual observations were accompanied by video recording (Fig. 1). The video images were decoded and processed on a personal computer.

Experimental dependences of the breakdown velocity on the twist parameter S and the Reynolds number (or flow rate Q) of the vortex flow (Fig. 2) were obtained by analyzing the video recording of the traveling breakdown. The twist parameter was determined as $S=(md)/(nf)$, where $m=188$ mm is the transverse width of the chamber, d is the diameter of an arbitrary circle along the tangent to which the axes of the vortex-generating nozzles are directed, $n=12$ is the number of nozzles, and $f=14\times23$ mm^2 is the area of a single nozzle. It can be seen from the graph that the perturbation velocity increases as the twist and the flow rate increase.

Investigations of the local structure of the traveling breakdown are required to identify the mechanisms responsible for these effects and compare them with wave theories of breakdown. Such investigations constitute a separate and fairly complex hydrodynamic problem because of their three-dimensional nature and transient conditions.

This work was supported by the Russian Fund for Fundamental Research (Grant No. 96-01-01667).

[1] M. P. Esculier, Prog. Aerospace Sci. **25**, 189 (1988).
[2] Yu. N. Grigor'ev, Russ. J. Eng. Thermophys. **4**(2), 197 (1994).
[3] S. V. Alekseenko and V. L. Okulov, Teplofiz. Aeromekh. **3**(2), 101, 1996).
[4] J. D. Randall and S. Leibovich, J. Fluid. Mech. **53**, 495 (1973).
[5] S. V. Alekseenko and S. I. Shtork, Russ. J. Eng. Thermophys. **2**(4), 231 (1992).
[6] A. K. Garg and S. Leibovich, Phys. Fluids **22**, 2053 (1979).
[7] S. V. Alekseenko and S. I. Shtork, Pis'ma Zh. Éksp. Teor. Fiz. **59**, 746 (1994) [JETP Lett. **59**, 775 (1994)].

Translated by R. M. Durham

Scenario for the establishment of an electron beam ''squeezed state'' in a magnetically insulated vircator

A. E. Dubinov

Russian Federal Nuclear Center — All-Russian Scientific Research Institute of Experimental Physics, Sarov (Arzamas-16)

(Submitted July 29, 1996)
Pis'ma Zh. Tekh. Fiz. **23**, 29–33 (November 26, 1997)

A 2.5-dimensional particle-in-cell code was used to simulate different scenarios for the establishment of an electron beam ''squeezed state'' in a magnetically insulated vircator. Vircators with and without anode foils were compared. It was found that the squeezed state is established in both cases but the dynamics of establishment differ. © *1997 American Institute of Physics.* [S1063-7850(97)02311-2]

Generators of microwave radiation with a virtual cathode (vircators) are attracting increasing attention among researchers.[1,2] Among these devices, particular mention should be made of vircators with magnetically insulated diodes in which a virtual cathode is formed in a drift tube of diameter much greater than the anode diameter.[3] Usually these systems do not have a transverse anode foil so that they can be called foilless vircators.

The dynamics of the formation of a virtual cathode in a foilless magnetically insulated vircator was simulated in Ref. 4. It was shown that a so-called ''squeezed state,'' characterized by a low velocity and high electron density, is established in the beam, and the front of this squeezed state moves together with the virtual cathode in the direction opposite to injection and stops near the cathode in the anode tube.

In order to explain this phenomenon, the authors of Ref. 4 analyzed a model based on the balance of the pressure forces in the cross sections on different sides of the step — a transient anode tube in the drift tube.

However, this model disregards the conditions at the step itself, where a thin electron-transparent foil or, say, a thin plasma layer, may or may not exist. It is natural to expect that different conditions at the step may lead to different scenarios for the formation of the virtual cathode (significant differences in the electron dynamics with and without an anode foil have been observed in an ordinary vircator, see Ref. 5).

In this context, our aim here is to continue the study of the squeezed state in a magnetically insulated vircator started in Ref. 4, and particularly to determine whether the same or different scenario for the establishment of the squeezed state may be achieved under different conditions at the step.

For this purpose we used the KARAT computer modeling package[6] which uses a 2.5 dimensional particle-in-cell (PIC) code and was kindly supplied by V. P. Tarakanov.

The region modeled and the required dimensions are shown in Fig. 1.

It was assumed that a uniform longitudinal magnetic field of 50 kG was applied to the entire system and a 500 kV voltage pulse was applied to the diode gap. Two versions, with and without a foil positioned at the diameter step, were compared.

It was found that in both cases, the amplitude of the cathode current was approximately 17 kA and a squeezed state was formed.

The evolution of the squeezed state can be conveniently studied using instantaneous phase portraits of the beams in the coordinates $(v_z; z)$. Phase portraits at various times (1, 2, and 3 ns) are given in Fig. 2a for a vircator with a foil and in Fig. 2b for a foilless vircator. An analysis reveals that in the vircator with the anode foil, the squeezed-state region of the beam develops more slowly than in the foilless vircator, leaving behind a ''phase bubble'' in the foil region. The existence of this bubble can be explained by the fact that the potential near the step is forced to remain equal to the anode potential.

The nature of the virtual cathode motion and also the motion of the front of the squeezed state were determined.

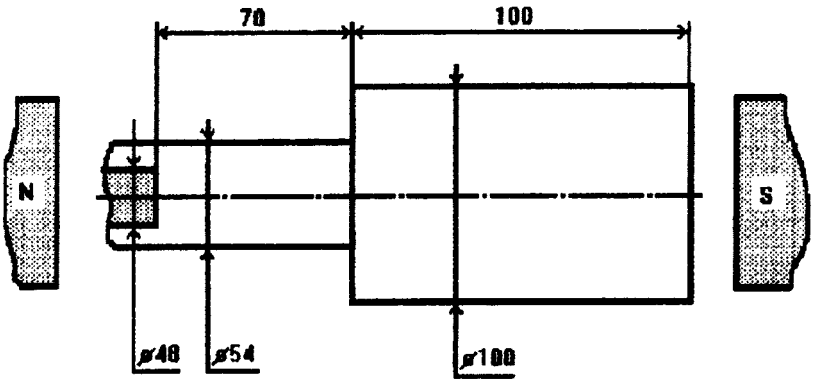

FIG. 1. Schematic of modeled region (all dimensions are in millimeter, not to scale).

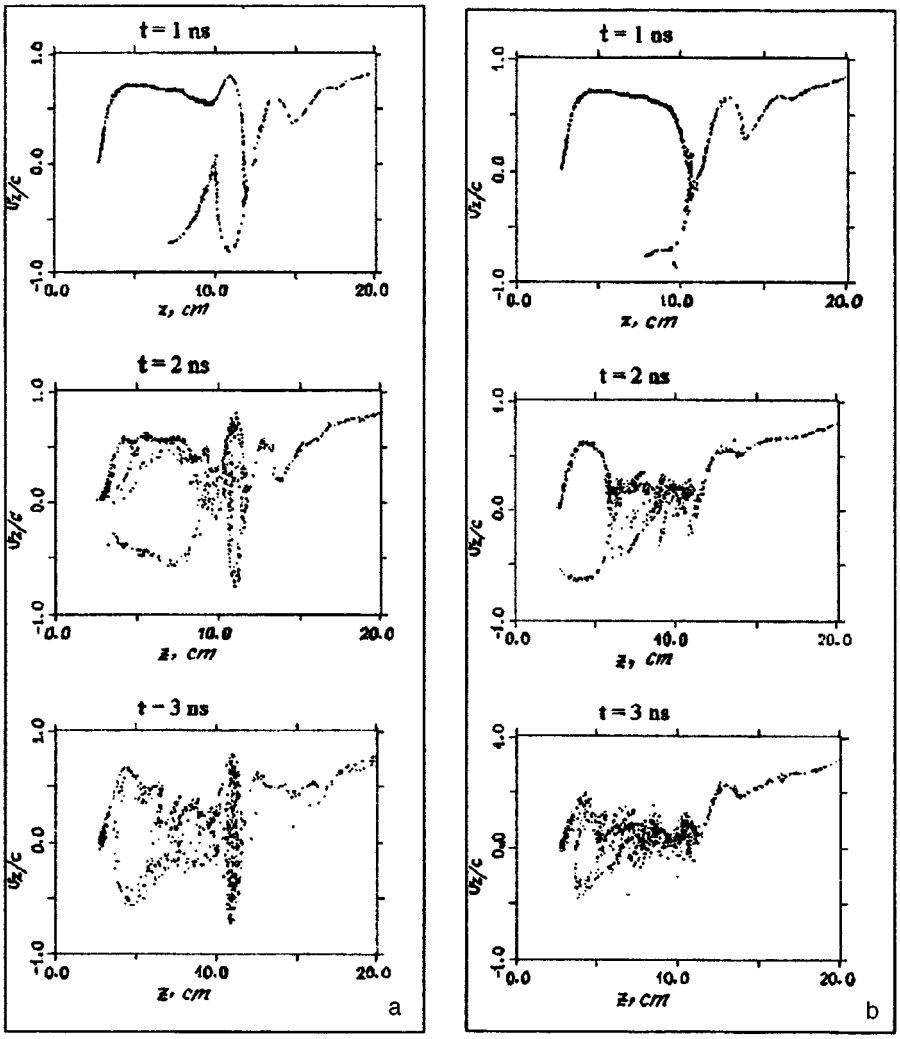

FIG. 2. Instantaneous phase portraits of the beam in the plane (v_z; z): a — for a vircator with an anode foil, b — for a foilless vircator.

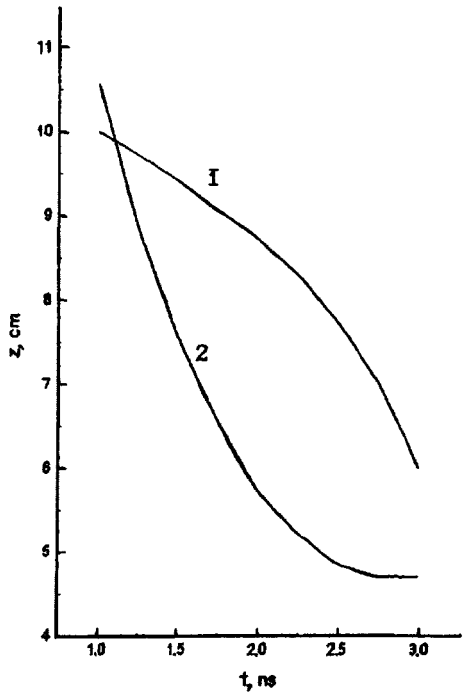

FIG. 3. Laws of motion of virtual cathode (and front of squeezed state): *1* — for vircator with an anode foil, *2* — for foilless vircator.

The laws governing their motion for both cases, calculated with a time step of 250 ps, are plotted in Fig. 3. The opposite curvature of these graphs indicates that the pressure forces at the front of the squeezed state differ in the two cases (if it is meaningful to talk of a force acting on phase formations, such as the virtual cathode and the front of the squeezed state).

To conclude, the squeezed state in a magnetically insulated electron beam is established regardless of the conditions at the step but these conditions strongly influence its establishment scenario.

The author would like to thank V. P. Tarakanov for consultations on the use of the KARAT code.

[1] B. V. Alyokhin, A. E. Dubinov, V. D. Selemir *et al.*, IEEE Trans. Plasma Sci. **22**, 945 (1994).
[2] A. E. Dubinov and V. D. Selemir, Zarub. Radioelektron. No. 4, 54 (1995).
[3] A. G. Zherlitsyn, S. I. Kuznetsov, and G. V. Mel'nikov, Zh. Tekh. Fiz. **56**, 1384 (1986) [Sov. Phys. Tech. Phys. **31**, 814 (1986)].
[4] A. M. Ignatov and V. P. Tarakanov, Phys. Plasmas **1**, 741 (1994).
[5] V. D. Grigor'ev and A. E. Dubinov, Pis'ma Zh. Tekh. Fiz. **22**(7), 70 (1996) [Tech. Phys. Lett. **22**, 299 (1996)].
[6] V. P. Tarakanov, *User's Manual for Code KARAT*, Berkley Research Associates, Springfield, VA (1992).

Translated by R. M. Durham

Inverted domains in lithium niobate

A. V. Golenishchev-Kutuzov and R. I. Kalimullin

Moscow Power Institute (Kazan Branch)
(Submitted May 6, 1997)
Pis'ma Zh. Tekh. Fiz. **23**, 34–38 (November 26, 1997)

The formation of a periodic structure of inverted domains under the simultaneous action of uniform laser irradiation and a standing surface acoustic wave has been investigated. Mechanisms for the formation of an acoustically induced domain structure are discussed. © *1997 American Institute of Physics.* [S1063-7850(97)02411-7]

The possible formation of periodic structures with a variable gradient or, especially, with a variable-direction electric field in ferroelectrics has long formed the subject of experimental investigations and theoretical models.[1] A comparison between the various models suggests that domains are created as a result of the formation of layers of impurity ions of different valence and therefore of different electric charge. These layers of ions form electric fields whose directions are inverted relative to each other.

In order to check out this hypothesis, we investigated the formation of inverted domain structures in the piezoelectric layer by a standing acoustic wave. Since the redistribution of electrons by fields of standing surface[2] and bulk acoustic waves[3] has already been observed in lithium niobate and the photo-induced electric field gradients are known, these crystals were selected for our investigations. Samples of lithium niobate single crystals cut in the form of *x*-cut wafers, measuring $1\times15\times25$ nm (XYZ) and containing between 10^{-1} and 10^{-3} at.% iron ions, were annealed in helium at 600° C for 1.5 h. It was observed using ESR, acoustic ESR, and optical spectroscopy, that up to 30% of the iron ions had been transferred to the divalent state after annealing. Standing surface acoustic waves were excited in the 30–35 MHz frequency range along the Z axis of the sample using two deposited interdigital transducers. The YZ surface was irradiated by 0.53 μm and 0.63 μm laser beams, expanded by a collimator, at intensities between 50 and 500 $\mathrm{mW\cdot cm^{-2}}$. The simultaneous acoustic and optical action on the sample was varied between a few seconds and 30 min with the samples thermostatically controlled in the temperature range 20–160°C.

It is fairly difficult to identify domains with inverted polarization. The etching method normally used for these purposes partially destroys the surface layer, as well as presenting experimental difficulties. In Ref. 4 we only reliably identified spatial modulation of the refractive index (δn) by a piezoelectric field of surface acoustic waves. In our view, more convincing evidence of polarization reversal was obtained in subsequent experiments which are considered in the present paper.

It is known[5] that for neighboring 180° domains only odd tensors describing some physical properties, such as the piezoelectric (d_{ijk}) and electrooptic (r_{ijk}) tensors, will have different signs. Thus, when an electric field is applied to the crystal, the birefringence tensor will be quasiperiodically modulated as a result of the electrooptic effect, which is equivalent to a periodic change in the sign of the refractive index. This principle is used as the basis for an interferometric method of identifying antiparallel domains, which was successfully used for lithium niobate in Refs. 6 and 7.

We used a similar method to determine the direction of the domains. A sample on whose surface an inverted domain structure had previously been formed was placed in one branch of a Mach–Zehnder interferometer (Fig. 1). An electric field E was applied parallel to the Z axis using electrodes deposited on the XZ surface near the domain boundaries. In this experimental geometry the change in phase for an optical beam passing through the sample along the Y axis as a function of E has the form[5]

$$\varphi=-\frac{\pi LV}{\lambda d}z_{33}n_e^3\frac{(E\cdot P)}{|E\cdot P|},$$

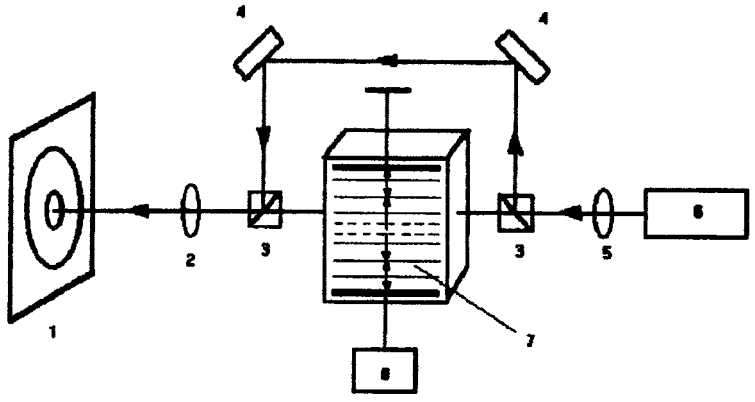

FIG. 1. Schematic of apparatus: *1* — screen, *2, 5* — lenses, *3* — beam splitters, *4* — mirrors, *6* — measuring laser, *7* — inverted domain structure, and *8* — static electric field source.

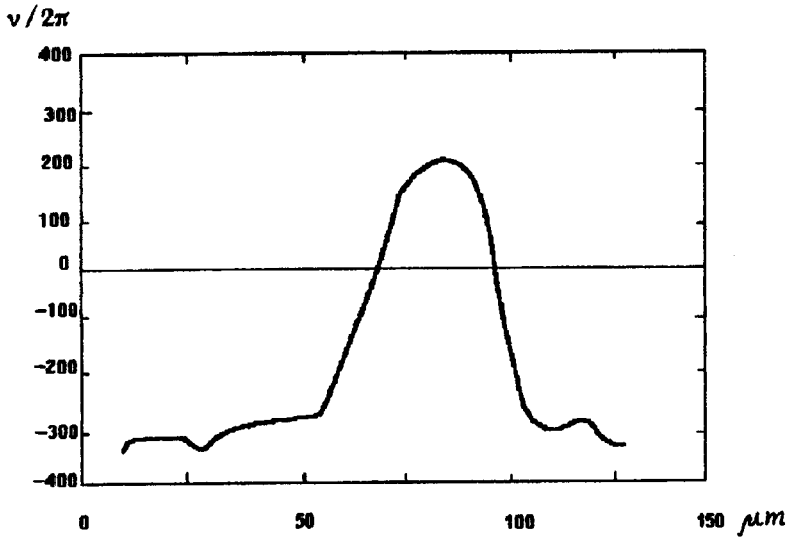

FIG. 2. Phase of applied voltage versus position of scanning optical beam.

where P is the polarization vector, L is the optical path length, and V is the voltage applied to the sample across the gap d. When the field E is parallel to the polarization P, the change in phase will decrease with increasing field E and the interference rings will expand. When E and P are antiparallel, the phase φ will increase and the rings will shift with increasing field E.

This structural change in the behavior of the interference rings was observed by scanning along the XZ surface in the region of formation of the domain structure using a focused ($\phi \approx 20$ μm) low-power helium-neon laser beam. Expansion and shrinkage of the interference rings as the beam moved from one domain to another in fields corresponding to rotation of the phase between 0 and 180° was only observed experimentally in the temperature range 120–160° C and when the relative amplitude of the acoustic deformation of the surface acoustic waves was less than 10^{-4} (Fig. 2). At $T<120$°C the phase change in the electric field had the same sign over the entire scanning cross section. Thus, our interferometric results are completely consistent with the data presented in Ref. 4.

A second set of evidence to support the formation of an inverted domain structure in an acoustic field is provided by the observation of reflection of surface acoustic waves from domains. We investigated the propagation of surface acoustic waves excited and detected by wide-band transducers. It was established that the induced structure possesses resonant properties in the frequency range 62–67 MHz, which corresponds to the period of the induced structure. In subsequent experiments the generation of surface acoustic waves was observed using an alternating electric field applied to the deposited electrodes.

Finally, further evidence of this structure is provided by the ''indelibility'' of the inverted structure when heated to 500°C. A high heating temperature was not used because at $T>500$°C the optical quality of the surface deteriorates. The usual optically induced photorefractive structure is erased at temperatures above 180–200°C.

The mechanism for the formation of inverted domains can be understood on the basis of the concept of lithium niobate as a ''frozen'' ferroelectric. It follows from Ref. 8 that the applied electric field E_s required for polarization reversal depends strongly on temperature. We established that at 140°C the field E_s is 2×10^3 V·mm^{-1}. The comparability between these fields and also the fact that the domain sizes are multiples of the standing wavelength confirm the hypothesis that the piezoelectric field is responsible for the formation of inverse domains.

This mechanism evidently also predominates in the formation of inverse domains by other methods, such as the electric fields induced by a graded distribution of dopants or a graded distribution of defect centers.

The electric fields in the domains measured after cooling are consistent with the electric charges produced by capture of photoexcited electrons by the corresponding centers. The intradomain fields are proportional to the time and intensity of the optical irradiation.

This work was supported financially by the Russian Fund for Fundamental Research, Grant No. 96-02-18229.

[1] M. E. Lines and A. M. Glass, *Principles and Applications of Ferroelectrics and Related Materials* (Clarendon Press, Oxford, 1977; Mir, Moscow, 1981].
[2] N. Berg, B. Undelson, and J. Lee, Appl. Phys. Lett. **31**, 555 (1977).
[3] Yu. V. Vladimirtsev and A. V. Golenishchev-Kutuzov, Pis'ma Zh. Tekh. Fiz. **9**, 809 (1983) [*sic.*].
[4] O. V. Bystrov and A. V. Golenishchev-Kutuzov, Pis'ma Zh. Éksp. Teor. Fiz. **61**, 128 (1995) [JETP Lett. **61**, 135 (1995)].
[5] A. Yariv, *Quantum Electronics* (Wiley, New York, 1975), pp. 335–338.
[6] Q. Chen and D. Stancil, Appl. Opt. **33**, 7496 (1994).
[7] Y. Zhu and N. Ming, J. Phys. Condens. Mater. **4**, 8073 (1992).
[8] V. Kovalevitch, L. Shuvalov, and T. Volk, Phys. Status Solidi **45**, 249 (1978).

Translated by R. M. Durham

Optical properties of layers of ultradisperse diamond obtained from an aqueous suspension

A. E. Aleksenskiĭ, V. Yu. Osipov, N. A. Kryukov, V. K. Adamchuk, M. I. Abaev, S. P. Vul', and A. Ya. Vul'

A. F. Ioffe Physicotechnical Institute, Russian Academy of Sciences, St. Petersburg
(Submitted May 29, 1997)
Pis'ma Zh. Tekh. Fiz. **23**, 39–44 (November 26, 1997)

The possibility of obtaining thin (1500–3000 Å) layers of ultradisperse diamond from an aqueous suspension is reported and the first results of studies of its optical properties are presented. It is deduced from an analysis of the optical absorption spectra of layers of ultradisperse diamond that the band gap of ultradisperse diamond is 2.06 eV. The luminescence spectra of ultradisperse diamond reveal a characteristic line with a peak at 363.7 nm. © *1997 American Institute of Physics.* [S1063-7850(97)02511-1]

Recently, considerable success has been achieved in the preparation of diamond films by chemical deposition from the vapor phase.[1] However, the problem of obtaining diamond films on substrates made of materials whose coefficient of thermal expansion differs substantially from that of diamond or which do not possess chemical affinity with carbon, has yet to be resolved.

One method of solving this problem is to incorporate carbon nucleation centers in the vapor phase during the growth process in the form of fullerenes for example,[2] or to coat the substrate with a preliminary layer containing carbon crystallization centers. In Ref. 3 this layer was deposited from a colloidal solution of diamond particles in acetone with an average size of around 250 nm.

Here we report a possible method of preparing similar layers from an aqueous suspension of ultradisperse diamond powder and we present the first results of a study of their optical properties.

The initial product used to prepare the suspension of ultradisperse diamond was detonation carbon, prepared by commercial detonation synthesis from a 60/40 mixture of trinitrotoluene and hexogen. The ultradisperse diamond was separated by oxidation of the nondiamond component of the detonation carbon using aqueous nitric acid at elevated temperature in a continuous-flow system. The mass obtained after this purification process comprised a suspension of ultradisperse diamond in 30–40% aqueous nitric acid with a diamond concentration of around 3 wt.%. The time taken for this suspension to settle out was around 24 h, when a boundary could be distinguished between the clear and settled layers. Further preparation of the suspension involved repeated dilution with distilled water, mixing, and removing the settled layer. As a result, a suspension of ultradisperse diamond in water was obtained, with a concentration of 0.04 wt.% and a settling time of at least 20 days.

It is known that, like other ultradisperse materials, clusters of ultradisperse diamond combine to form aggregates. In the ultradisperse diamond used to prepare the suspension, the size of the ultradisperse diamond clusters was around 45 Å (Ref. 4). The average diameter of the aggregates in the suspension, determined from the sedimentation characteristics using the Stokes approximation, was around 410 Å. This value agrees with the data given in Ref. 5 according to which the sizes of ultradisperse diamond aggregates in an aqueous medium are in the range 200–600 Å.

Layers of ultradisperse diamond were prepared by deposition of ultradisperse diamond particles from an aqueous suspension onto a fused quartz substrate by evaporating off the water. The layers had a specular surface, the layer thicknesses, determined by an ellipsometric method at $\lambda = 632.8$ nm, were between 1400 and 3500 Å, and the refractive index ($N = n - ik$) varied between $N = 1.40 - 0.08i$ and $N = 1.55 - 0.02i$. The difference between the real part of the refractive index of the layers and the corresponding value for natural diamond ($n = 2.5$) may be attributed to the presence of pores in the layers and to the ''friable'' structure of the ultradisperse diamond aggregates.[5]

Figure 1 shows the spectral dependence $\alpha(\lambda)$ of the optical absorption coefficient of ultradisperse diamond for layers of varying thickness. It can be seen that the absolute values of the absorption coefficient lie in the range $(3\times10^3)-10^5$ cm^{-1}, i.e., they are several orders of magnitude higher than the absorption coefficients of natural diamond single crystals in the same spectral range.[6] However, both the nature of the spectral curve and the absolute value of the absorption coefficient $\alpha(\lambda)$ of the ultradisperse diamond layers are almost the same as those observed for amorphous diamond-like films[7,8] (Fig. 1).

An attempt to determine the band gap in ultradisperse diamond by using the Tauc criterion (plotting the curve $\alpha(h\nu)$ in terms of the coordinates $(\alpha\cdot h\nu)^{1/2} = f(h\nu)$) by analogy with amorphous materials did not yield positive results since the absorption spectrum could not be fitted to a straight line (see inset to Fig. 1). However, this is not surprising and is sometimes observed in amorphous materials. In these cases, the energy for which the absorption coefficient of the material is 10^4 cm^{-1} is frequently taken as the optical band gap.[9] By this criterion the band gap of ultradisperse diamond is 2.06 eV.

Note that the band gap of single-crystal natural diamond is $E_g = 5.5$ eV and thus the optical absorption edge is near 225 nm. In amorphous diamond-like films the band gap may be substantially smaller depending on the ratio between the $sp2$ (''graphite'') and $sp3$ (''diamond'') bonds. For in-

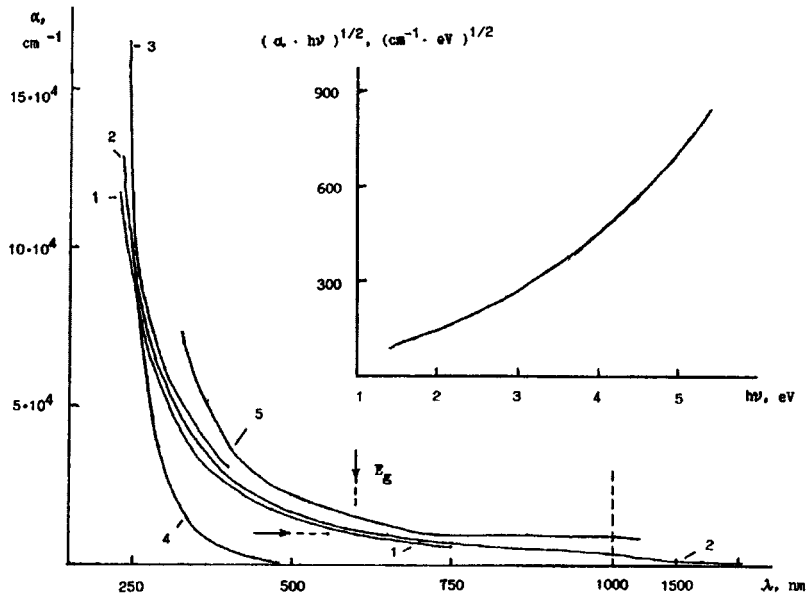

FIG. 1. Spectral dependences of the absorption coefficient $\alpha(\lambda)$ for layers of ultradisperse diamond on quartz at 293 K. Layer thickness, Å: *1* — 1600, *2* — 3000, *3* — 3500; *4* — $\alpha(\lambda)$ for an *a*-C:H film according to data from Ref. 7 ($E_g = 3.6$ eV), *5* — $\alpha(\lambda)$ for an *a*-C:H film according to data from Ref. 8 ($E_g = 2.1$ eV). Wavelength range λ between 230 and 2000 nm. Inset — α versus $h\nu$ for a layer of ultradisperse diamond 3000 Å thick, in Tauc coordinates.

stance, it was shown in Ref. 10 that the tetrahedral lattice of amorphous carbon, where 86% of the atoms form $sp3$ bonds and 14% form $sp2$ bonds, has a band gap of around 2 eV, and a decrease in the fraction of $sp2$ bonds leads to an increase in E_g.

Thus, the existence of strong absorption in the visible range in ultradisperse diamond and the difference between the optical band gap of ultradisperse diamond and the corresponding value for natural diamond may be attributed to the presence of a specific fraction of the amorphous $sp2$ phase. As in Ref. 4, where this phase was observed in analyses of the Raman light scattering and x-ray diffraction spectra, it may be postulated that the $sp2$ phase is available at the surface of the diamond clusters.

The luminescence spectra of layers of ultradisperse diamond (Fig. 2, curve *1*) show a characteristic line with a peak at $\lambda_m = 363.7$ nm ($h\nu = 3.40$ eV). The full width at half maximum of the line is 19.5 nm. The luminescence excitation spectrum — the dependence of the luminescence intensity at λ_m on the wavelength of the exciting radiation — has the form of a saturating curve (Fig. 2, curve *2*). This means that E_g can be determined from the point where the curve of the excitation spectrum reaches a plateau, which gives $h\nu = 5.24$ eV ($\lambda = 236.4$ nm). This E_g value is considerably higher than that obtained from the optical absorption and is close to that for natural diamond. It can therefore be postulated that the luminescence is caused by radiative recombination which takes place in the diamond nucleus of the ultradisperse diamond cluster.

Further investigations are required to identify the nature of the characteristic luminescence line in the range 350–380 nm. An interpretation of this line must obviously take account of the fact that nitrogen is one of the main components of detonating explosives and large quantities (up to 1.5 at.%) are therefore contained in the product particles of ultradisperse diamond. A high percentage of nitrogen in the gas mixture at the stage where the ultradisperse diamond particles are formed may lead to the formation of complex nitrogen complexes. Note, however, that in natural and synthetic bulk diamond crystals nitrogen centers and intrinsic lattice defects do not give rise to any characteristic features in the luminescence at $\lambda = 350$–380 nm (Ref. 1). The small

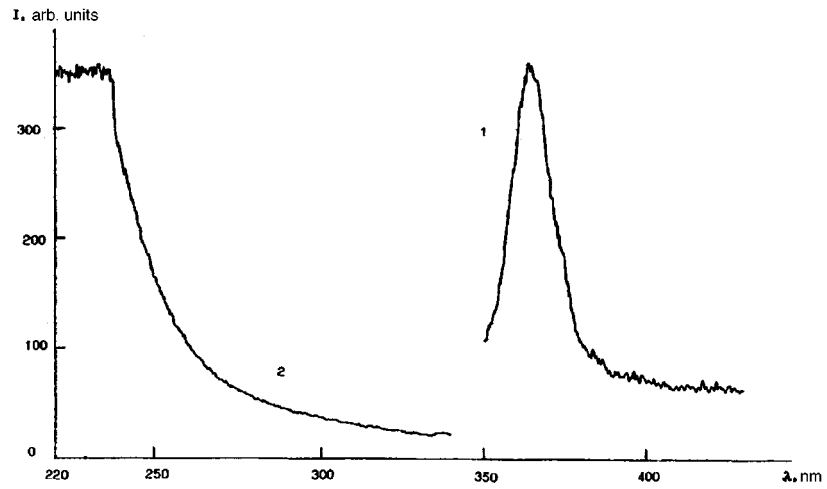

FIG. 2. Luminescence characteristics of layers of ultradisperse diamond on quartz at $T = 293$ K: *1* — luminescence spectrum, *2* — peak luminescence intensity (at $\lambda = 363.7$ nm) as a function of wavelength of exciting radiation.

sizes of the ultradisperse diamond clusters may result in the appearance of a new radiative channel, particularly as a result of the confinement of a photoexcited electron-hole pair. In this context, we note that electroluminescence from diamond films with a peak near 3.0 eV, also of an unidentified nature, was observed in Ref. 11.

The authors are grateful to A. T. Dideĭkin for useful discussions.

This work was carried out as part of the Russian Fund for Fundamental Research Project 96-02-19445 and was partly supported by project No. 039.04.223/57/2-3/1-95 of the State Scientific-Technical Program ''Promising Technologies and Micro- and Nanoelectronics Devices.''

[1] *Synthetic Diamond: Emerging CVD Science and Technology*, edited by K. E. Spear and J. P. Dismukes (Wiley-Interscience, New York, 1994).
[2] D. M. Gruen, S. Liu, A. R. Krauss, J. Luo, and X. Pan, Appl. Phys. Lett. **64**, 1502 (1994).
[3] R. K. Singh, D. R. Gilbert and J. Laveigne, Appl. Phys. Lett. **69**, 2181 (1996).
[4] A. E. Aleksenskiĭ, M. V. Baĭdakova, A. Ya. Vul', V. Yu. Davydov, and Yu. A. Pevtsova, Fiz. Tverd. Tela (St. Petersburg) **39**(6), 1125 (1997) [Phys. Solid State **39**, 1007 (1997)].
[5] G. V. Sakovich, V. D. Gubarevich, F. Z. Badaev *et al.*, Dokl. Akad. Nauk SSSR Ser. Fiz. Khim. **310**, 402 (1990).
[6] C. D. Clark, R. W. Ditchburn, and H. B. Dyer, Proc. R. Soc. London A **234**, 363 (1956).
[7] V. A. Vasil'ev, A. S. Volkov, E. Musabekov, and E. E. Terukov, Pis'ma Zh. Tekh. Fiz. **14**, 1675 (1988) [Sov. Tech. Phys. Lett. **14**, 729 (1988)].
[8] V. I. Ivanov-Omskii, A. V. Tolmatchev, and S. G. Yastrebov, Philos. Mag. B **73**, 715 (1996).
[9] V. Chu, J. P. Conde, J. Jarego, P. Brogueira, J. Rodriguez, N. Barradas, and J. C. Soares, J. Appl. Phys. **78**, 3164 (1995).
[10] P. Stumm and D. A. Drabold, Solid State Commun. **93**, 617 (1995).
[11] C. Manfredotti, F. Wang, P. Polesello, E. Vittone, F. Fizzotti, and A. Scacco, Appl. Phys. Lett. **67**, 3376 (1995).

Translated by R. M. Durham

Investigation of transient processes in YBaCuO films by low-temperature scanning electron microscopy

V. A. Solov'ev, M. É. Gaevskiĭ, S. G. Konnikov, R. A. Suris, and A. V. Bobyl'

A. F. Ioffe Physicotechnical Institute, Russian Academy of Sciences, St. Petersburg;
St. Petersburg State Technical University
(Submitted July 17, 1997)
Pis'ma Zh. Tekh. Fiz. **23**, 45–53 (November 26, 1997)

It has been observed that the inhomogeneity of high-temperature superconducting films influences its temporal characteristics under the local action of electron probe pulses. The proposed method of time-resolved, low-temperature scanning electron microscopy is the first step in this direction. For the first time local investigations with a time resolution of 1 ns have been made of the influence of weak bonds during switching from the superconducting to the normal state and back, under local heating by an electron probe. It was shown that for a $YBa_2Cu_3O_{7-x}$ film 400 nm thick at $T=80$ K, the thermal diffusion time is between 400 and 600 ns depending on the parameters of the film and substrate sections adjacent to the point under study.
 [S1063-7850(97)02611-6]

Methods of determining the thermodynamic parameters of high-temperature superconducting films on substrates (the thermal resistance of the film–substrate interface, the heat diffusion coefficient, the electron–phonon interaction constant, and so on) are generally nonlocal and are based on studying the integrated response of the entire sample to an external pulsed action. Methods used include transmitted current pulses, laser illumination, and microwave irradiation.[1–5] A characteristic feature of high-temperature superconductors is the strong spatial inhomogeneity of various characteristics. In particular, it was shown in Refs. 6–8 that, near T_c, the mechanism of current flow and low-frequency noise in $YBa_2Cu_3O_7$ films is mainly determined by the spatial distribution of its microstructure. Since the thermal resistance and the heat diffusion coefficient are local characteristics of the film and they depend strongly on the substrate material, the film thickness and the quality of the film–substrate interface, and on the structural perfection and composition of the film, the use of nonlocal methods obviously gives appreciable errors in the values of these parameters and the corresponding electron–phonon interaction constants.

Here we propose to develop a method for making local studies of transient processes, with a spatial resolution of 1–2 μm and 1 ns time resolution, in structures based on high-temperature superconducting films. Such studies may also be of interest because of the need to develop various high-speed cryoelectronics devices based on high-temperature superconducting films whose temporal characteristics and degradation are determined by heat transfer processes. The first results described below show that these requirements are met by the method of low-temperature scanning electron microscopy.[6–10] This method involves recording the voltage induced by an electron probe at the contacts of a high-temperature superconducting bridge exposed to local irradiation by a focused 5–20 keV electron beam.

Here we present results of studies of $YBa_2Cu_3O_7$ films by low-temperature scanning electron microscopy for cases of cw and pulsed excitation of the samples by an electron probe. These modes were used to observe the spatial inhomogeneity of the electrophysical properties and to study the time constants of typical sections of the sample. For the measurements we used a CamScan Series 4-88 DV 100 scanning electron microscope fitted with a system for cooling the samples to the range 77–300 K (Oxford Instruments), an electron probe modulator, and also a low-noise amplifier for the electron-probe-induced voltage signal. The spatial resolution of the method was $\sim 1\,\mu$m and the time resolution was 1–2 ns, limited by the pass band of the modulator. The investigations were carried out using $YBa_2Cu_3O_7$ films, 0.4–0.5 μm thick, prepared by magnetron sputtering on an MgO substrate.[10] The results of x-ray structural analysis and Raman spectroscopy revealed a high degree of orientation with the c crystallographic axis of the film perpendicular to the substrate. A standard photolithographic method was used to form 100×500 μm microbridges on the films. These structures became superconducting at $T_c=87$ K with a transition width of $\Delta T_c=0.7$ K.

Immediately after preparation, the samples exhibited a high degree of spatial homogeneity for T_c ($<$ 0.3 K) and high current density, but after thermal cycling between 300 and 77 K ten times, the nonuniformity of the current flow increased appreciably. In particular, low-temperature scanning electron spectroscopy in the cw mode at temperatures $T<T_c$, revealed accumulations of current whose spatial distribution corresponds to the maxima of the induced voltage signal, which is plotted in Fig. 1 for the case of electron beam scanning along the sample. An investigation of the sample morphology in the secondary electron mode revealed microcracks whose position correlated with the position of the corresponding peaks of the induced voltage signal. Studies of the temperature and time dependences of the induced voltage signal were made at various points near one microcrack intersecting the sample (points G, B, and H in Fig. 1), at various spatially separated microcracks (A, B, C, D, and F), and in region E where there were no microcracks. Temperature dependences of the signal at point B near the microcrack and at point E are plotted in Fig. 2. Near the microc-

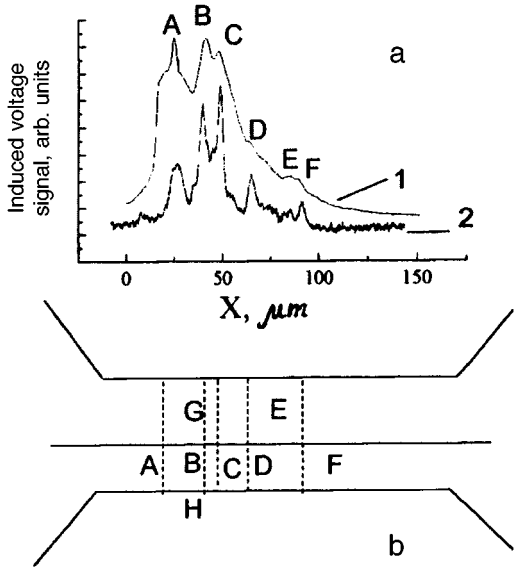

FIG. 1. a — Voltage signal induced by electron probe as a function of the coordinate during electron beam scanning along a bridge, heating temperature $\Delta T=10$ K — curve 1 and $\Delta T=1$ K — curve 2; b — schematic of microbridge showing points at which temperature and time characteristics were measured. The position of the microcracks which appeared after thermal cycling is indicated by the dashed lines; also shown is the line along which the electron beam was scanned.

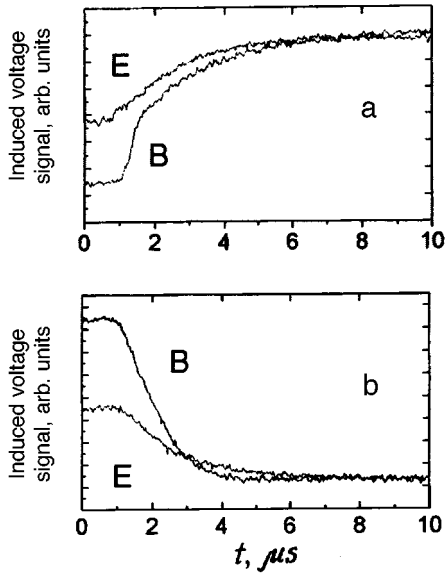

FIG. 3. Time dependences of the induced voltage signal for two typical points on the bridge: a — with the probe switched on, b — with the probe switched off.

rack the peak of the induced voltage signal broadens appreciably and its maximum is shifted toward lower temperatures. This indicates that a weak bond forms at the microcrack with a substantially lower critical current density compared with the defect-free zone.[8]

The following observations may be made on the overheating ΔT. It was shown in Ref. 11 that the voltage signal induced by the electron probe is $S\sim jdV\Delta T$, where j is the displacement current density, dV is the heated volume of the film, and ΔT is the heating temperature. In Refs. 1–5, the entire area of the sample ($\sim 100\times 100\ \mu\text{m}^2$ or greater) was exposed to the external irradiation so that a comparatively low excitation energy density could be used to obtain a sufficiently high signal level and the temperature did not increase by more than 0.05 K. In order to make highly local measurements, the power density and probe current density must be increased. Another favorable factor for enhancing the signal level was the comparatively large film thickness, optimized to give the minimum surface resistance at microwave frequencies. Since the maximum thickness of the films is limited by technological difficulties involved in their fabrication and the current density cannot exceed the critical value j_c (in our case $j_c=5\times 10^5$ A/cm^2 at 77 K), the only method of enhancing the signal level is to increase the heating temperature. In this study ΔT was varied between 0.5 and 10 K.

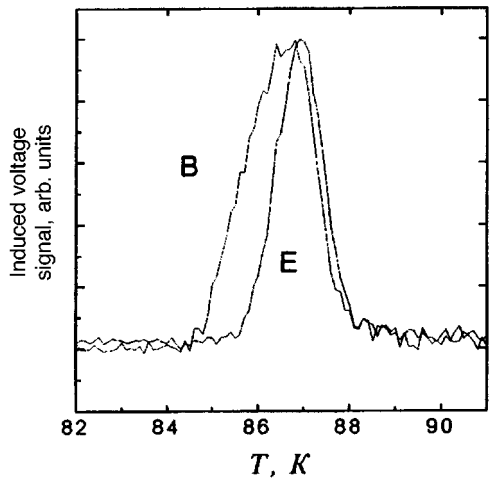

FIG. 2. Temperature dependences of the induced voltage signal for the region with a microcrack at point B in fig. 1 (curve B) and for the defect-free region at point E (curve E).

Typical behavior of the induced voltage signals when the probe is switched on and off is shown in Figs. 3a and 3b, respectively. At points located near weak bonds a rapid rise in the induced voltage signal is observed in the first 100–400 ns, corresponding to a transition of the weak bond from the superconducting to the normal state. This transition is then followed by a section where heat propagates over the substrate and the film. Since the coefficient of heat diffusion in the MgO substrate is more than two orders of magnitude greater than that in the $YBa_2Cu_3O_7$ film, the propagation of heat in the film is mainly determined by the thermal characteristics of the substrate and by the thermal resistance of the film–substrate interface. We note in relation to the latter, that the experiment is carried out at fairly high temperatures of 80–90 K and ballistic expansion of phonons can be neglected so that the thermal resistance can subsequently be considered to be large, also bearing in mind the relatively great thickness of the film. For $\Delta T\sim 10$ K and a displacement current of $0.9j_c$, propagation of heat over the substrate takes place within $\sim 1.5\ \mu$s. After a steady-state temperature distribution has been established over the substrate, heat dif-

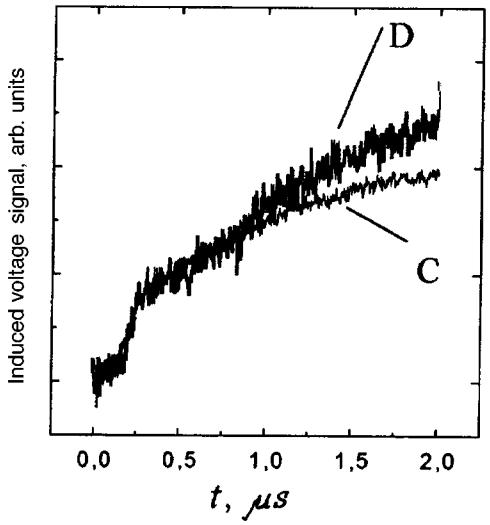

FIG. 4. Normalized time dependences of the induced voltage signal for point C at which the maximum induced voltage signal is observed and for point D at a distance of 15 μm.

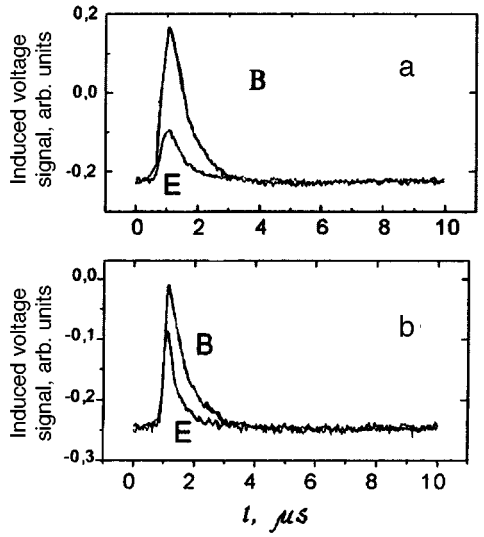

FIG. 5. Dependences of the induced voltage signal $S(t)$ for two different durations of the electron probe pulses: a — 400 ns, b — 200 ns.

fuses into the film, which corresponds to the exponential section $S\sim\exp(t/t_D)$ in Fig. 3a. The characteristic heat diffusion times when the probe is switched on (Fig. 3b) are $t_D=900$ ns whereas when it is switched off, we find $t_D=600$ ns. This difference can be attributed to the temperature dependence of the nonequilibrium phonon velocity, which was observed in Ref. 2, and also to the difference between the temperature distributions at the beginning of the corresponding relaxation processes. As a result of the strong heating of the film by the electron probe with its δ-shaped distribution, the switchon process takes place on average at a higher temperature, which is responsible for the increase in t_D by a factor of 1.5.

When analyzing the profile of the time dependences $S(t)$, we need to bear in mind the influence of the neighboring sections. When the film is subjected to a high level of excitation, Fig. 1 shows strong overlap between the individual peaks. A method of allowing for this influence of neighboring sections when the electron-probe-induced voltage signal is recorded under cw conditions was described in Refs. 7 and 9. Here this influence is observed on the profile of the time dependences $S(t)$. For the curve corresponding to point *E* in Fig. 3, deviations from the exponential profile are observed for $t>1.5$ μs and the effective value $t_{D^{\text{eff}}}$ increases to 1700 ns, which is caused by the influence of the B and C sections. In fact, with increasing distance from the point of incidence of the electron beam, the heating temperature decreases and the corresponding sections make a smaller contribution to the integrated signal. Thus, when the beam is incident in regions B and C, having a high signal level, the contributions made to the signal by the remote sections D and F, having a low signal level, may be neglected. However, when the beam is incident at points D, E, and F, distortion of the signal is observed at the instant when the thermal wave reaches the weak bonds B and C (Fig. 4). The observed effect depends strongly on the excitation time and level. As the exciting pulse time decreases, a decrease in $t_{D^{\text{eff}}}$ is observed at point E. For the excitation time $t=200$ ns, no influence of neighboring points was observed and $t_{D^{\text{eff}}}$ reaches the minimum $t_D=400$ ns (Fig. 5), which agrees with the value obtained for thick $YBa_2Cu_3O_{7-x}$ films in Ref. 5. At points B and C, t_D did not depend on the pulse duration. This may be explained by the fact that neighboring regions with weak bonds are converted to the normal state in times <1.5 μs.

By comparing the data plotted in Figs. 1 and 4, we can estimate the coefficient of heat diffusion in the substrate. It can be seen from Fig. 1 that the distance between point D and the nearest weak bond of point C, corresponding to a high signal level, is $x=15$ μm and Fig. 4 shows that the thermal wave reaches this section after the time $t_1=700$ ns. Additional measurements showed that the time t_1 depends linearly on the distance between the point irradiated by the probe and the region with a high level of induced voltage signal (points B and C). An estimate of the coefficient of heat diffusion gives $D\sim x^2/t_1=3.6$ K/cm^2, which is in good agreement with the coefficient of heat diffusion of the MgO substrate $D=6.2$ K/cm^2 (Ref. 1).

To conclude, we have observed that the inhomogeneity of high-temperature superconducting films influences their temporal characteristics under the action of electron probe pulses. The method used, time-resolved, low-temperature scanning electron microscopy, is a first step in this direction. Local investigations of the influence of weak bonds during switching from the superconducting to the normal state and back again, caused by local heating by the electron probe, have been conducted for the first time with a time resolution of 1 ns. We have shown that for a $YBa_2Cu_3O_{7-x}$ film 400 nm thick at $T=80$ K, the thermal diffusion time is between 400 and 600 ns depending on the parameters of the film and substrate sections adjacent to the point being studied.

This work was carried out under the Russian State Scientific Program ''Superconductivity,'' Project No. 96071.

[1] A. V. Sergeev, A. D. Semenov, P. Kouminov, V. Trifonov, I. G. Goghidze, B. S. Karasik, G. N. Gol'tsman, and E. M. Gershenzon, Phys. Rev. B **49**, 9091 (1994).
[2] E. M. Gershenzon, I. G. Gogidze, G. N. Gol'tsman, A. D. Semenov, and A. V. Sergeev, Pis'ma Zh. Tekh. Fiz. **17**(22), 6 (1991) [Sov. Tech. Phys. Lett. **17**, 786 (1991)].
[3] S. B. Peralta, Z. H. Chen, and A. Mandelis, Appl. Phys. A **52**, 289 (1991).
[4] K. Robl, G. Schlaffer, C. Oprea, B. Brunner, O. Kus, W. Prettl, K. F. Renk, and H. Lengfellner, Physica C **249**, 333 (1995).
[5] L. Ngo Phong and I. Shih, J. Appl. Phys. **74**, 7414 (1993).
[6] R. Gross and D. Koelle, Rep. Progr. Phys. **57**, 651 (1994).
[7] V. A. Solov'ev, M. E. Gaevskiĭ, D. V. Shantsev, and S. G. Konnikov, Izv. Ross. Akad. Nauk Ser. Fiz. **60**(2), 32 (1996).
[8] A. V. Bobyl, M. E. Gaevski, S. F. Karmanenko, I. A. Khrebtov, V. N. Leonov, D. V. Shanrtsev, V. A. Solov'ev, and R. A. Suris, Physica C **266**, 33 (1996).
[9] A. V. Bobyl, M. E. Gaevski, S. G. Konnikov, D. V. Shantsev, V. A. Solov'ev, and R. A. Suris, Scanning Microscopy **10** (1993).
[10] S. F. Karmanenko, V. Yu. Davydov, M. V. Belousov, R. A. Chakalov, G. O. Dzjuba, R. N. Il'in, A. B. Kozyrev, Y. V. Liholetov, K. F. Njakshev, I. T. Serenkov, and O. G. Vendik, Supercond. Sci. Technol. **6**, 23 (1993).
[11] V. E. Umansky, S. A. Solov'ev, S. G. Konnikov, S. F. Karmanenko, and O. V. Kosogov, Mater. Lett. 417 (1990).

Translated by R. M. Durham

Physicochemical mechanism for rearrangement of the shock wave structure in a decaying discharge plasma

A. S. Baryshnikov

A. F. Ioffe Physicotechnical Institute, Russian Academy of Sciences, St. Petersburg
(Submitted May 29, 1997)
Pis'ma Zh. Tekh. Fiz. **23**, 54–57 (November 26, 1997)

A physicochemical mechanism of wave rearrangement in a decaying glow discharge plasma is studied. A mechanism for stratification of the plasma flow via excitation and emission from a pseudometastable oxygen state is confirmed. © *1997 American Institute of Physics.* [S1063-7850(97)02711-0]

The anomalous structure of a shock wave in a glow discharge plasma in air has been studied in previous articles.[1] It has been observed that this structure takes a very long time (approximately 100 s) to disappear as the discharge decays[2] and this behavior cannot be explained merely in terms of electrodynamic theory. It is also known that some excited states of oxygen have a radiative decay time measured in hours.[3] This suggests that an explanation for the mechanism of this effect should be sought in the theory of physicochemical conversions in air.

The theoretical calculations and experiments described in Refs. 4 and 5 may be used to understand the processes taking place in a glow discharge plasma in air. These investigations have the advantage that they were carried out under conditions similar to those studied: gas temperature 353 K, electron temperature and density in discharge 12 000 K and 10^{10} cm^{-3}. The experimental conditions for the effect are: gas temperature in discharge 400–100 K, electron temperature and density 1 eV and 10^{11} cm^{-3} (Ref. 1); the gas pressure (33 Torr) is lower than that in Refs. 4 and 5 (647 Torr in dry air) but this difference can easily be taken into account in the preexponential factor in the expression for the rate of the physicochemical conversions. In addition to dry air, the physicochemical kinetics of a discharge in moist air were also studied in these articles.

Having information on the lifetime of the effect, we can compare this with the times of the processes and determine which state and which process is responsible for the effect. Using the data given in Refs. 4 and 5, we can find several fairly slow processes (process times of the order of 10–100 s under the conditions required to observe the effect):

$$\mathrm{N}+\mathrm{O_2}\rightarrow\mathrm{NO}+\mathrm{Q} \quad k=10^{-16}\mathrm{cm^3/s}, \tag{1}$$

$$\mathrm{N}+\mathrm{O_2}(a^1\Delta)\rightarrow\mathrm{NO}+\mathrm{Q} \quad k=10^{-16}\mathrm{cm^3/s}, \tag{2}$$

$$\mathrm{N}+\mathrm{O_3}\rightarrow\mathrm{NO}+\mathrm{O} \quad k=10^{-15}\mathrm{cm^3/s}, \tag{3}$$

$$\mathrm{O^-}+\mathrm{O}\rightarrow\mathrm{O_3}+e \quad k=5\times10^{-15}\mathrm{cm^3/s}, \tag{4}$$

$$\mathrm{O_2}(b^1\Sigma)+\mathrm{N_2}\rightarrow\mathrm{O_2}+\mathrm{N_2} \quad k=2\times10^{-15}\mathrm{cm^3/s}, \tag{5}$$

$$\mathrm{N_2}(A^3\Sigma)+\mathrm{N_2}\rightarrow\mathrm{N_2}+\mathrm{N_2} \quad k=3.7\times10^{-16}\mathrm{cm^3/s}, \tag{6}$$

$$\mathrm{O_2}(a^1\Delta)+\mathrm{O_2}\rightarrow\mathrm{O_2}+\mathrm{O_2} \quad k=2.2\times10^{-18}\mathrm{cm^3/s}, \tag{7}$$

$$\mathrm{O_2}(a^1\Delta)+\mathrm{N_2}\rightarrow\mathrm{O_2}+\mathrm{N_2} \quad k=1.4\times10^{-19}\mathrm{cm^3/s}, \tag{8}$$

$$\mathrm{O^{-1}}+\mathrm{M}\rightarrow\mathrm{O}+e+\mathrm{M} \quad k=f(E/N), \tag{9}$$

where k is the rate constant of the process.

Reactions (5)–(8) involve the deactivation of excited states of molecules by collisions with air molecules, whose concentrations are orders of magnitude lower than those of the atomic components and electrons. These reactions cannot play any significant role in the discharge. Three-body recombination processes have a substantially longer process time. It is known that deionization of the gas in a glow discharge is mainly caused by ambipolar diffusion. The reactions cited above are secondary processes involving the formation of intermediate states which lengthen the time taken to establish an equilibrium state of the air in the decaying plasma.

It can be seen from the system of reactions (1)–(4) that the main secondary processes involve the formation of atomic oxygen, apart from reaction (4), which reduces the [O] concentration by collisions with negative oxygen ions. Thus, reaction (9), involving the detachment of electrons from oxygen atoms, is a competing process for this reaction. The rate constant of this reaction depends strongly on the parameter E/N, where E is the voltage on the electrodes and N is the gas density. According to data presented in Ref. 4, for $E/N=70$ Td, we have $k=10^{-16}$ and for $E/N>120$ Td we have $k=10^{-12}$. In the case under study, the mechanism for the effect should apply to the decaying plasma and to the discharge itself so we shall consider the discharge. In Ref. 4 we find $E/N=75$–100 Td. The difference in the voltages ($E=12.5$ and 650 V) is compensated by the difference in pressure. Thus, the difference in the ratio is only determined by the difference in gas temperature. At the center of the discharge the temperature is 3–4 times higher and the parameter E/N is also higher. At the edges of the discharge under conditions where the effect is observed, the value of the parameter E/N is close to the values in Refs. 4 and 5 but is 10–20% higher. Consequently, the rate of process (9) is so high, even at the edges of the discharge, that reaction (4) only makes a small contribution to the balance of activated states and may be neglected closer to the center of the discharge. This holds in the decaying plasma of a decaying discharge because of the low [$\mathrm{O^-}$] concentration. This implies that as a result of secondary processes, a fairly high density of atomic oxygen states is formed under these conditions. In order to effectively reduce this density, either the parameter E/N must be reduced substantially or the moisture

content of the air must be increased considerably since, in accordance with Refs. 4 and 5, in moist air the atomic oxygen is replaced by OH hydroxyl groups. This conclusion, together with the observation that there is a high density of atomic oxygen states, form the basic conclusions of the cited articles.

The effect was first observed in an argon discharge.[6] It was shown earlier in Ref. 7 that effects involving rearrangement of the shock wave structure in ionized argon can be explained by a model of emission behind the wavefront whose intensity is proportional to the third power of the concentrations of the plasma components. However, no specific physicochemical mechanism was put forward for this third-order emission. A physicochemical mechanism was also proposed in Ref. 8 for the rearrangement of the discharge structure in argon (but a microwave discharge) where the discharge broke down into an alternate series of light and darker sections.[9] According to this mechanism, the especially close spacing of some metastable and resonant levels in argon (res 11.83 eV, met 11.72 eV, or res 11.62 eV, met 11.55 eV) has the result that the emission is effectively third-order in terms of the component concentration. These groups of states are called ''pseudometastable'' states. In argon the ratio of the energy difference between the resonant and pseudometastable states to the energy of the state itself is approximately 1%. A remarkable factor is that a similar pseudometastable state also exists in atomic oxygen: res 9.51 eV ($3^3S_1^0$), met 9.13 eV ($3^5S_2^0$) for which the relative energy difference is approximately 4%. Other pseudometastable states in an air plasma cannot be identified. It is hypothesized that this atomic oxygen state is responsible for the effect being studied.

[1] I. V. Basargin and G. I. Mishin, Pis'ma Zh. Tekh. Fiz. **15**(8), 55 (1989) [*sic*].
[2] I. V. Basargin and G. I. Mishin, Zh. Tekh. Fiz. **66**(7), 198 (1996) [Tech. Phys. **41**, 742 (1996)].
[3] A. A. Radtsig and B. M. Smirnov, *Reference Data on Atoms, Molecules, and Ions* (Springer-Verlag, Berlin, 1985) [Russ. original, Atomizdat, Moscow, 1980].
[4] Yu. S. Akishev, A. A. Deryugina, V. B. Karal'nik, I. V. Kochetov, A. P. Napartovich, and N. I. Trushkin, Fiz. Plazmy **20**, 571 (1994) [Plasma Phys. Rep. **20**, 511 (1994)].
[5] Yu. S. Akishev, A. A. Deryugin, I. V. Kochetov, A. P. Napartovich, and N. I. Trushkin, Fiz. Plazmy **20**, 585 (1994) [Plasma Phys. Rep. **20**, 525 (1994)].
[6] I. V. Basargin and G. I. Mishin, Pis'ma Zh. Tekh. Fiz. **11**, 209 (1985) [Sov. Tech. Phys. Lett. **11**, 85 (1985)].
[7] A. S. Baryshnikov, *Rarefied Gas Dynamics*, edited by A. E. Beylich, in *Proceedings of the 17th International Symposium on Rarefied Gas Dynamics* (VCH, New York, 1991), pp. 263–270.
[8] M. A. Huerta and J. F. Magnan, Phys. Rev. A **26**, 539 (1993).
[9] H. S. Robertson and J. J. Herring, Phys. Fluids **12**, 836 (1969).

Translated by R. M. Durham

Angular momentum of the fields of a few-mode waveguide: conversion of the angular momentum

A. V. Volyar, T. A. Fadeeva, and N. A. Groshenko

Simferopol State University
(Submitted March 25, 1997)
Pis'ma Zh. Tekh. Fiz. **23**, 58–65 (November 26, 1997)

An analysis is made of the transformation of the angular momentum density in the field of an unstable IV vortex of a few-mode optical fiber. It is shown that the effect of mode dispersion of IV vortices is observed as the conversion of the polarization and orbital components of the electrodynamic angular momentum. The angular momentum defect may be recorded experimentally as a mechanical twist of the optical few-mode fiber. Formally the dispersion process resembles the conversion of the signs of the orbital and polarization components of the angular momentum density. A complex pseudopotential, whose real and imaginary parts characterize the field lines and lines of equal pseudopotential, is introduced to describe the energy flux density of the fiber vortex. The conversion of field states with equivalent partial $\hat{\mathbf{e}}^{+}F_1(R)\exp\{-i\varphi\}$ and $\hat{\mathbf{e}}^{-}F_1(R)\exp\{+i\varphi\}$ vortices was investigated experimentally.
 [S1063-7850(97)02811-5]

The physical mechanisms for the interaction between light and matter allow a distinction to be made between the electrodynamic angular momentum and the quantum spin momentum of an optical field.[1] The angular momentum is usually associated with the rotational degree of freedom of the electromagnetic field and its density is determined as

$$\mathbf{M}=\rho\times\mathbf{P}/c^2, \tag{1}$$

where $\mathbf{P}$ is the Poynting vector. The quantum density of the photon spin vector is given by

$$S_i=1/2\varepsilon_{ijk}(A_k\partial A_j/\partial t-A_j\partial A_k/\partial t) \tag{2}$$

(ε_{ijk} is the Levi-Civita tensor, A_j is the vector potential) and is associated with the internal degree of freedom of the photon field.

Electrodynamic processes for transformation of the angular momentum density $\mathbf{M}$ and $\mathbf{S}$ are known in anisotropic[2] and astigmatic[3] optical systems. The transformation of a linearly polarized Hermite-Gaussian beam HG_{mn} into a Laguerre-Gaussian beam LG_{lp} (l is the topological charge) is usually associated with a transformation of the orbital angular momentum $\mathbf{M}=0$ into $\mathbf{M}=\mathbf{M}_0$. This property can be found in an optical mode converter consisting of a system of spherical and cylindrical lenses. In addition, by acting on the Gouy phase of the natural modes, such a converter can reverse the sign of the topological charge $l\rightarrow -l$ and therefore the sign of the angular momentum.[3]

In optical fibers, the electrodynamic and quantum properties of the fields cannot be considered separately from the vector polarization properties. This is observed most clearly for the unstable IV vortices of a few-mode fiber for which the following relation is satisfied

$$\sigma_z+l=0, \tag{3}$$

where $\sigma_z=\pm 1$ is the helicity of the field, which is characterized by the circulation of the polarization.[5] As a result of the mode dispersion effect in IV vortices, it is possible to have processes of the type

$$-l\rightarrow l, \quad \sigma_z\rightarrow -\sigma_z. \tag{4}$$

It is tempting to associate the orbital angular momentum with the topological charge l and the quantum spin momentum with the helicity σ_z. However, it should be borne in mind that for the momenta $\mathbf{M}$ and $\mathbf{S}$, the laws of conservation are satisfied separately,[1] the quantities $\mathbf{M}$ and $\mathbf{S}$ describe different physical processes, and thus a conversion of the type $\mathbf{M}\leftrightarrow\mathbf{S}$ is impossible.

At the same time, the angular momentum $\mathbf{M}$ of paraxial beams in free space may be represented as a sum of the angular polarization momentum $\mathbf{M}_s$ to which the helicity σ_z makes a contribution, and the orbital angular momentum $\mathbf{M}_l$ associated with the topological charge l (Ref. 6). This division is based on the condition div $\mathbf{e}=0$ ($\mathbf{e}$ is the electric field strength vector) which neglects the polarization properties of the wave in an inhomogeneous medium.

Our aim was to study the conditions for transformation of the transverse components of the Poynting vector of the energy flux in the field of a IV vortex perturbed by the field of the dominant circularly polarized HE_{11} mode of a few-mode waveguide and the associated transformation of the angular momentum density $\mathbf{M}$.

1. Let us assume that a right circularly polarized HE_{11}^{+} mode, having the propagation constant β_0, propagates along a few-mode fiber together with a IV_{-1}^{+} vortex. We write the strength components of the electric and magnetic fields of the perturbed unstable IV_{-1}^{+} vortex in the form:[5,7]

$$\mathbf{e}_t=(\hat{\mathbf{e}}^{+}\exp\{-i\varphi\}\cos\Delta\beta z-i\hat{\mathbf{e}}^{-}\exp\{i\varphi\}\sin\Delta\beta z)F_1$$
$$\times\exp\left\{i\frac{\beta_2+\beta_4}{2}z\right\}+a\hat{\mathbf{e}}^{+}F_0\exp\{i\beta_0 z\},$$

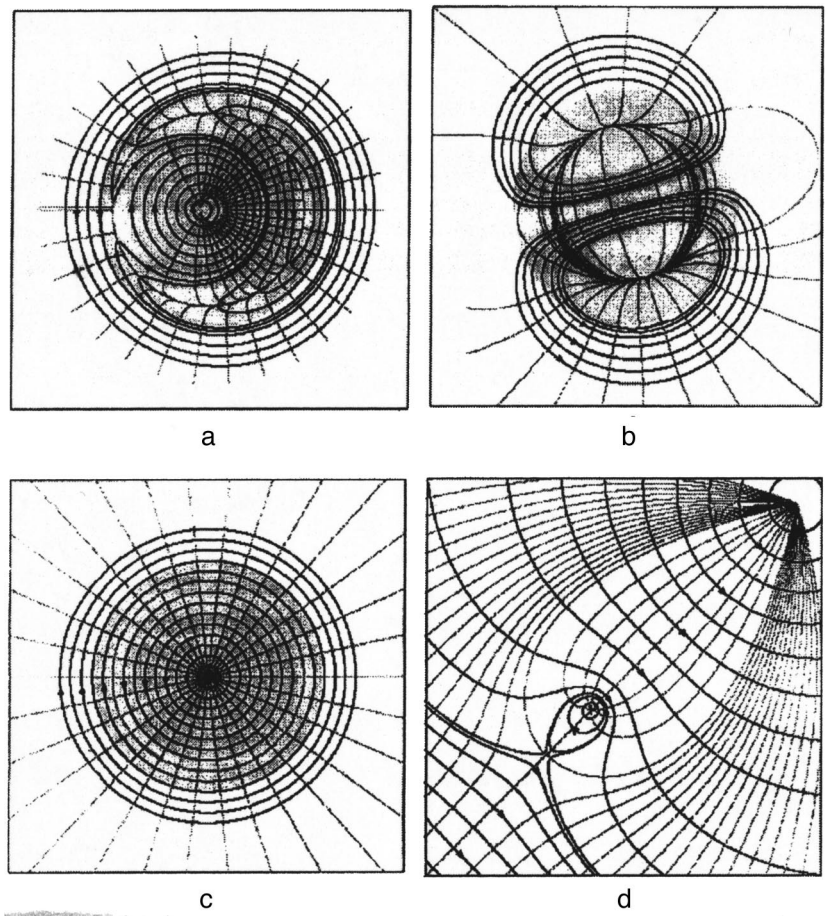

FIG. 1. Distribution pattern of field lines (black curves with arrows) and lines of equal pseudopotential (gray lines) for the field of the Poynting vector $\mathbf{P}_t$ of an unstable IV_{-1}^{+} vortex in the fiber cross sections: a — $\Delta\beta z=0$, b — $\Delta\beta z=\pi/4$, c — $\Delta\beta z=\pi/2$; d — field of the vector $\mathbf{P}_t$ in the region of induced vortex state of the CV vortex.

$$\mathbf{h}_i=-n_{co}\sqrt{\frac{\varepsilon_0}{\mu_0}}\Big\{(\hat{\mathbf{e}}^{+}\exp\{-i\varphi\}\cos\Delta\beta z + i\hat{\mathbf{e}}^{-}\exp\{i\varphi\}\sin\Delta\beta z)F_1\exp\Big\{i\frac{B_2+\beta_4}{2}z\Big\} + a\hat{\mathbf{e}}^{+}F_0\exp\{i\beta_0 z\}\Big\},$$

$$e_z=i\frac{\sqrt{2\Delta}}{V}(G_1^{+}\exp\{i\beta_2 z\}+aG_0\exp\{i\beta_0 z\}),$$

$$h_z=\pm n_{co}\Big(\frac{\varepsilon_0}{\mu_0}\Big)^{1/2}\frac{\sqrt{2\Delta}}{V}(G_1^{+}\exp\{i\beta_4 z\} + aG_0\exp\{i\beta_0 z\}), \qquad (5)$$

where β_2 and β_4 are the propagation constants of the TM and TE modes, $\Delta\beta=(\beta_4-\beta_2)/2$, F_l and G_l are the transverse distribution functions of the $\mathbf{e_t}$ and e_z fields, and R is the normalized radius of the fiber cross section.

Using relation (5), we derive an expression for the components of the Poynting vector $\mathbf{P}=|\mathbf{E}\times\mathbf{H}|$ and the $\mathbf{M}_z$ component of the angular momentum density of the IV_{-1}^{+} vortex perturbed by the field of the HE_{11}^{+} mode:

$$P_\varphi=-K\{F_1G_1^{+}\cos 2\Delta\beta z+a^2F_0G_0 + a(F_0C_1^{+}+F_1G_0)\cos\Delta\beta z\cos(\Delta\beta_1 z-\varphi)\},$$

$$P_r=2Ka(F_0G_1^{+}-F_1G_0)\cos\Delta\beta z\sin(\Delta\beta_1 z-\varphi),\Delta\beta_1 = 1/2(\beta_2+\beta_4)-\beta_0,$$

$$P_z=K\frac{V}{\sqrt{2\Delta}}\{F_1^2+a^2F_0^2+2aF_1F_0\cos\Delta\beta z \times\cos(\Delta\beta_1 z-\varphi)\}, \qquad (6)$$

$$\mathbf{M}_z=\rho\mathbf{P}_\varphi/c^2,\quad K=a_1^2/2\sqrt{\frac{\varepsilon_0}{\mu_0}n_{co}}\frac{\sqrt{2\Delta}}{V}, \qquad (7)$$

where a_1 is the amplitude of the $\mathbf{e}_t$ field strength of the IV vortex, $\rho=\rho_0 R$, and ρ_0 is the radius of the fiber core.

It can be seen from expressions (6) and (7) that the separation of the angular momentum $\mathbf{M}_z$ into orbital and polarization components in IV vortices becomes meaningless. Each expression for the transverse components of the energy flux contains terms which are responsible for both the orbital and polarization components. In addition, the field of an unstable IV vortex is not strictly transverse and the constraint $\mathrm{div}\,\mathbf{e}=0$ is not satisfied for it. The longitudinal z components of the energy and magnetic fields of this vortex are smooth and do not have dislocations although the z components of the perturbing circularly polarized HE_{11}^{+} mode carry a screw dislocation with the topological charge $l=1$.

If the perturbing field is weak or completely absent $(a=0)$, it may be formally assumed that the angular momen-

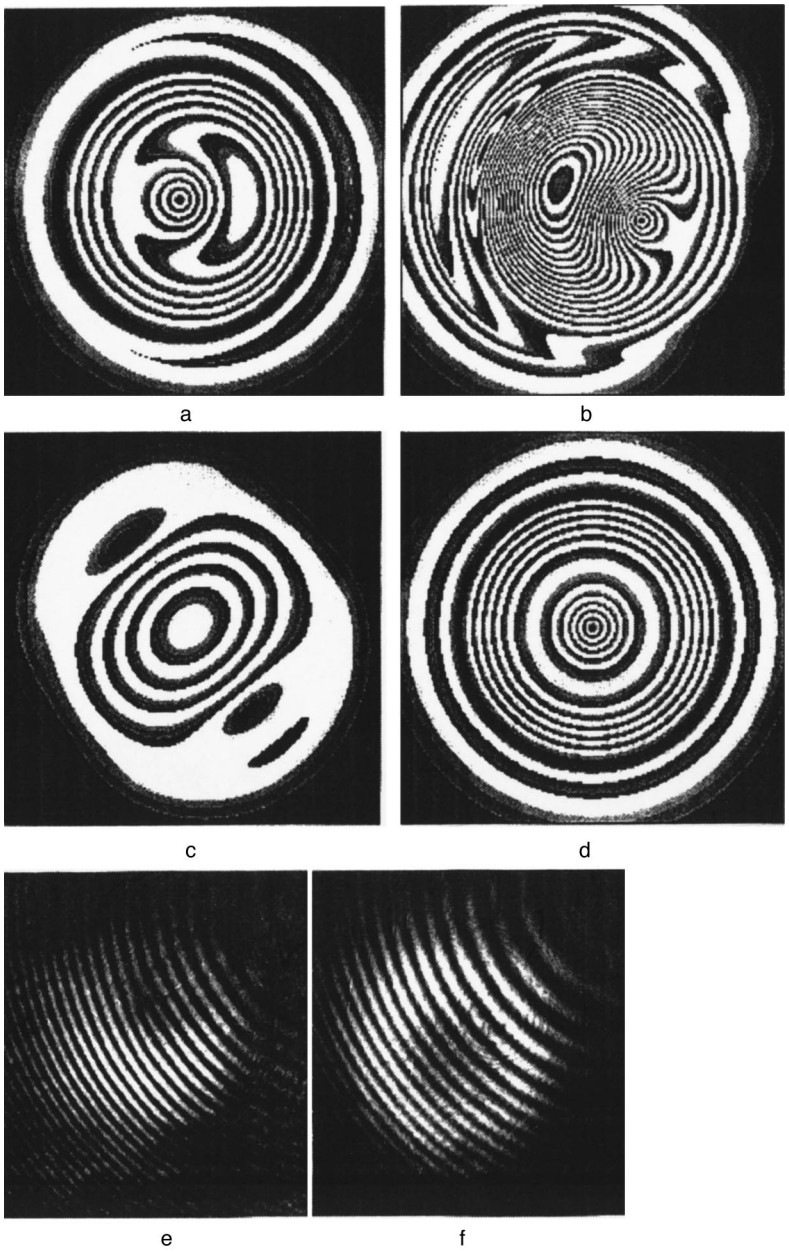

FIG. 2. Distribution pattern of the contours $|P_t| = \text{const}$ of an unstable IV^{+}_{-1} vortex in the fiber cross sections: a — $\Delta\beta z = 0$, b — $\Delta\beta z = 0.95\pi/4$, c — $\Delta\beta z = \pi/4$; d — $\Delta\beta z = \pi/2$. Photographs of the interference pattern of the radiation field of a perturbed IV vortex (e, f).

tum of an unperturbed IV vortex at the entry end of the fiber ($z=0$) corresponds to the polarization momentum $\mathbf{M}_s$ with $\sigma_z = +1$ and the orbital momentum $\mathbf{M}_l$ with $l=-1$. As it propagates along the fiber, the component $\mathbf{M}_z$ of the angular momentum density gradually decreases and reaches the value $\mathbf{M}_z = 0$ at the point $z = \pi/4\Delta\beta$. At the point $z = \pi/2\Delta\beta$, the angular momentum densities correspond to the numbers $\sigma_z = -1$ and $l = +1$, and the direction of $\mathbf{M}_z$ is reversed. The distribution of the $\mathbf{P}_t$ field lines in the fiber cross section is shown in Fig. 1c and the contours $|\mathbf{P}_t| = \text{const}$ are plotted in Fig. 2d (the black area indicates regions where $\mathbf{M}_z = 0$).

We shall consider the propagation process of a perturbed IV^{+}_{-1} vortex. It was shown in Refs. 5 and 8 that the evolution of an unperturbed IV^{+}_{-1} vortex may be represented as beats between partial $\hat{\mathbf{e}}^{+}\exp\{-i\varphi\}$ and $\hat{\mathbf{e}}^{-}\exp\{+i\varphi\}$ vortices, for which the coordinates of the screw dislocations are the same. The perturbing field of the circular HE^{+}_{11} mode displaces the vortex field with like polarization state, inducing a separation of the zero points of the vortices having the charges $l=+1$ and $l=-1$. In accordance with expression (2), the partial vortex with ($\sigma_z = +1$, $l=-1$) is expelled and that with ($\sigma_z = -1$, $l=+1$) remains unperturbed. A screw dislocation with $l=-1$ undergoes both radial and azimuthal displacement. The rate of azimuthal displacement is $w_\phi = 1.38\times 10^4$ rad/m (for $\rho_0 = 3.5\ \mu$m, $V=3.6$), and the rate of radial displacement is $w_\rho \ll w_\phi$. At points $z = (m+1/4)\pi/\Delta\beta$ along the fiber, the screw dislocation is displaced to infinity as a result of radial displacement. At the entry end of the fiber there only exists a field in the state ($\sigma_z = +1$, $l=-1$). The coordinates of the singular points of the field $\mathbf{P}_t$ are determined by the condition $\mathbf{P}_t = \mathbf{P}_\varphi = 0$ and at $z=0$ for $\varphi_0 = \pi$ we have:

$$F_1(R)-aF_0(R)=0, \quad G_1^+(R)-aG_0(R)=0, \tag{8}$$

and for $\varphi_0=0$:

$$G_1^+(R)+aG_0(R)=0. \tag{9}$$

Figure 1 shows the distribution of the field lines (heavy lines with arrows) and the lines of equal pseudopotential of the perturbed field of a IV vortex for the relative perturbation parameter $a=0.1$. The flow lines of the vector **P** were calculated using Eq. (13) from the first part of this study, and the lines of equal pseudopotential were determined from the requirement that they should be orthogonal to the field lines. The term pseudopotential was used to emphasize the nonpotential nature of the field of the Poynting vector **P**: curl **P** $\neq 0$ (but div $\mathbf{P}=0$) and was introduced on the basis of a formal analogy with the velocity field of an ideal fluid.[9]

It can be seen from Figs. 1a and 2a that three systems of field lines having opposite directions of circulation and two groups of pseudopotential lines are formed at the entry end. The first group of pseudopotential lines collects at the localization point $l=-1$ of the dislocation (the center of the vortex of the **P** vector) in the region encompassed by the second group of field lines. The second group of pseudopotential lines begins at infinity and, contracting to a circle, collects at the same point as the first group. At the point $z=\pi/4\Delta\beta$, the first term in $(3, a)$ responsible for the angular momentum of the unperturbed IV_{-1}^+ vortex, vanishes and the main contribution to **M** is made by the field of the circularly polarized HE_{11}^+ mode and the cross term. In this state, the opposite azimuthal fluxes of **P** almost cancel each other out and the lines of pseudopotential collect at the well-defined centers of the vortices of the vector **P**. At $z=\pi/2\Delta\beta$ the induced vortex of the vector **P** completely dominates in this cross section of the fiber. Note that in general we find $L_z=\int_{S_\infty} M_z dS\neq 0$. Thus, at the point $z=\pi/2\Delta\beta$, conversion of the angular momentum $\mathbf{L}_z(\Delta\beta z=0)\rightarrow-\mathbf{L}_z(\Delta\beta z=\pi/2)$ takes place. Formally, this change in the sign of the angular momentum may be expressed as the conversion of the polarization momentum $\mathbf{L}_z^s\rightarrow-\mathbf{L}_z^s$ and the orbital momentum $-\mathbf{L}_z^l\rightarrow\mathbf{L}_z^l$ (for comparison Fig. 1d shows the distribution of the field and pseudopotential lines of the vector $\mathbf{P}_t$ or the field of a stable CV_{+1}^+ vortex in the fiber.)

Figures 2e and 2f show photographs of the interference pattern of a perturbed IV vortex. In Fig. 2e the ''fork'' of the field indicates a region of localization of a screw dislocation at the exit end of the fiber ($l=-1$). Figure 2f shows an interference field in which a screw dislocation with $l=-1$ is displaced to infinity.

[1] N. N. Bogolyubov and D. V. Shirkov, *Introduction to Quantized Field Theory* [in Russian], Nauka, Moscow (1976).
[2] R. A. Beth, Phys. Rev. **50**, 115 (1936).
[3] M. W. Beijersbergen, L. Allen, H. E. L. O. van der Veen, and J. P. Woerdman, Opt. Commun. **96**, 123 (1993).
[4] N. Kukhtarev, A. Volyar, and A. Gnatsky, Int. J. Nonlin. Opt. Phys. **2**, 447 (1993).
[5] A. V. Volyar, T. A. Fadeeva, and Kh. M. Reshitova, Pis'ma Zh. Tekh. Fiz. **23**(5), 69 (1997) [Tech. Phys. Lett. **23**, 70 (1997) [Tech. Phys. Lett. **23**, 198 (1997)].
[6] L. Allen, M. W. Beijersbergen, R. J. C. Spreeuw, and J. P. Woerdman, Phys. Rev. A. **45**, 8185 (1992).
[7] A. W. Snyder and J. D. Love, *Optical Waveguide Theory* (Methuen, London, 1984; Radio i Svyaz, Moscow, 1987).
[8] A. V. Volyar and T. A. Fadeeva, Pis'ma Zh. Tekh. Fiz. **22**(17), 75 (1996) [Tech. Phys. Lett. **22**, 722 (1996)].
[9] M. A. Lavrent'ev and B. V. Shabat, *Methods in the Theory of Functions of a Complex Variable* [in Russian], GITTL, Moscow (1951).

Translated by R. M. Durham

Investigation of spontaneous and coherent radiation in the 3–4 μm wavelength range in an InGaAsSb/AlGaSbAs laser heterostructure

E. A. Grebenshchikova, O. G. Ershov, B. E. Zhurtanov, A. N. Imenkov, N. M. Kolchanova, and Yu. P. Yakovlev

A. F. Ioffe Physicotechnical Institute, Russian Academy of Sciences, St. Petersburg
(Submitted July 16, 1997)
Pis'ma Zh. Tekh. Fiz. **23**, 66–71 (November 26, 1997)

Coherent radiation in the 3–4 μm spectral range has been obtained for the first time in an InGaAsSb/AlGaSbAs double heterostructure grown on a GaSb substrate. It has been shown that spontaneous and coherent radiation is generated mainly as a result of interband transitions in the narrow-gap InGaAsSb layer. It has been established that the optical confinement of the electromagnetic wave is sufficient for operation of the laser up to 120 K with a square-wave supply. © *1997 American Institute of Physics.* [S1063-7850(97)02911-X]

1. Laser structures for the 3–4 μm spectral range, grown on an InAs substrate[1,2] in which the active region consists of ternary InAsSb solid solutions and the emitter layers are formed by wider-gap InAsSbP, are well known. The maximum phosphorus content is $\approx$34% and determines the region of existence of InAsSbP solid solutions isoperiodic with the InAs substrate. As a result of the similarity between the compositions of the narrow-gap and wide-gap layers, the refractive index difference is in the range $\Delta n = 0.02–0.09$. For such a small Δn the differential quantum efficiency of the lasers does not exceed 10–15% because of the strong penetration of radiation into the wide-gap layers and the InAs substrate, and its corresponding absorption.

When the temperature increases above 77 K, not only does the absorption increase, reducing the efficiency , but Δn also decreases, as was shown in Ref. 3, because of an increased carrier density in the narrow-gap layer. Since Δn tends to zero with increasing temperature, it is difficult to raise the operating temperature above 200 K for lasers using these structures.

In AlGaSbAs–InGaAsSb–AlGaAsSb structures with an In content of $\sim$90% in the narrow-gap layer and an Al content $>$60% in the wide-gap layers, Δn may be in the range 0.1–0.3. As the temperature increases from liquid-nitrogen to room temperature, Δn varies negligibly, since the lattice component of the refractive index in the narrow-gap layer increases more rapidly than in the wide-gap layers and compensates for the decrease in the refractive index as a result of an increase in the threshold concentration of nonequilibrium carriers with temperature. With good optical confinement, it should be possible to develop highly efficient lasers with a high operating temperature.

Here, we attempt to fabricate for the first time a laser structure in the long-wavelength 3–4 μm spectral range with large Δn (the difference between the refractive indices of the active and emitter regions) and improved electron confinement.

The laser structure was an isoperiodic AlGaSbAs–InGaAsSb–AlGaSbAs heterostructure grown on a GaSb substrate. The Al content in the wide-gap layer was 64% and the In content in the narrow-gap solid solutions was $\sim$90%. The optical confinement in this structure is still low (0.13) but we anticipate improving this substantially by using wide-gap solid solutions with a high Al content (up to 90%). The large difference between the band gaps of the confining layers and the active layer (Fig. 1c) ensures good electrical confinement for electrons and holes (Fig. 1d).

2. The laser structures were prepared by liquid-phase epitaxy on a n-GaSb substrate oriented in the [100] plane (Fig. 1a). First, we grew a wide-gap n-AlGaAsSb confining layer containing 64% Al, then a narrow-gap n-InGaAsSb active layer containing $\sim$10% Ga and a wide-gap p-AlGaSbAs injector containing 64% Al, and finally a p-GaSb contact layer. All the layers were isoperiodic with the GaSb substrate (the mismatch of the lattice periods did not exceed 0.2%). The thickness of the active region was 1.7 μm and the wide-gap layers were each 1.6 μm thick. The calculated refractive index difference between the wide-gap and narrow-gap layers was $\Delta n = 0.13$ at 77 K (Fig. 1b). These structures were used to fabricate stripe lasers with a stripe width of 20 μm and a cavity length of 200–300 μm. The laser structures were used to investigate the current-voltage, lux-ampere, and spectral characteristics at different temperatures in the range 77–300 K, using techniques described in Ref. 1.

3. Both spontaneous and coherent radiation was obtained for the first time over a wide temperature range in these AlGaSbAs–InGaAsSb–AlGaSbAs structures. Spontaneous radiation was recorded in the range between 77 and 300 K. The maximum energy of the spontaneous radiation band (Fig. 2) was close to the band gap of the narrow-gap material at the appropriate temperature. The long-wavelength slope of the radiation band was gentler than that obtained from interband recombination theory. At low temperature, another two bands can be identified with maximum energies 10–15 and 15–20 meV lower than the maximum energy of the dominant band, respectively. When the temperature is increased from liquid-nitrogen to room temperature, the radiation intensity is reduced approximately ten times for the same current.

Coherent radiation was recorded in the temperature range 77–120 K. Figure 3 shows the coherent radiation spec-

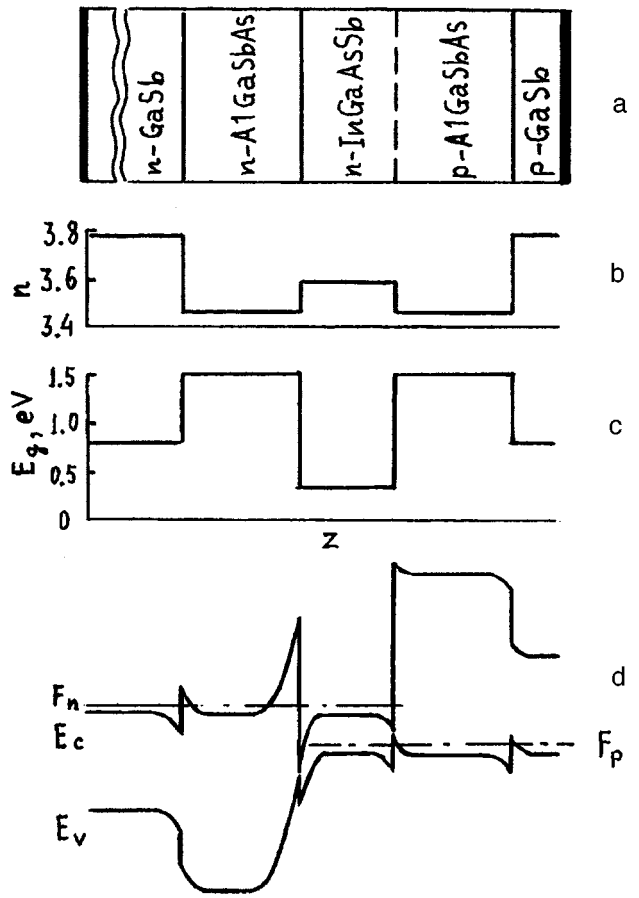

FIG. 1. Schematic of structure studied (a), layer-by-layer profile of refractive index n (b) and band gap E_g (c), and energy diagram in operating mode (d).

tra for four temperatures when the laser is supplied by a square wave. In all cases, the dominant mode suppresses the two neighboring cavity modes with the other cavity modes being weak. Thus, the dominant mode has a large advantage.

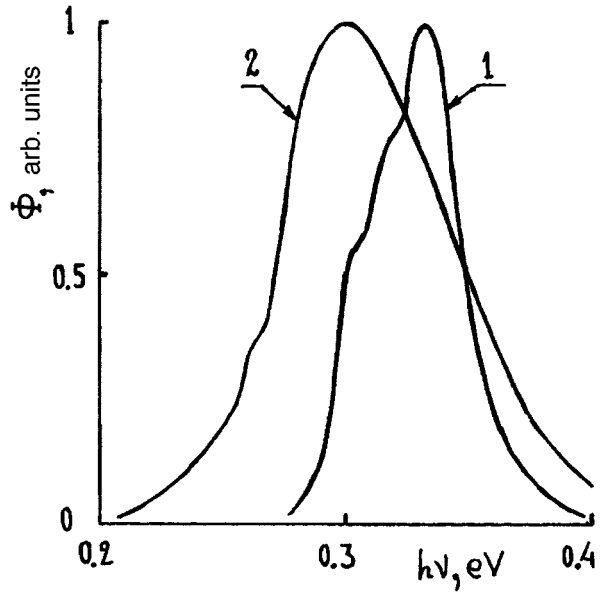

FIG. 2. Spontaneous radiation spectra at 77 K (*1*) and 300 K (*2*).

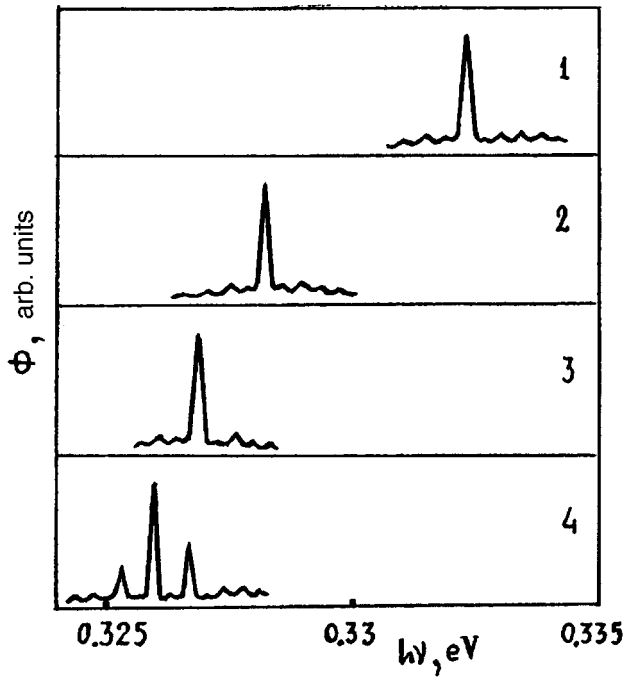

FIG. 3. Laser radiation spectra near lasing threshold at various temperatures T, K: *1* — 100, *2* — 113, *3* — 116, *4* — 120 and currents I, mA: *1* — 140, *2* — 150, *3* — 160, *4* — 180, respectively.

4. We shall analyze the experimental results.

The dominant band in the spontaneous radiation spectrum has a profile close to that predicted theoretically for interband recombination in an n-material. Its half-width can be used to determine the electron concentration in the active region at low currents when the stimulation of radiation is low. From the spectra measured at low currents (less than 10 mA) the electron concentration is $(4–5)\times 10^{16}$ cm^{-3}. This clearly corresponds to the concentration of intrinsic donors in the specially doped active region.

Since the photon energy of the laser radiation is close to the maximum energy of the interband spontaneous radiation band, we can conclude that lasing is achieved as a result of interband transitions. Having due regard to the nature of the energy diagram, we postulate that the weaker long-wavelength bands in the spontaneous radiation spectrum are caused by interface recombination at the type II $p–n$ heterojunction and the $n–n$ heterojunction. Since the depth of the potential wells at the $p–n$ junction is less than that at the $n–n$ junction, one hypothesis is that the short-wavelength and lower-intensity bands are generated by the $p–n$ junction and the longer-wavelength band is generated by the $n–n$ junction. As the thickness of the narrow-gap layer decreases, the fraction of interband recombination will decrease and coherent radiation may be obtained as a result of interface transitions. However, interband recombination predominates in the structures studied where the width of the narrow-gap layer is 1.7 μm. The high Al content in the wide-gap layers has the result that as the temperature rises, the refractive index difference between the narrow-gap and wide-gap layers varies negligibly. Thus, the laser can be operated at 120 K with a

square-wave supply, which gives the best results for lasers in the 3–4 μm range. A further increase in the Al content should improve the laser operating temperature still further.

The fact that the spontaneous radiation intensity only decreases $\sim$10 times when the temperature is increased from 77 to 300 K at constant current means that these structures can also be used to fabricate highly efficient light-emitting diodes.

This work was partly supported by the Copernicus Scientific Program, Grant No. CIPA-CT94-0158.

[1] A. N. Baranov, T. N. Danilova, O. G. Ershov, A. M. Imenkov, V. V. Sherstnev, and Yu. P. Yakovlev, Pis'ma Zh. Tekh. Fiz. **18**(22), 6 (1992) [Sov. Tech. Phys. Let. **18**, 725 (1992)].

[2] T. N. Danilova, A. N. Imenkov, N. M. Kolchanova, A. A. Popov, and Yu. P. Yakovlev, Fiz. Tekh. Poluprovodn. **30**, 1244 (1996) [Semiconductors **30**, 656 1996)].

[3] T. N. Danilova, O. I. Evseenko, A. N. Imenkov, N. M. Kolchanova, M. V. Stepanov, V. V. Sherstnev, and Yu. P. Yakovlev, Fiz. Tekh. Poluprovodn. **31**(6), 662 (1997) [Semiconductors **31**, 563 (1997)].

Translated by R. M. Durham

Observation of a negative characteristic temperature for the threshold current of diode lasers for the 2.8 μm spectral range

A. A. Popov, V. V. Sherstnev, Yu. P. Yakovlev, S. Tsivish, and Z. Zelinger

A. F. Ioffe Physicotechnical Institute, Russian Academy of Sciences, St. Petersburg;
J. Heyrovsky Institute of Physical Chemistry, 18223 Prague 8, Czech Republic
(Submitted July 17, 1997)
Pis'ma Zh. Tekh. Fiz. **23**, 72–79 (November 26, 1997)

A decrease in the lasing threshold with increasing temperature has been observed in InAs/InAsSbP laser heterostructures for the 2.7–2.9 μm spectral range at cryogenic temperatures (T = 32–85 K). At temperatures below 50 K a negative characteristic temperature, $T_0 = -70$ K, was obtained for the threshold current. Characteristics of the temperature dependence of the threshold current and the laser output power were investigated. © *1997 American Institute of Physics.* [S1063-7850(97)03011-5]

1. Recent success in the development of narrow-gap semiconductor lasers utilizing III-V antimonide compounds has stimulated increasing interest in studies of diodes for the 2.5–3 μm spectral range. Diodes for this spectral range are fabricated using InAsSbP (Refs. 1–5), InGaAs/InAs (Ref. 6), and GaInAsSb/GaSb heterostructures[7,8] grown on GaSb and InAs substrates. Unlike the wide-gap analogs, lasing in these narrow-gap semiconductors is accompanied by strong nonradiative Auger recombination which predominates at $T > 77$ K (Refs. 1,3, and 9). Another feature of the band structure of InAs compounds is the similarity between the band gap E_g and the spin-orbit splitting Δ. Thus, the radiation generated in the laser is strongly absorbed by holes in the valence band, which are then excited to the spin-orbit splitting band. The characteristic temperature of the threshold current obtained for lasers using these compounds was 25–30 K (Refs. 1–5), even at temperatures close to liquid nitrogen, and the operating range for cw lasing was limited to cryogenic temperatures ($T < 122$ K) (Ref. 5). The radiative characteristics of these lasers have mainly been studied in the temperature range 77–180 K. Studies of the threshold and power characteristics in the range below liquid nitrogen temperature have not been afforded any special attention. However, this range is interesting because it can be used to study lasing in narrow-gap lasers under conditions where radiative recombination predominates.

The present paper is a continuation of our previous studies on narrow-gap laser heterostructures and is concerned with the threshold and power characteristics of InAs/InAsSbP laser diodes emitting in the wavelength range 2.7–2.9 μm at low temperatures (T = 32–85 K).

2. The laser heterostructures were grown by liquid-phase epitaxy on an InAs (100) substrate. The double heterostructures (see inset to Fig. 1) consisted of a 1.5 μm active region (rated band gap $E_g^{77\,\mathrm{K}} = 425$ meV) between two wide-gap In-AsSbP emitters ($E_g^{77\,\mathrm{K}} = 590$ meV) 2 μm thick. The contact layer was 0.8 μm thick InAs. The electron concentration in the active region was $(2–4)\times 10^{16}$ cm^{-3}. The n-InAsSbP emitter was doped with Sn to a concentration of $(5–8)\times 10^{18}$ cm^{-3} and the p-InAsSbP was doped with Zn to a hole concentration of $(1–2)\times 10^{18}$ cm^{-3}. The diodes had a deep mesastripe structure with a width of 20 μm and a cavity length of 250–300 μm. The laser crystals were attached by the substrate to a special copper heat sink, which allowed the laser to be placed in a closed helium Dewar (Laser Photonics, Model L5731). A current and temperature controller (Laser Photonics, model L5820) was used to pump the lasers and stabilize the temperature. The laser radiation was collimated by an off-axis toroidal mirror to a cooled InSb photodetector. After being processed in a synchronous detection system and analog-to-digital conversion (DAQ), the data were stored in a computer for subsequent analysis.

3. The laser characteristics in the range T = 32–85 K were investigated in the cw mode. The maximum pump current was 210 mA. At $T = 32$ K, lasing was observed with the threshold $I_{th} = 84$ mA. The temperature dependence of the threshold current is plotted in Fig. 1 and consisted of two fundamentally different sections with a point of inflection at T = 45 K. In the first section (T = 32–45 K) it was observed that the threshold current decreased anomalously as the temperature increased to T = 45 K. This behavior is unusual for III-V semiconductor lasers. By fitting the exponential curve $I_{th} = I_{th}^0 \exp(T/T_0)$ to the temperature dependence of the threshold current, we obtain the characteristic temperature $T_0 = -70$ K. In the range T = 45–50 K the curve passed through a minimum $I_{th} = 74$ mA. The second section was observed at temperatures above 50 K and was accompanied by a slight increase in the lasing threshold with the characteristic temperature $T_0 = 180$ K ($T < 65$ K). Such high values of T_0 have not been reported so far for 2.8 μm InAs/InAsSbP lasers. With further increase in temperature, the threshold increased more steeply and at $T > 75$ K the rate of increase was particularly great. In the section T = 65–75 K, and above 75 K, the temperature dependence is described by $T_0 = 60$ K and $T_0 = 27$ K, respectively. It should be noted that this last value, obtained at high temperatures ($T > 75$ K), shows good agreement with the characteristic temperature T_0 = 25–30 K already observed in 3.3 μm laser diodes in the range T = 80–95 K (Refs. 4 and 5) and is obviously typical of mesastripe lasers utilizing InAs compounds.

The current dependences of the laser output power were determined at 5 K temperature intervals. The most characteristic curves, obtained for temperatures T = 32, 40, 50, 70,

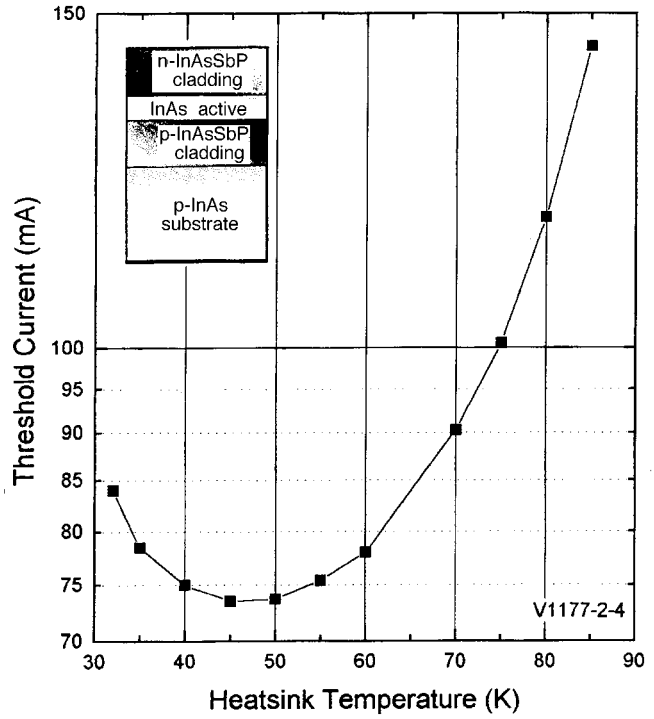

FIG. 1. Temperature dependences of the threshold current of a diode laser in the range 32–85 K. The curves were obtained for cw lasing in the wavelength range 2.7–2.9 μm for a laser with a 20 μm mesastripe width and a cavity length of 300 μm. A schematic of the laser heterostructure is shown in the inset.

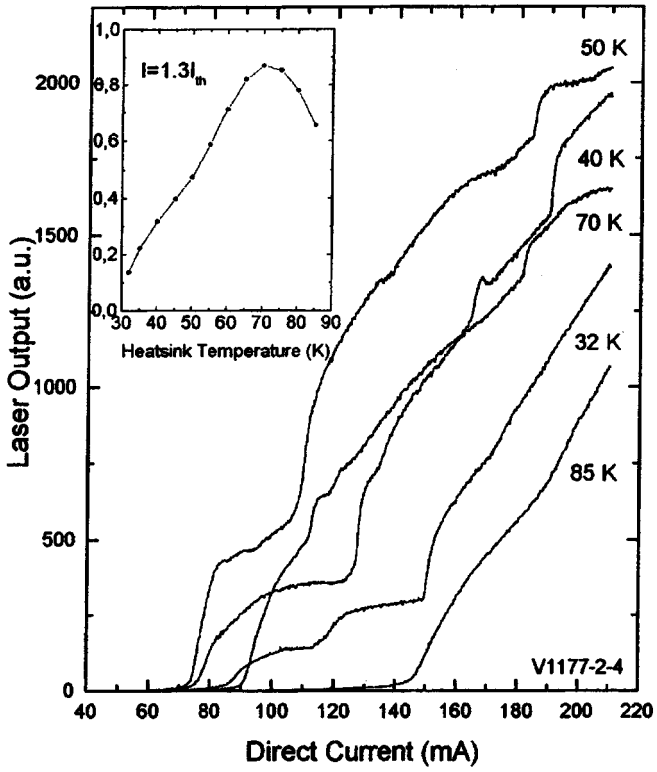

FIG. 2. Laser output power versus pump current obtained at temperatures of 32, 40, 50, 70, and 85 K. The inset shows the temperature dependence of the laser output power plotted for a constant excess of the pumping over the threshold $I=1.3I_{th}$.

and 85 K, are plotted in Fig. 2. At each selected temperature in the range $T = 32$–85 K the optical power increased normally with injection current. However, at temperatures $T<70$ K the curves contained several current sections with a hard switching regime at the boundaries of the sections. In the low temperature range ($T = 32$–50 K) the radiative recombination efficiency near the threshold increased rapidly with temperature and the boundaries of the initial current section became narrower. At high pump currents ($I>1.75$–$1.45I_{th}$) the efficiency fell slightly. At higher temperatures ($T>75$ K) the power characteristics exhibited a monotonic dependence. The radiative recombination efficiency remained almost constant near the threshold current ($I<1.2$–$1.4I_{th}$) and decreased smoothly at high levels of pumping. The inset to Fig. 2 shows the change in the laser power as a function of temperature when the excess of the pumping over the threshold is fixed ($I=1.3I_{th}$). A distinguishing feature of this curve is that the optical output power increases at an almost constant rate as the temperature increases up to $T=65$ K. At higher temperatures the output power falls.

4. We shall discuss the results. These investigations have revealed various features of the threshold and power characteristics of InAs/InAsSbP heterostructure laser diodes for the 2.7–2.9 μm spectral range at temperatures $T = 32$–85 K. Particular mention should be made of the anomalous behavior of the temperature dependence of the threshold current which can be attributed to the section described by a negative characteristic temperature. This section has a steep slope ($T_0=-70$ K) and was obtained for a narrow-gap bulk semiconductor under conditions where nonradiative Auger recombination makes no significant contribution ($T<70$–75 K for the laser studied here, see Fig. 2) and radiative recombination predominates. Among the various possible physical factors responsible for this behavior, mention should be made of intraband absorption (important for InAs when $h\nu>\Delta$), changes in the pumping rate, internal quantum yield, and gain profile.[10] A detailed macroscopic analysis of the behavior of the threshold characteristics of an InAs/InAsSbP laser taking into account radiative and Auger recombination, and intraband absorption[9] revealed an increase in the recombination quantum efficiency at temperatures below 100–150 K. This agrees qualitatively with our experimental results plotted in the inset to Fig. 2. In our case, however, an increase in the lasing efficiency was observed in the range $T<65$ K. In addition, the temperature dependence of the threshold current given in Ref. 9 does not contain the minimum observed in Fig. 1 and cannot be used to explain the observed anomaly of the lasing threshold. In our view, this may be because the theoretical model adopted neglects the characteristics of the carrier energy distribution at low temperatures. However, a considerable part of the temperature dependence of the threshold characteristics of injection lasers is associated with the influence of the density-of-states energy distribution on the gain spectrum. The expression for the threshold current density may be written in the form[10]

$$I_{th}=([\mu_e^* kT/e^* F_{1/2}(F_e/kT)/F_{-1/2}(F_e/kT)]/\tau_e)^{1/2},$$

where $\mu_e = \mu_e(T)$, $F_j(F_e/kT)$, and τ_e are the mobility, Fermi integrals, and lifetime of the carriers, respectively. A possible reason for the observed anomaly may be that at $T =$ 45 K the curve passes through the characteristic temperature $T^* = E_0/kT$, which corresponds to degeneracy of the density-of-states tails in the active region. For InAs/InAsSbP lasers the energy E_0 can be roughly estimated as 3.9 meV. Thus, the optical gain at the threshold, which corresponds to compensation for the losses in the active region, differs for the temperatures corresponding to degenerate and nondegenerate filling of the states ($T < 45$ K and $T > 45$ K). This is consistent with the lack of an abrupt inversion threshold at low temperatures. As the level of degeneracy varies with increasing temperature above $T = 50$ K, the inversion threshold becomes more abrupt. We turn to the laser power characteristics observed at $T < 45$ K which are associated with hard switching. These curves may be typical of cases of lasing where the stimulated recombination efficiency differs substantially, and the intense interaction between them, when their degree of spatial overlap is a function of temperature. Enhanced diffusion of electron-hole pairs and carrier mobility with increasing temperature in the range $T < T^*$ should give rise to considerable spatial overlap between the modes in the bulk of the active region. Under conditions where radiative recombination predominates, spatial overlap of the modes should lead to strong intermode competition and should be observed particularly in the hard switching regime. A change in the lasing region V_v within the bulk of the active region accompanied by an increase in the local laser radiation intensity helps to promote a superlinear increase in power $P_v = h\upsilon^* V_v^* (N_v/\tau_v^{\text{ext}})$ with increasing pumping. As the lasing region becomes stabilized, the current-voltage characteristic of the laser again acquires a more gently sloping profile. Thus, the observed anomaly in the temperature dependence of the threshold current may also be caused by a change in the recombination region. On the whole, the observed anomalous behavior of the temperature dependence of the threshold current is most likely caused by the combined influence of all these mechanisms which will be analyzed in greater detail in subsequent investigations.

To conclude, we have reported the observation of characteristic features in the temperature dependence of the threshold current and output power of InAs/InAsSbP ($\lambda =$ 2.7–2.9 μm) laser heterostructures at cryogenic temperatures of 32–85 K. At temperatures below 45 K the lasers exhibited a section where the threshold current had a negative characteristic temperature $T_0 = -70$ K. It has been shown that the threshold current increases slightly with temperature in the range $T = 50$–70 K and it has been established that the laser optical power reaches a maximum at $T \sim 65$ K. The assumptions made as to the nature of the observed anomalous behavior of the threshold current will form the subject of further detailed investigations.

This work was supported by the EC under the INCO-Copernicus Program.

[1] A. N. Baranov, A. N. Imenkov, V. V. Sherstnev, and Yu. P. Yakovlev, Appl. Phys. Lett. **64**, 2480 (1994).
[2] Yu. P. Yakovlev, N. Danilova, O. G. Ershov, A. N. Imenkov, and V. V. Sherstnev, Pis'ma Zh. Tekh. Fiz. **20**(4), 87 (1994) [Tech. Phys. Lett. **20**, 172 (1994)].
[3] N. Aydaraliev, N. V. Zotova, S. A. Karandashev, B. A. Matveev, N. M. Stus, and G. N. Talalakin, Semicond. Sci. Technol. **8**, 1575 (1993).
[4] A. Popov, V. Sherstnev, Yu. Yakovlev, R. Mücke, and P. Werle, Appl. Phys. Lett. **68**, 2790 (1996).
[5] A. Popov, V. Sherstnev, Yu. Yakovlev, R. Muecke, and P. Werle, Proc. SPIE **3001** (1997).
[6] A. N. Baranov, V. V. Sherstnev, C. Alibert, and A. Krier, J. Appl. Phys. **79**, 3354 (1996).
[7] D. Z. Garbuzov, R. U. Martinelli, R. J. Menna, P. K. York, H. Lee, S. Y. Narayan, and J. C. Connolly, Appl. Phys. Lett. **67**, 1346 (1995).
[8] H. K. Choi, G. W. Turner, M. J. Manfra, and M. K. Connors, Appl. Phys. Lett. **68**, 2936 (1996).
[9] N. A. Gun'ko, G. G. Zegrya, Z. N. Sokolova, N. M. Stus', and B. B. Khalfin, Fiz. Tekh. Poluprovodn. (in press) (1997).
[10] P. G. Eliseev, *Introduction to the Physics of Injection Lasers* [in Russian], Nauka, Moscow (1983).

Translated by R. M. Durham

Self-organization of quantum dots in multilayer InAs/GaAs and InGaAs/GaAs structures by submonolayer migration-stimulated epitaxy

G. É. Cirlin, V. N. Petrov, S. A. Masalov, A. O. Golubok, and N. N. Ledentsov

Institute for Analytical Instrumentation, Russian Academy of Sciences, St. Petersburg;
A. F. Ioffe Physicotechnical Institute, Russian Academy of Sciences, St. Petersburg
(Submitted July 17, 1997)
Pis'ma Zh. Tekh. Fiz. **23**, 80–84 (November 26, 1997)

Multilayer structures of InGaAs/GaAs quantum dots fabricated by submonolayer migration-stimulated epitaxy have been studied experimentally by scanning tunneling microscopy and results are presented. These results clearly show that in multilayer structures, ordering of nanoobjects into rows occurs in InAs and InGaAs heteroepitaxial layers. © *1997 American Institute of Physics.* [S1063-7850(97)03111-X]

One of the principal trends in modern fundamental and applied surface physics is the study of nanostructure formation processes by self-organization of the surface during heteroepitaxial growth in lattice-mismatched systems.[1,2] Quantum dots and quantum wires open the way to the development of a new generation of optoelectronics devices.[3,4] The progress achieved in the theory of nanostructure formation[5] and the observation of ordering effects of quantum-size formations on the surface of an (InAs, InGaAs)/GaAs system[6,7] suggest that it may be possible to obtain quantum-size structures with predefined geometric properties. In Ref. 8 a model was proposed for the self-organization of quantum dots, involving the development of multilayer structures, and experimental data were presented as confirmation of the ''effective'' self-organization of $Si_{0.25}Ge_{0.75}$ on the surface of Si. The results of Ref. 9 also confirm the efficiency of this method for the formation of quantum dots by molecular beam epitaxy in a InAs/GaAs system.

Here we propose to study self-organization processes of quantum dots in multilayer InAs/GaAs and InGaAs/GaAs structures using submonolayer migration-stimulated epitaxy.[10]

The growth experiments were carried out on GaAs(100) substrates using an ÉP1203 molecular beam epitaxy machine. After removing the oxide layer in the growth chamber at a substrate temperature T_s = 610–630 °C in an As_4 stream, a 0.25 μm thick GaAs buffer layer was grown by conventional molecular beam epitaxy at T_s=550 °C providing a (2×4) surface reconstruction. The buffer layer was doped with beryllium to a concentration of $\sim10^{16}$ cm^3 to ensure reliable capture of the tunnel current during the subsequent examination of the surface by scanning tunneling microscopy. After the buffer layer had been grown, the sample temperature in the arsenic stream was reduced to T_s=470 °C (when the surface reconstruction changes from (2×4) to (4×4). In all the experiments the arsenic pressure was kept constant at 2.7×10^{-6} Pa by keeping the arsenic shutter in the growth chamber open.

Each of the layers of InAs and InGaAs quantum dots was formed by submonolayer migration-stimulated epitaxy. In all cases, three monolayers were grown by the following technique: after depositing the required amount of indium for 0.5 ML of InAs, or after depositing the required amount of gallium (33%) and indium (67%) required for 0.5 ML of InGaAs, the surface was held in an arsenic stream for 10 s. The quantum dots formed were then overgrown with a GaAs:Be (20 ML) layer by conventional molecular beam epitaxy at the same temperature T_s, and this process of forming the quantum dots was repeated. After growth had been completed, the sample heater was rapidly disconnected and the sample was removed from the holder zone.

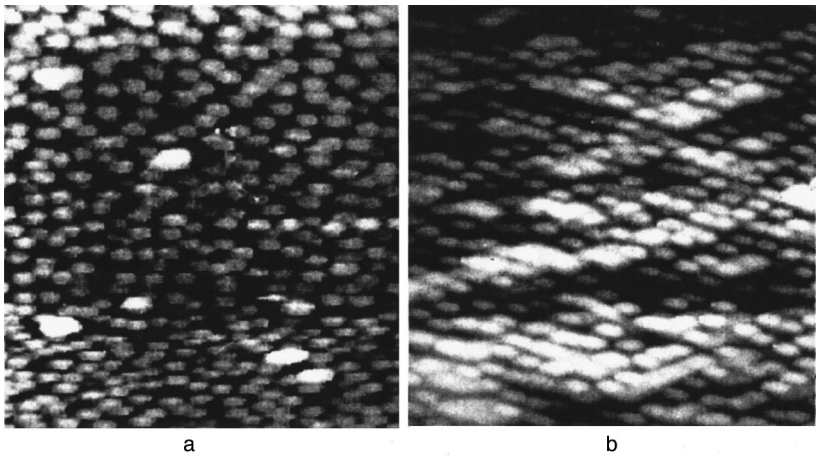

FIG. 1. STM images of sections of the surface after deposition of one layer (a) and ten layers (b) of InAs on GaAs(100). Scanning area 600×600 nm (a) and 700×700 nm (b). The sides of the images are parallel to the [011] and [0-11] directions.

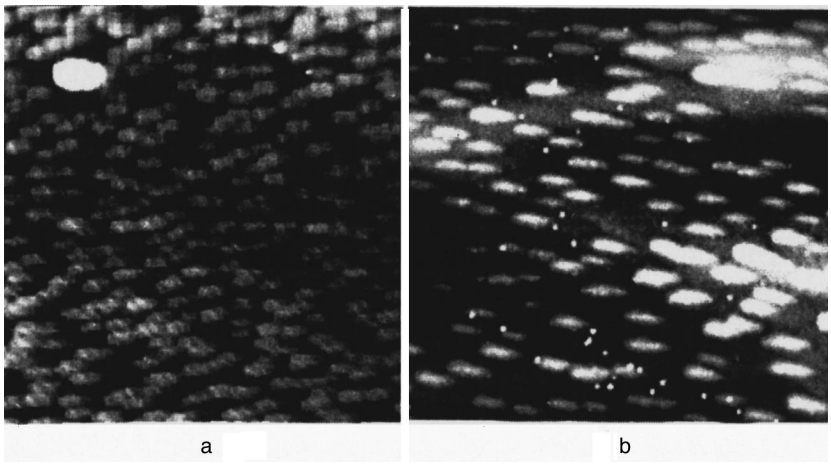

FIG. 2. STM images of sections of the surface after deposition of one layer (a) and ten layers (b) of $In_{0.66}Ga_{0.33}As$ quantum dots on GaAs(100). The scanning area is 600×600 nm for both cases. The sides of the images are parallel to the [011] and [0-11] directions.

The state of the surface was monitored in situ by reflection high-energy electron diffraction (RHEED) using a system[11] which could process the RHEED patterns in real time. The GaAs and InAs growth rates were calibrated by measuring the oscillations of the specular reflex intensity on the RHEED pattern. The GaAs and InAs growth rates during the experiments were 0.5 and 0.1 ML/s, respectively.

The surface morphology of the samples was examined in situ with a scanning tunneling microscope (STM), for which the procedure and measurement conditions were described in Refs. 6 and 12. Multiply reproducible stable STM images were obtained for various sections of the samples at a positive bias in the dc regime ($I_T = 5–7\times10^{-11}$ A, $V_T = 0.7–0.9$ V).

Figures 1a and 1b show STM images of the surface after the formation of one and ten layers of InAs quantum dots, respectively. In both cases the density of quantum dots ($\sim1\times10^{11}$ cm^{-2}) and the lateral dimensions (18–20 nm) are almost the same. However, whereas the spatial distribution of the quantum dots is isotropic for the single layer (Fig. 1a), the distribution of quantum dots for the multilayer structure is anisotropic and is oriented in rows along the [001] and [010] directions (Fig. 1b).

Figure 2a shows STM images of the surface after one and ten layers of InGaAs quantum dots have formed, respectively. In the first case, the spatial distribution is uniform with a fairly high density of quantum dots ($>1.0\times10^{11}$ cm^{-2}) and relatively small lateral dimensions (12 nm). For the multilayer structure the nanoobjects have an elongated profile with a length-to-width ratio of ~4 and are preferentially oriented in the [001] direction. Their surface density in this case is substantially lower ($\sim3\times10^{10}$ cm^{-2}).

To conclude, we have observed experimentally the ordering of nanoobjects into rows in multilayer $In_xGa_{1-x}As/GaAs$ structures obtained by submonolayer migration-stimulated epitaxy. A detailed statistical analysis of these STM images and a discussion of the mechanisms responsible for the ordering of nanoobjects into rows will be presented in a separate article.

This work was partially supported by the Russian Fund for Fundamental Research (Grant No. 95-02-05084-a), INTAS (Grant No. 94-1028), and the Scientific Program ''Physics of Solid-State Nanostructures.''

[1] L. Goldstein, F. Glas, J. Y. Marzin, M. N. Charasse, and G. Le Roux, Appl. Phys. Lett. **47**, 1099 (1985).
[2] J. Tersoff and R. M. Tromp, Phys. Rev. Lett. **70**, 2782 (1993).
[3] M. Grundmann, J. Christen, N. N. Ledentsov, J. Bšhrer, D. Bimberg, S. S. Ruvimov, P. Werner, U. Ricchter, U. Cšsele, J. Heydenreich, V. M. Ustinov, A. Ya. Egorov, A. E. Zhukov, P. S. Kop'ev, and Zh. I. Alferov, Phys. Rev. Lett. **74**, 4043 (1995).
[4] D. S. L. Mui, D. Leonard, L. A. Coldren, and P. M. Petroff, Appl. Phys. Lett. **66**, 1620 (1995).
[5] V. A. Shchukin, N. N. Ledentsov, P. S. Kop'ev, and D. Bimberg, Phys. Rev. Lett. **75**, 2968 (1995).
[6] G. E. Cirlin, G. M. Guryanov, A. O. Golubok, S. Ya. Tipissev, N. N. Ledentsov, P. S. Kop'ev, M. Grundmann, and D. Bimberg, Appl. Phys. Lett. **67**, 97 (1995).
[7] N. N. Ledentsov, M. Grundmann, N. Kirstaedter, O. Schmidt, R. Heitz, J. Bšhrer, D. Bimberg, V. M. Ustinov, V. A. Shchukin, A. Ya. Egorov, A. E. Zhukov, S. Zaitsev, P. S. Kop'ev, Zh. I. Alferov, S. S. Ruvimov, A. O. Kosogov, P. Werner, U. Gšsele, and J. Heydenreich, Solid State Electron. **40**, 785 (1996).
[8] J. Tersoff, C. Teichert, and M. G. Lagally, Phys. Rev. Lett. **76**, 1675 (1996).
[9] S. A. Komarov, G. S. Solomon, and J. S. Harris Jr., in *Proceedings of the International Symposium ''Nanostructures: Physics and Technology '97,''* St. Petersburg, Russia (1997), p. 314.
[10] G. E. Cirlin, A. O. Golubok, S. Ya. Tipisev, N. N. Ledentsov, and G. M. Gur'yanov, Fiz. Tekh. Poluprovodn. **29**, 1697 (1995) [Semiconductors **29**, 884 (1995)].
[11] V. B. Gubanov, G. M. Gur'yanov, V. N. Demidov, V. G. Dubrovskiĭ, N. P. Korneeva, V. N. Petrov, N. K. Polyakov, Yu. B. Samsonenko, and G. E. Cirlin, Nauchnoe Priborostroenie, **6**(1/2), 3 (1996).
[12] G. M. Guryanov, G. E. Cirlin, V. N. Petrov, N. K. Polyakov, A. O. Golubok, S. Ya. Tipissev, E. P. Musikhina, V. B. Gubanov, Yu. B. Samsonenko, and N. N. Ledentsov, Surf. Sci. **331**, 414 (1995).

Translated by R. M. Durham

Reduction in deflections of α-particle orbits in a thermonuclear reactor with an $l=3$ helical winding

Oleg A. Shishkin

Kharkov State University
(Submitted October 14, 1996; resubmitted September 15, 1997)
Pis'ma Zh. Tekh. Fiz. **23**, 85–93 (November 26, 1997)

Studies are made of α-particle trajectories in a reactor-scale magnetic system with a three-turn ($l=3$) helical current winding and an auxiliary current winding generating a vertical magnetic field. It is shown that the deflections of negative and positive free particles relative to the vacuum magnetic surfaces can be reduced by suitably selecting the magnitude and direction of the vertical magnetic field. It is also shown that the deflections of trapped α-particles are reduced under the same conditions. It is particularly important to note that this result was obtained for a system with low aspect ratio. © *1997 American Institute of Physics.* [S1063-7850(97)03211-4]

1. INTRODUCTION

In the optimum magnetic configuration of a fusion reactor based on a toroidal magnetic trap, the displacement of the drift trajectories for free particles having longitudinal velocities parallel and in the opposite direction to the magnetic field (positive and negative free particles) and trapped particles relative to the initial vacuum magnetic surfaces should be as small as possible.[1–8] This problem has almost been solved for a modular stellarator reactor[5] with a Helias magnetic configuration.[2–4] Methods of solving this problem are also being sought for heliotron and torsatron magnetic systems.[6–8,10] This problem is particularly important for compact systems, i.e., systems with a low aspect ratio, which include the system for the Force-Free Helical Reactor (FFHR) with a quasi-force-free helical winding.[8,10] Its magnetic system consists of a three-turn ($l=3$) helical winding and three pairs of vertical field windings (Fig. 1). A feature of this system which distinguishes it from other reactor systems is the strong magnetic field on the circular axis of the torus. The system is designed to generate a magnetic field $B_0=12$ T on the circular axis of the torus. This can be achieved if the tangent of the angle of inclination of the helical conductor to the equatorial plane of the torus is close to one, i.e., $m_h a/R=1$, where m_h is the number of turns of the helical conductor over the torus length, R and a are the major and minor radius of the torus on which the helical windings are wound.

Here we study the trajectory of α-particles in the FFHR magnetic system with the following parameters: major radius of torus $R=1320$ cm, minor radius of torus on which helical winding is wound $a=330$ cm, number of poles in helical winding $l=3$, and number of magnetic field periods over torus length $m=12$ ($m_h=4$). Possible methods of regulating the orbits of free and trapped particles (drift trajectories) relative to the magnetic surfaces are examined. It is shown that by altering the vertical magnetic field generally present in the configuration, the deflections of the α particle trajectories from the initial magnetic surfaces can be reduced appreciably.

2. PROPERTIES OF THE MAGNETIC CONFIGURATION

By changing the magnitude and direction of the vertical magnetic field (its dipole component), it is possible to shift the magnetic surfaces into the inner or outer parts of the torus and thereby alter the character of the magnetic field modulation in the direction of the field line (Fig. 2). The magnetic surfaces are shown in the meridional cross sections after a period and half-period of the magnetic field. The quality of the magnetic surfaces satisfies the conditions of plasma confinement in the following range of variation of the vertical magnetic field: $-0.003\leqslant B_\perp/B_0\leqslant 0.015$. The average radius of the magnetic surfaces with the same starting point for the magnetic field line increases with increasing vertical field. For a vertical field $B_\perp/B_0=0.015$ the outermost magnetic fields are close to rational. This is indicated by the position of the field line traces which run ''in pairs'' a short distance apart. These magnetic surfaces may require correction in the presence of perturbing magnetic fields. Such a correction may be achieved by using higher-order harmonics of the angular variable along the torus minor circumference, and is accomplished in practice by varying the currents in the vertical field windings.

For the same range of variation of the vertical field, the modulation of the field along the field line taken on a magnetic surface whose radius is approximately half the radius of the outermost magnetic surface, varies as follows: when the magnetic surfaces are shifted to the outer part of the torus, the ripple increases in the region of stronger toroidal field. This is an indication of conditions for enhanced radial drift of trapped particles, as we know from Ref. 9. When the magnetic surfaces are shifted into the inner part of the torus, the ripple decreases in the region of weaker toroidal field and increases in the region of stronger toroidal field. This is an indication of a favorable configuration for suppressing radial drift of trapped particles.[9]

For this range of variation of the vertical field the angle of rotation transform varies in the range $0.29\leqslant l\leqslant 0.64$.

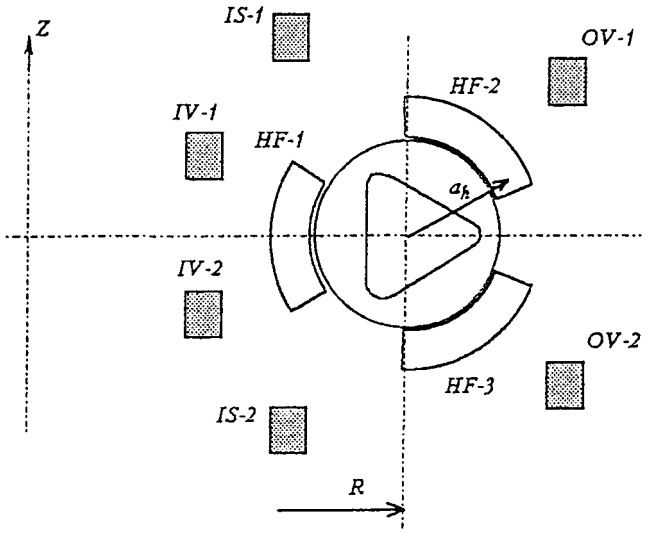

FIG. 1. Schematic of current coils in the magnetic system: HF-1, HF-2, HF-3 — helical conductors, IV-1, IV-2, IS-1, IS-2, OV-1, OV-2 — pairs of annular conductors.

3. BASIC EQUATIONS AND MAGNETIC FIELD MODEL

The study of trapped particle motion is based on solving a system of equations of motion for the particle guiding center

$$\frac{d\mathbf{r}}{dt}=V_{\parallel}\frac{\mathbf{B}}{B}+\frac{c}{B^2}[\mathbf{E}\times\mathbf{B}]+\frac{M_j c(2V_{\parallel}^2+V_{\perp}^2)}{2e_j B^3}[\mathbf{B}\times\nabla B],$$

$$\frac{dW}{dt}=0,\quad \frac{d\mu}{dt}=0,$$

where W and μ are the total energy and magnetic moment of the particle, $V_{\parallel}$ and $V_{\perp}$ are the particle velocities parallel and at right angles to the magnetic field, M_j and e_j are the particle mass and charge, $\mathbf{r}$ is the position vector of the particle guiding center, c is an electrodynamic constant, and $\mathbf{E}$ and $\mathbf{B}$ are the electric and magnetic fields.

The magnetic field components are defined in a quasicylindrical coordinate system, relative to the circular axis of the torus, as a Fourier series expansion in terms of the angular variables θ and φ: $\mathbf{B}=\nabla\Phi$, where the scalar potential of the magnetic field is given by:

$$\Phi=B_0\left\{R\varphi-R/m\left[\sum_N \varepsilon_N(r/a)^N\sin(N\theta-m\varphi)+\sum_k \varepsilon_k(r/a)^k\sin\, k\theta\right]\right\},$$

where r is the radial variable, θ and φ are the angular variables along the major and minor radii of the torus: θ is measured from the direction opposite to the principal normal to the circular axis of the torus, ε_N and ε_k are the coefficients of the magnetic field harmonics. In our case, these have the values: $N=3$, $\varepsilon_3=0.76$, and $k=1$, and the parameter ε_1 has the following three values for the three vertical fields studied: $B_V/B_0=-0.003$, 0.0, and 0.015 .

4. α-PARTICLE ORBITS

The main source of α particle generation should be the center of the plasma where the plasma density and temperature are highest. This point should be located at the center of the magnetic surfaces near the magnetic axis. To study the trajectories of 3.52 MeV α-particles we defined the starting

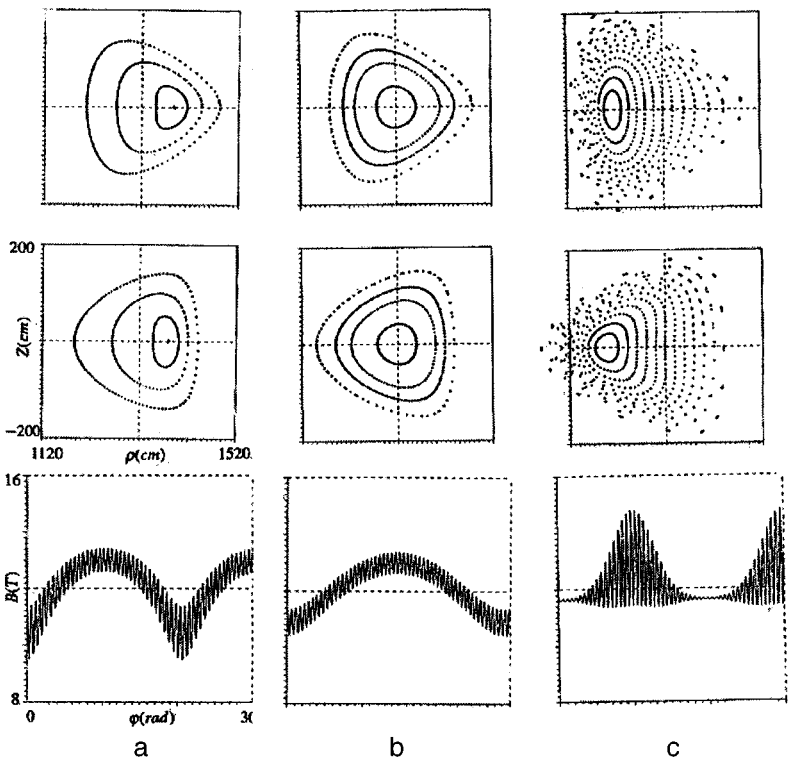

FIG. 2. Profile of magnetic surfaces in meridional cross sections at the beginning of a magnetic field period: $\varphi=0$ (upper row), and in a magnetic field half-period $\varphi=\pi$ (middle row), and modulation of the magnetic field along the field line for a surface whose average radius is half the average radius of the outermost unperturbed magnetic surface (lower row) for $B_{\perp}/B_0=-0.003$ (a), $B_{\perp}/B_0=0.0$ (b), and $B_{\perp}/B_0=0.015$ (c). In the upper and middle rows the distance from the direct axis of the torus is given along the abscissa and the distance along the direct axis of the torus is given on the ordinate.

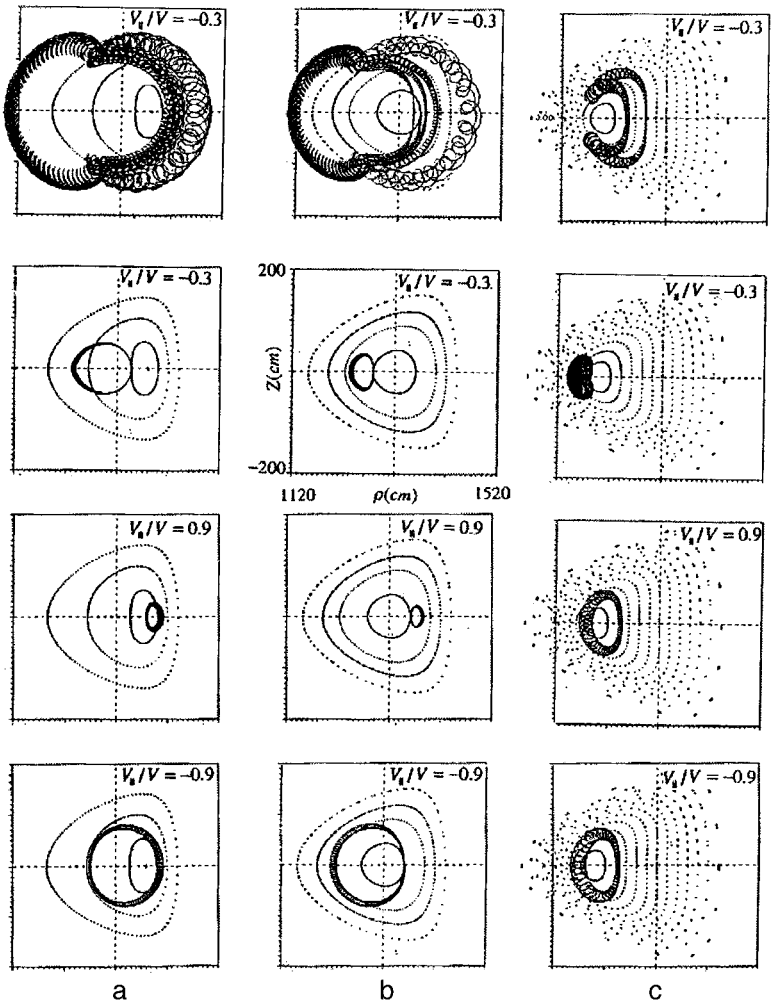

FIG. 3. Projections of α-particle trajectories on meridional cross section for $V_\parallel/V=-0.3$ (first and second rows), $V_\parallel/V=0.9$ (third row), $V_\parallel/V=-0.9$ (fourth row) for $B_\perp/B_0=-0.003$ (a), $B_\perp/B_0=0.0$ (b), and $B_\perp/B_0=0.015$ (c). The distance from the direct axis of the torus is given on the abscissa and the distance along the torus direct axis is given on the ordinate.

point so that the deflections of the orbits from magnetic surfaces with almost the same average radius ≈ 40 cm could be compared in different configurations (Fig. 3). We selected the most typical trajectories for which the ratio of the longitudinal velocity to the total particle velocity was $V_\parallel/V=-0.3$, as well as $V_\parallel/V=0.9$ and -0.9.

Particles starting from a region of weaker toroidal field (first row in Fig. 3) are converted into trapped particles and move a considerable distance from the initial surface for $B_\perp/B_0=-0.003$ (Fig. 3a) and for $B_\perp/B_0=0.0$ (Fig. 3b). For $B_\perp/B_0=0.015$ (Fig. 3c) this particle is reflected into a region of stronger toroidal field and its deflection is substantially smaller.

Particles starting near the same surfaces but on the side of weaker toroidal field (second row in Fig. 3), although free for $B_\perp/B_0=-0.003$ (Fig.3a) and for $B_\perp/B_0=0.0$ (Fig. 3b), are deflected from the initial surface by appreciable distances. For the case $B_\perp/B_0=0.015$ (Fig. 3c) a similar particle is trapped and remains near the initial magnetic surface.

As the absolute value of the ratio $V_\parallel/V$ increases (third and fourth rows in Fig. 3), the particles are free. The differences between the positive and negative free particles are very great for $B_\perp/B_0=-0.003$ (Fig. 3a) and $B_\perp/B_0=0.0$ (Fig. 3b) but are barely noticeable for $B_\perp/B_0=0.015$ (Fig. 3c). Figure 3 shows particle orbits starting near inner surfaces. Exactly the same effect — a substantial reduction in the difference between the deflections of the positive and negative free particles — is found for $V_\parallel/V=\pm 0.9$ for the outer magnetic surfaces.

The physical mechanism responsible for this effect involves compensation for the toroidal magnetic field gradient by harmonics which are satellites relative to the fundamental helical harmonic. These harmonics form as combination harmonics as a result of the action of the vertical magnetic field on the pure third helical harmonic.

5. CONCLUSIONS

1. The incorporation of a vertical magnetic field in the magnetic system of a fusion reaction with a three-turn ($l=3$) helical winding can control and substantially reduce the deflections of α-particle orbits from vacuum magnetic surfaces.

2. In a configuration where the magnetic axis is shifted inside the torus the deflections of positive and negative free particles are reduced substantially compared with configurations where the magnetic axis is shifted into the outer part of the torus or where there is a zero shift.

3. For the same parameters in this configuration the magnetic field modulation is favorable for suppressing radial drift of trapped particles.

4. It is particularly important to note that this effect is achieved in a magnetic system with a low aspect ratio $(R/a=4)$.

In conclusion, the author would like to thank Professor O. Motojima (National Institute for Fusion Research, Tokyo, Japan) for continuous support, Doctor A. V. Zolotukhin and Doctor I. N. Sidorenko (Kharkov Physicotechnical Institute, Kharkov, Ukraine) for considerable assistance at the beginning of this research, and Doctor A. Shishkin (Kharkov Physicotechnical Institute) for suggesting this subject.

[1] R. Chodura, W. Dommaschk, F. Herrnegger, W. Lotz, J. Nührenberg, and A. Schlüter, IEEE Trans. Plasma Sci. **PS-9**, 221 (1981).
[2] H. Wohbig, in *Proceedings of the Workshop on Wendelstein 7-X*, Schloss Ringberg, Bavaria 1987, pp. 93–113.
[3] W. Lotz, P. Merkel, J. Nurenberg and E. Strumberger, Plasma Phys. Contr. Fusion **34**, 1037 (1992).
[4] A. V. Zolotukhin, C. D. Beidler, F. Herrnegger, J. Kisslinger, and H. Wohbig, in *Proceedings of the 23rd European Physical Society Conference on Controlled Fusion and Plasma Physics*, Kiev, Ukraine, 1996, paper b001.
[5] J. V. Hofmann, J. Baldzuhn, R. Brakel, Y. Feng, S. Feidler, J. Geiger, P. Grigull, G. Herre, R. Janicke, M. Kick, J. Kisslinger, G. Kuhner, A. Runow, F. Sardei, U. Stroth, F. Wagner, A. Weller, and H. Wobig, in *Proceedings of the 23rd European Physical Society Conference on Controlled Fusion and Plasma Physics*, Kiev, Ukraine, 1996, paper b006.
[6] B. A. Carreras, N. Dominguez, L. Garcia, V. E. Lynch, J. F. Lyon, J. R. Cary, J. D. Hanson, and A. P. Navarro, Nucl. Fusion **28**, 1195 (1988).
[7] S. L. Painter and J. F. Lyon, Fusion Technol. **16**, 157 (1989).
[8] O. Motojima, K. Y. Watanabe, A. Sagara, K. Yamazaki, A. A. Shishkin, A. V. Zolotukhin, M. S. Smirnov, I. N. Sidorenko, N. A. Belash, E. I. Polunovskii, and O. A. Shishkin, in *Proceedings of the 23rd European Physical Society Conference on Controlled Fusion and Plasma Physics*, Kiev, Ukraine, 1996.
[9] H. E. Mynick, T. K. Chu, and A. H. Boozer, Phys. Rev. Lett. **48**, 322 (1982).
[10] O. Motojima, K. Y. Watanabe, A. Sagara, K. Yamazaki, A., A. Shishkin, A. V. Zolotukhin, M. S. Smirnova, I. N. Sidorenko, N. A. Belash, and O. A. Shishkin, in *Proceedings of the Sixth Workshop on Wendelstein 7-X and Helias Reactors*, Schloss Ringberg, Bavaria, 1995, edited by F. Herrnegger and F. Rau, IPP2/331 (1996), pp. 227–236.

Translated by R. M. Durham